THREAD COUNTER BASED ON IMAGE PROCESSING USING A REFERENCE SIGNAL

PONGSAK KHOKHUNTOD

A Dissertation Submitted to Graduate School of Naresuan University
in Partial Fulfillment of the Requirements
for the Doctor of Philosophy Degree in Applied Physics
May 2025

Dissertation entitled "Thread counter based on image processing using a reference signal"
by Pongsak Khokhuntod
has been approved by the Graduate School as partial fulfillment of the requirement for the Doctor of Philosophy in Applied Physics of Naresuan University

Oral Defense Committee

..... Chair
(Professor Paramote Wardkein, D.Eng.)

..... Advisor
(Associate Professor Anucha Kaewpoonsuk, D.Eng.)

..... Committee
(Associate Professor Attapon Amthong, Ph.D.)

..... Committee
(Assistant Professor Kriangsak Prompak, Ph.D.)

..... Committee
(Assistant Professor Ratchanoo Katman, Ph.D.)

Approved

.....
(Associate Professor Krongkarn Chootip, Ph.D.)
Dean of the Graduate School

30 MAY 2025

ACKNOWLEDGMENTS

First and foremost, I would like to sincerely thank Associate Professor Dr. Anucha Kaewpoonsuk for giving me the opportunity to pursue this work. His steady guidance, thoughtful advice, and constant support have been instrumental throughout my research. I am especially grateful for the academic freedom and opportunities he provided, which have contributed greatly to both my personal and professional growth.

I am also thankful to my thesis committee: Professor Dr. Paramote Wardkein, Associate Professor Dr. Attapon Amthong, Assistant Professor Dr. Kriangsak Prompak, and Assistant Professor Ratchanoo Katman. Their insightful feedback and helpful suggestions have strengthened this thesis in many ways, and I deeply appreciate the time and effort they devoted to reviewing my work.

My gratitude also goes to the Department of Physics, Faculty of Science, Naresuan University, for creating a supportive and inspiring research environment. I especially thank the department staff for their practical support, including providing equipment and assistance with administrative matters. I would also like to acknowledge fellow researchers in the department for their helpfulness and encouragement along the way.

Lastly, I am profoundly grateful to my family. Their patience, support, and belief in me have meant more than words can express.

Pongsak Khokhuntod

Title	THREAD COUNTER BASED ON IMAGE PROCESSING USING A REFERENCE SIGNAL
Author	Pongsak Khokhuntod
Advisor	Associate Professor Anucha Kaewpoonsuk, D.Eng.
Academic Paper	Ph.D. Dissertation in Applied Physics, Naresuan University, 2024
Keywords	Moiré pattern, Fourier analysis, Binary grating, Stripe density, Moving average filter, Image processing

ABSTRACT

This study presents a two-part investigation into stripe density analysis based on the Moiré pattern phenomenon. The first part focuses on the theoretical modeling of binary rectangular gratings using logic signals with two discrete levels: "0" and "1." Fourier series are used to describe their frequency components, phase relationships, and duty cycles. The overlap between two gratings is mathematically formulated using expressions that correspond to logical AND and OR operations. Simulation results confirm that the output signals align with the theoretical predictions, showing clear relationships between the structural parameters of the gratings and the characteristics of the resulting Moiré patterns.

The second part introduces a practical method for measuring stripe density using image processing techniques. The proposed system applies a moving average filter to isolate low-frequency signals, allowing it to suppress high-frequency noise in both simulated and real fabric images. Grid lines with gradually increasing frequency are generated from left to right and overlaid on the target image to determine where the frequencies match. Experiments conducted on synthetic stripe patterns ranging from 30 to 180 L^{-1} and on actual fabric images show that the system can measure stripe density with a maximum deviation of less than ± 1 L^{-1}.

This approach offers a reliable and automated solution suitable for industrial and scientific applications that require accurate and repeatable stripe density measurements.

LIST OF CONTENTS

Chapter **Page**

LIST OF CONTENTS (CONT.)

Chapter **Page**

LIST OF CONTENTS (CONT.)

Chapter **Page**

LIST OF FIGURES

Figure **Page**

LIST OF FIGURES (CONT.)

Figure **Page**

LIST OF FIGURES (CONT.)

Figure **Page**

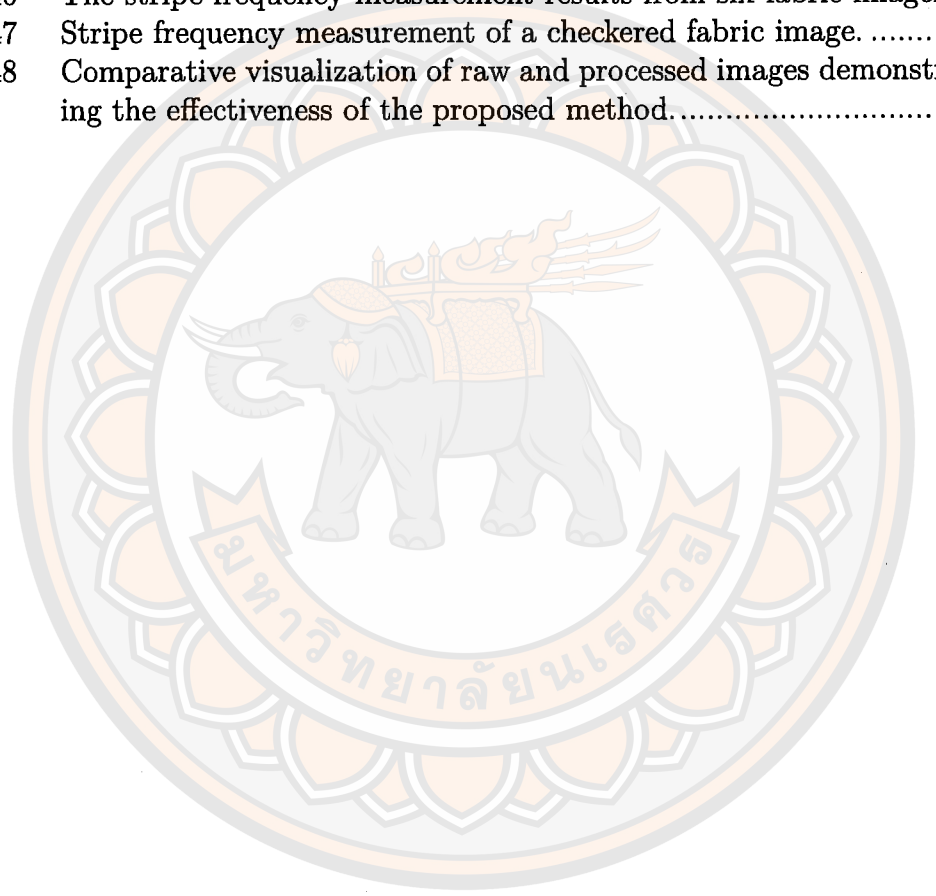

LIST OF TABLES

Table **Page**

CHAPTER I

INTRODUCTION

1.1 Motivation

In the textile industry, an important parameter used to determine fabric quality and pricing is the number of threads per unit area, commonly referred to as "Thread Density" or "Thread Count." To prevent false advertising by textile manufacturers, various devices have been developed to measure thread density continuously. Initially, these devices were relatively simple, such as using a magnifying glass along with a rectangular frame to define the counting area. In addition, a small needle was used to assist in counting the threads. However, these traditional tools had significant limitations, especially regarding practical use, as they required high levels of concentration and meticulousness. This could lead to user fatigue and counting errors, causing low measurement accuracy due to potential human judgment errors.

Subsequently, a device called the "Overlay Thread Counter" was developed, utilizing the phenomenon known as the "Moiré Pattern." This device employs a transparent sheet with opaque stripes arranged in straight lines. The number of opaque stripes per unit area increases or decreases linearly from left to right. When this transparent sheet is overlaid on the fabric to be inspected, straight and curved patterns appear on the sheet. The straight lines that emerge directly indicate the thread density of the fabric. However, this technique still faces challenges in interpretation because the occurrence of the Moiré Pattern is often accompanied by high-frequency components, which may lead to inaccurate analysis of thread density. Therefore, eliminating the high-frequency components is crucial for developing more precise and reliable techniques.

From the research of [1], it was found that using logical operators (AND, OR) could effectively simulate the superposition of binary gratings. Furthermore,

Fourier series expansion was applied to analyze spatial frequencies that arise from the pattern. Particularly in the case where the duty cycle of the binary signal is 50%, the logical operators produce a triangular waveform that significantly eliminates the impact of high-frequency components. This technique led to the development of a Moving Average Filter to eliminate high-frequency signals, functioning as a low-pass filter to effectively remove noise. As a result, the generated Moiré Pattern becomes a low-frequency component that is easier to interpret, enhancing the accuracy of thread density measurement. Moreover, these techniques are suitable for measuring the frequency of sinusoidal voltage signals [2]. Additionally, for measuring the frequency of a rectangular voltage signal, a phase-locked loop circuit [3] and a microcontroller is commonly employed. These methods ensure precise and efficient frequency measurement in electrical and electronic systems.

In response to these challenges, this research aims to develop techniques for analyzing thread density and explaining the formation of the Moiré pattern through theoretical modeling and digital signal processing. By integrating logical operators with image processing and frequency analysis, we propose a method to eliminate high-frequency noise and improve the accuracy of thread counting. The outcome is a prototype of a low-cost, modern, accurate, user-friendly, and reliable device for measuring fabric density, particularly suitable for industrial settings. This research not only minimizes errors associated with traditional counting tools but also enhances the efficiency and practicality of fabric inspection processes in the textile industry.

1.2 Objectives

1. Develop a mathematical model to describe Moiré pattern formation in binary gratings, using logical operators (AND, OR, NOR).
2. Investigate the effects of duty cycle, frequency, and phase on the re-

sulting Moiré pattern.

3. Apply Fourier series analysis and low-pass filtering to extract relevant frequency components from Moiré patterns.
4. Apply the Moving Average Filter to reduce high-frequency components.
5. Implement a computer-based image processing algorithm for automated thread counting in fabric samples.

1.3 Scope of the thesis

To validate the analysis results, we will utilize the principle of image processing with a computer as the processor, along with a combination of a computer and a camera as the main equipment, to develop a set of devices for counting the number of threads per unit area of fabric. In addition, the analysis will include the examination of the Moiré Pattern generated from parallel binary gratings to understand the formation and behavior of the pattern. We will also study the effects of duty cycle, frequency, and initial phase on the occurrence of the Moiré Pattern. To ensure accuracy and robustness, we will employ computer simulations combined with image processing techniques to test the performance and validate the proposed methodology.

1.4 Basic concepts

The analysis and explanation of the Moiré pattern for thread counts per area are based on the concept that the presence and absence of threads are represented by rectangular signals with a certain duty cycle value. When introducing a pattern with a specific value (comparable to another rectangular signal) and applying it to the fabric image, it can be compared with an OR operation (or AND operator) using the Fourier series distribution technique of both signals and implemented in logic.

This will produce an output signal with a frequency proportional to the difference in frequency of the two initial signals. Such analysis can be used to determine the frequency or number of threads per unit area of the fabric for further examination.

1.5 Thesis details

In this thesis outline, the content is divided into five chapters, with details of each chapter as follows.

Chapter I Introduction: This chapter introduces the motivation for improving thread density measurement in textiles by using Moiré pattern analysis. It outlines the objectives involving logical operators, Fourier series, and filtering techniques, defines the research scope using image processing and computer simulations, and explains the conceptual basis using rectangular signals to model thread presence and analyze frequency differences.

Chapter II Theory and Literature Reviews: This chapter presents the theoretical basis and prior research related to Moiré pattern analysis. It begins with the concept of sound wave beats as an analogy for understanding frequency differences, followed by the formation of Moiré patterns using binary gratings. Mathematical modeling with rectangular signals and logical operators is introduced, along with the application of Fourier series for spatial frequency analysis. The chapter concludes with related work on oscillator-based beat detection and logic gate modeling.

Chapter III Moiré Pattern Analysis Using Logical AND and OR: This chapter explores the formation of Moiré patterns through the superposition of rectangular binary gratings, modeled as periodic signals representing the opaque and transparent regions of a structure. Logical operations (AND and OR) are applied to simulate the interaction between the Base and Revealing layers, with mathematical expressions derived using Fourier series. The chapter examines how varying frequency, phase, and duty cycle influence the resulting pattern and demonstrates

through simulation the theoretical conditions under which low-frequency structures emerge within the composite signal.

Chapter IV Moiré Pattern Application for Stripe Measurement: This chapter presents a method for measuring stripe density by superimposing computer-generated grid lines onto fabric images to create Moiré patterns. The pattern formation depends on several parameters, including stripe frequency, duty cycle, and phase alignment. To analyze the resulting patterns, image processing techniques such as thresholding and the moving average filter are applied to eliminate high-frequency components and extract useful signals. The proposed method enhances measurement accuracy and offers a reliable solution for automated stripe counting in practical textile applications.

Chapter V Summary: This chapter provides a synthesis of the findings presented in the previous chapters. It first summarizes the theoretical analysis of binary grating overlaps using logical operators, highlighting the conditions that give rise to low-frequency components. It then reviews the practical application of Moiré patterns for stripe density measurement, emphasizing the effectiveness of image-based filtering techniques in extracting meaningful signals for automated analysis.

CHAPTER II

THEORY AND LITERATURE REVIEWS

2.1 Theoretical

2.1.1 Sound Wave Beats Phenomenon

One important idea in carrying out this thesis is the Moiré pattern formation. Some aspects are similar (analogous) to the phenomenon of Beats in sound waves. Therefore, the first part of the second chapter reviews knowledge about Beat formation in sound waves and how to analyze the frequency of these Beats, which can be explained as follows.

The Beat phenomenon of sound waves is caused by two sound waves with slightly different frequencies arriving at the observer's ear, as shown in Figure 1, where the observer hears a sound with a frequency equal to the average of the two waves. However, the sound will alternate loudly and softly in a continuous rhythm. The frequency of this alternating loudness is called the Beat frequency (Beat Frequency; f_B), which is equal to the difference in frequency of the two waves.

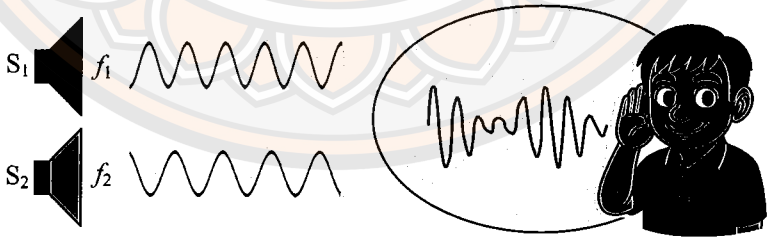

Figure 1 Sound wave representation of the beats phenomenon

For expressing the calculation of beat frequency, it's typically analyzed using the wave equation and the algebraic combination of the two waves, as follows:

$$Y_1 = A\cos(2\pi f_1 t) \tag{2.1}$$

$$Y_2 = A\cos(2\pi f_2 t) \tag{2.2}$$

Where Y_1 and Y_2 the first and second sound waves' equations, A is the amplitude of each waves, t is time, and f_1 and f_2 are the frequencies of the first and second sound waves. The combination of the two waves at the observer's ear position is as follows:

$$Y = Y_1 + Y_2 = 2A\cos(2\pi(\frac{f_2 - f_1}{2})t)\cos(2\pi(\frac{f_2 + f_1}{2})t) \tag{2.3}$$

From equation (2.3), the term $\cos(2\pi(\frac{f_2+f_1}{2})t)$ represents the cosine function with high-frequency values. The observer hears the sound as the average of the values f_1 and f_2. Meanwhile, the term $2A\cos(2\pi(\frac{f_2-f_1)}{2})t)$ can be regarded as the amplitude of the sound signal Y. This term causes the amplitude to change between 0 and $2A$ twice within 1 second (equal to twice the value of $(\frac{f_2-f_1}{2})$). Therefore, the beat frequency (f_{beat}) of the sound wave that occurs will have a value of

$$f_{beat} = |f_2 - f_1| \tag{2.4}$$

In addition to using equations (2.1) to (2.3) to analyze beat frequency values, another approach is to rely on the timing diagram of the wave signal, as shown in Figure 2, to display each wave's phase. It is assumed that the frequencies of the two waves are not significantly different from the beat frequency ($f_1 = 20$ Hz and $f_2 = 22$ Hz). In the initial condition, the two sound waves have an initial phase difference of 0, which will change over time. However, at time intervals of 0.25, 0.50, 0.75, and 1.00 second, the two waves will have phase differences of π, 0, π, and 0, respectively. When both waves have a phase difference of 0, the sum of the two waves will have the highest amplitude (resulting in the loudest sound), whereas a phase difference of π will lead to the sum of the two waves having the lowest amplitude (resulting in the softest sound). The diagram shows that the beat frequency value (beat) equals 2 Hz, which is equal to the absolute value of the frequency difference of the two original sound waves, as shown in equation (2.4).

The equation in terms of the signal period can be written as

$$T_{beat} = \frac{1}{f_{beat}} = \frac{T_1 T_2}{|T_1 - T_2|} \tag{2.5}$$

Where T_{beat}, T_1, and T_2 represent the beat period, the period of the first wave, and the period of the second wave, respectively.

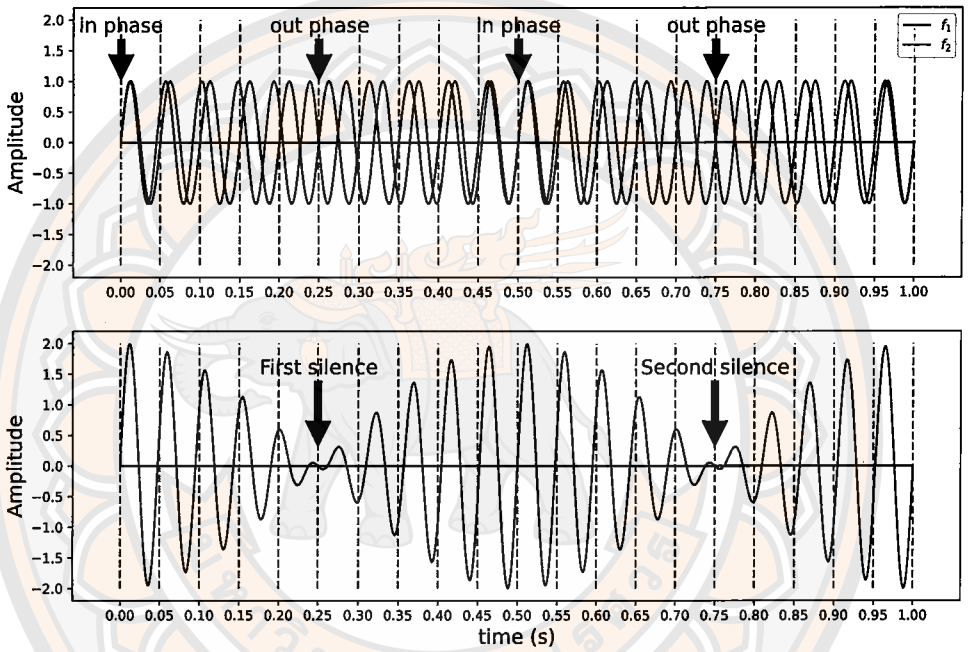

Figure 2 Beat frequency analysis of an audio wave using timing diagrams.

2.1.2 Moiré pattern

A simple Moiré pattern can be created by stacking two translucent panels on top of each other, where both panels have opaque lines (alternating translucent sections) in different areas. The translucent sheet at the bottom is called the "Base layer," while the translucent sheet at the top is called the "Revealing layer." When the observer looks at the top of the two translucent layers, they will see dark bands alternating with bright bands, similar to the interference of light waves. The frequency of alternating dark bands with bright bands equals the frequency

difference in the number of opaque lines on the two translucent sheets, as illustrated in the example in Figure 3.

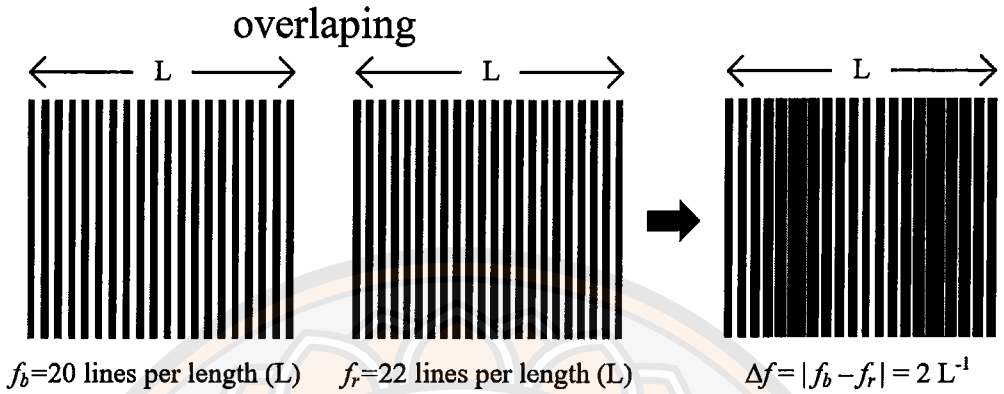

Figure 3 Demonstration of Moiré pattern formation using binary gratings.

In Figure 3, a simple Moiré pattern appears when the Base layer and the Revealing layer have different frequencies (per unit length) of constant opaque lines. The orientation of the Base and Revealing layers is at an angle of zero degrees. However, in cases where the Base layer and the Revealing layer are arranged at angles other than zero, a different pattern will result, as shown in Figure 4. Additionally, Figure 5 shows the scenario where the Base and Revealing layers consist of circular lines.

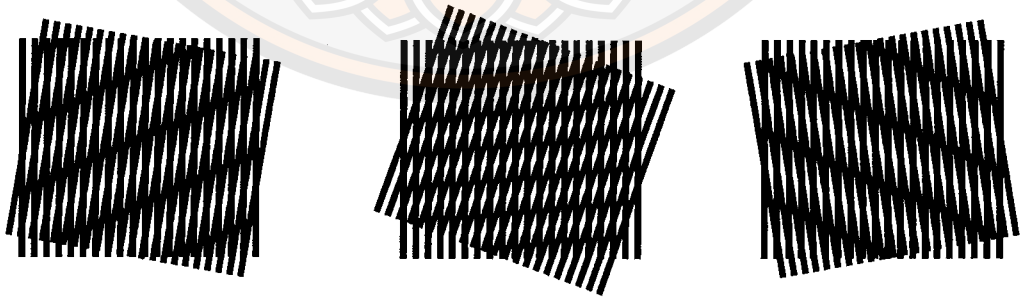

Figure 4 The difference between the base and revealing layers arises from angular alignment.

The Moiré pattern phenomenon has been applied in various fields. For example, it is used for counting the number of threads per unit area of fabric since

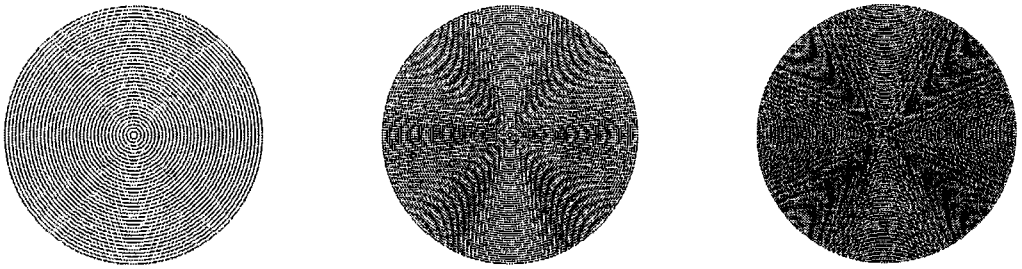

Figure 5 Moiré pattern where the Base and Revealing layers consist of circular lines.

the mid-2005s [4], for creating simple animations [5], for generating and reading image codes on material surfaces [6], and for inspecting the structure of objects [7], among others.

As shown in Figure 6, an example of applying the Moiré pattern phenomenon for counting the number of threads per unit area of fabric is presented. This concept involves using the fabric as the Base layer and an instrument called the "Overlay Thread Counter" as the Revealing layer. The Overlay Thread Counter is a transparent sheet with non-uniform opaque stripe frequency (varying from 30 lines per inch on the left side, gradually increasing to 50 lines per inch on the right side). In this case, the sample fabric used has a thread density of 44 lines per inch.

When the Overlay Thread Counter is placed over the fabric, the observer will see alternating dark and bright bands, as illustrated in the figure. By examining the frequency scale on the Overlay Thread Counter, it is found that at other frequency values, the pattern shows continuous alternating dark and bright bands. However, at the specific frequency of 44 lines per inch, the pattern appears as a continuous dark band across the entire sheet. This indicates that the frequency difference between the Base and Revealing layers is zero at this point.

2.1.3 Frequency analysis of opaque linear Moiré patterns with a fixed frequency

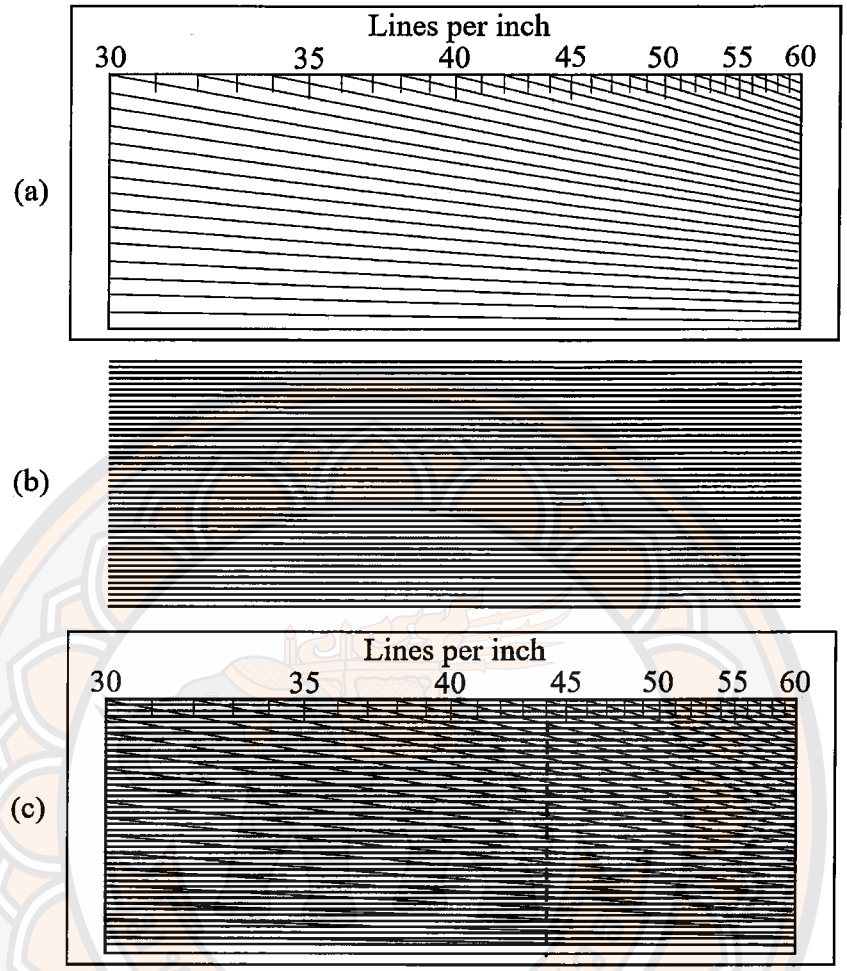

Figure 6 Application of Moiré patterning for thread count per area of fabric. (a) Overlay Thread Counter. (b) Example of thread lines (44 lines per inch). (c) Moiré pattern formed after placing the Overlay Thread Counter.

In Figure 3, it is illustrated that the Base layer and the Revealing layer have frequencies represented by opaque lines, with $f_b = 20$ lines per length and $f_r = 22$ lines per length, respectively. Consequently, the frequency of the dark and bright bands (f_m) is equal to 2 strips per length. This relationship can be expressed as follows:

$$f_m = |f_r - f_b| \tag{2.6}$$

Where f_b and f_r represent the frequencies (per length) of the opaque lines

on the Base and the Revealing layer, respectively. As defined in equation (2.6), the resulting Moiré pattern exhibits dark and bright bands with a frequency equal to the absolute value of the difference in frequencies of the opaque lines on the Base and the Revealing layer. This phenomenon can be likened to the occurrence of Beats in a sound wave when depicted in a time diagram, or time domain. An analysis of the relationship of this phenomenon has been presented in a research article [5], which can be explained as follows.

As shown in Figure 7, assume that the Base and the Revealing layer have a duty cycle value (the ratio between the distance occupied by the opaque line to the total distance between opaque lines) equal to 0.5 or 50%. In this case, the Base and the Revealing layer have a opaque line frequency value per unit length equal to f_b and f_r, respectively, assuming that $f_r > f_b$. Therefore, both layers will have the distance between the opaque lines given by $T_b = 1/f_b$ and $T_r = 1/f_r$, respectively. The opaque lines from both layers are perfectly overlapped at the starting position (as if both sound waves have the same initial phase).

When the observer looks at this area, the average brightness at the next location is approximately 50% (as the opaque and transparent lines have the same width). The phase of the opaque lines of the Revealing layer begins to precede the phase of the opaque line in the Base region because $f_r > f_b$. When reaching the position where the opaque line of the Revealing layer leads the Base region by approximately π, the observer will perceive that area as a completely dark band. Then, at further positions, the phase of the opaque line of the Revealing layer continues to advance relative to the opaque line of the Base region until both layers are in phase again. From this relationship, $T_m = 1/f_m$ is defined as the distance between the bright and bright areas. (or the distance between the dark area and the dark area) will be

$$\frac{T_m}{T_r} = \frac{T_m}{T_b} + 1 \tag{2.7}$$

Whether $f_r > f_b$ or $f_b > f_r$, the pattern of dark and bright bands will be the same. Therefore, from equation (2.7), we will get the relationship

$$T_m = \frac{T_r T_b}{|T_b - T_r|} \tag{2.8}$$

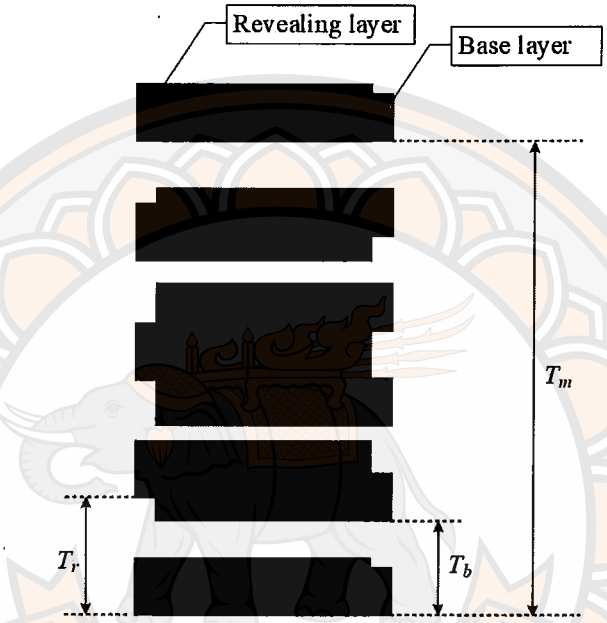

Figure 7 Implementation of Moiré patterning to measure fabric thread count per unit area.

From equations (2.8) and (2.5), it can be seen that they are similar. And when changing the relationship into frequency form, we get

$$f_m = \frac{1}{T_m} = |f_r - f_b| \tag{2.9}$$

2.1.4 Preliminary Fourier Analysis of Square Wave Signals

The Fourier analysis of square wave signals provides a fundamental method for understanding time-domain periodic binary waveforms. In this context, we consider a square wave function denoted as $Q_A(t)$, where the amplitude alternates between 0 and 1 with a specified duty cycle δ. The duty cycle represents the proportion of the period during which the signal remains at a high level (amplitude

= 1), while the remaining portion of the period remains at a low level (amplitude = 0). Assuming a period of $T = 2\pi$, the square wave function can be defined as:

$$Q_A(t) = \begin{cases} 1, & \text{if} \quad 0 \leq t < 2\pi\delta \\ 0, & \text{if} \quad 2\pi\delta \leq t < 2\pi \end{cases} \tag{2.10}$$

Given that $Q_A(t)$ is periodic with period 2π, it can be expressed as a Fourier series:

$$Q_A(t) = a_0 + \sum_{n=1}^{\infty} [a_n \cos(nt) + b_n \sin(nt)] \tag{2.11}$$

To determine the Fourier coefficients, we begin with the constant term a_0:

$$a_0 = \frac{1}{2\pi} \int_0^{2\pi} Q_A(t)\, dt = \frac{1}{2\pi} \int_0^{2\pi\delta} 1\, dt = \delta \tag{2.12}$$

The coefficient a_n is given by:

$$a_n = \frac{1}{\pi} \int_0^{2\pi} Q_A(t) \cos(nt)\, dt = \frac{1}{\pi} \int_0^{2\pi\delta} \cos(nt)\, dt = \frac{1}{\pi} \cdot \frac{\sin(2\pi n\delta)}{n} \tag{2.13}$$

The coefficient b_n is:

$$b_n = \frac{1}{\pi} \int_0^{2\pi} Q_A(t) \sin(nt)\, dt = \frac{1}{\pi} \int_0^{2\pi\delta} \sin(nt)\, dt = \frac{1}{\pi} \cdot \frac{1 - \cos(2\pi n\delta)}{n} \tag{2.14}$$

In the case where $\delta = 0.5$, substituting this value into the expressions for the Fourier coefficients results in $a_n = 0$ for all n due to the sine term $\sin(2\pi n\delta)$ vanishing. For the sine coefficients, $b_n = 0$ when n is even, since $\cos(2\pi n\delta) = \cos(\pi n) = 1$. The remaining non-zero terms occur when n is odd. By substituting a_0, a_n, and b_n into the Fourier series expression, we obtain:

$$Q_A(t) = \frac{1}{2} + \frac{2}{\pi} \sum_{n=1,3,5,\ldots}^{\infty} \frac{1}{n} \sin(nt) \tag{2.15}$$

This result reveals that the symmetric square wave signal consists solely of odd sine harmonics with decreasing amplitude. This compact representation is widely used in time-domain signal processing and forms a foundation for subsequent analysis involving logic gate operations on square wave signals.

2.2 Literature Review on Moiré Pattern Analysis

The Moiré effect has long been recognized as an important phenomenon in measurement systems and optical analysis. Since the late 19th century, numerous studies have examined its properties and applications. These include surface inspection, defect detection, mechanical property measurement, and vibration analysis [8, 9, 10, 11, 12]. The core principle relies on the interference pattern generated when two sets of periodic lines overlap. This pattern provides insight into the relative differences in frequency, angle, and alignment between the layers involved.

A wide range of analytical methods has been proposed to study Moiré patterns. These include geometric methods, which are intuitive and suitable for estimating the period and intersection of tilted gratings [13], algebraic methods that model continuous sinusoidal gratings [14], and spectral approaches that employ Fourier series for analyzing binary grating structures [15]. Each technique reveals different aspects of the frequency content and structure of the observed pattern. Recent research often combines multiple methods to enhance analytical precision, such as time-averaged Fourier transforms [16], reciprocal vector models [17], and phase-space representations [18].

One of the most common applications of the Moiré effect is in measuring stripe density. Traditional approaches are typically categorized into direct and indirect methods. Direct counting requires manual observation using magnification tools, but this method is limited by the operator's visual capacity and is prone to fatigue and inconsistency [19]. Indirect methods, on the other hand, use auxiliary tools such as Moiré gratings or optical systems to convert the visual pattern into measurable data. For example, a translucent grating sheet with varying density can be overlaid on the target surface. The appearance of a straight Moiré band indicates a match in density, allowing users to estimate the value using a calibrated

scale [20].

The advancement of computer technology has led to the development of digital methods that improve both accuracy and repeatability. Techniques now exist that analyze digital images of stripe patterns using signal processing methods. These include calculating the distance between adjacent stripes in pixel units [21, 22], counting the number of stripes over a fixed distance [23, 24], and applying Fourier Transform techniques to extract dominant frequency components [25, 26, 27]. While each approach has merits, their accuracy often depends on image resolution and pattern regularity.

Comparing these techniques is complicated by differences in image quality and testing conditions. However, several studies report high accuracy under controlled settings. In [28], the simulation error was below 0.2 percent and experimental error within 1.8 percent. Similarly, [29] achieved a maximum error of 0.4 percent in plain weave and 0.75 percent in twill fabric. These results demonstrate the potential of Moiré-based methods when appropriate preprocessing and filtering are applied, particularly in fields such as textile analysis, optical inspection, and image-based metrology.

2.3 Related Work

2.3.1 Metal Detector Oscillator Frequency Beats

Beat Frequency Oscillator Metal Detector [30, 31, 32, 33] is a device for detecting metal or metal-containing objects. It is based on a principle similar to the formation of Beats in sound waves. Still, the difference is that the signal frequency of the two signal generators used in the system is usually designed to be higher than the frequency that humans can hear. For example, it is set to be higher than 90-100 kHz or more. Figure 8 shows an example block diagram of a typical Beats frequency oscillator metal detector. It consists of two signal generator circuits,

a mixer circuit, a filter circuit, an amplifier circuit, and a speaker for displaying measurement results. The first signal generator generates a voltage signal with a constant frequency. To serve as the system reference frequency, a second signal generator has a search coil connected to the signal generator. The second signal generator has search coils connected as part of the signal generator. In the initial state, the frequency values of the voltage signals from both signal generators are set to be equal. When metal or metal-containing objects are brought near the search coil, It will cause the frequency values of the two voltage signals obtained from the signal generator at 2 to change. A signal mixing circuit coupled with a frequency filter detects the difference in frequencies of the signals from the two signal generators. This results in a voltage signal equal to the frequency difference, similar to the sound wave's Beats. The frequency that comes out of this filter circuit is in the range that humans can hear. After that, the signal amplification circuit makes the signal bigger to send to the speaker.

The classification of Beats frequency oscillator metal detectors, based on signal format, can be divided into two categories. These categories encompass signals utilized within the system, such as sine wave signals and square wave signals. In the case of a sine wave signal, a mixed signal circuit can be constructed by combining two signals and passing the resultant signal through a rectifier to obtain the absolute value. For square signals, the circuit detects the frequency difference. This involves employing a D-type flip-flop connected to a high-pass filter [34] and a NAND-Gate connected to a low-pass filter [35].

2.3.2 Analysis of the frequency difference of a rectangular signal using logic gates

In previous studies, it has been shown that not only NAND gates and Exclusive OR gates, which are commonly used for detecting frequency differences in phase-locked loop (PLL) circuits [3], but also other types of logic gates can be uti-

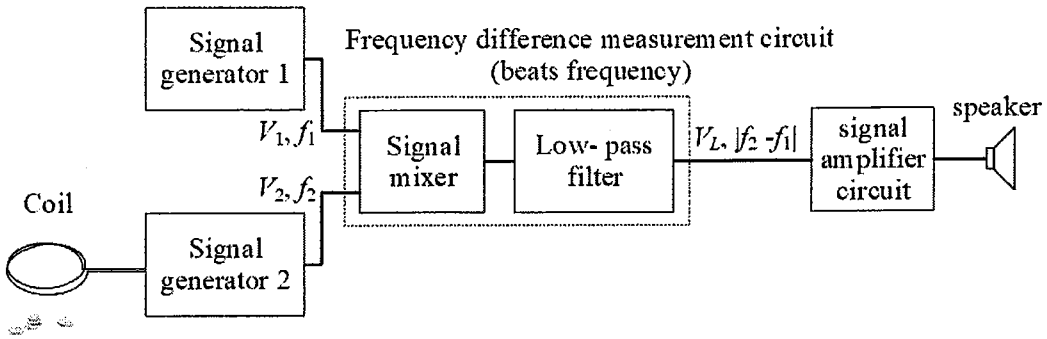

Figure 8 Block diagram illustrating the beat frequency principle in a metal detector.

lized for measuring the frequency difference of a rectangular signal when combined with a low-pass filter circuit (as illustrated in Figure 9). This study aims to utilize the Fourier series distribution of rectangular signals from two sources. Considering that these two signals are logic signals with logical magnitude values of "0" and "1", and relying on the operational characteristics of each type of logic gate as shown in Table 1, by leveraging their respective properties to perform various tasks, this corresponds to the algebraic representation shown in Table 2.

Table 1 Truth table of 6 types of logic gates

Input		**Output**					
Q_A	Q_B	AND-gate	NAND-gate	NOR-gate	OR-gate	XOR-gate	XNOR-gate
0	0	0	1	1	0	0	1
0	1	0	1	0	1	1	0
1	0	0	1	0	1	1	0
1	1	1	0	0	1	0	1

An example of circuit analysis involves using AND-Gate logic gates connected with a low-pass filter circuit. Let Q_A and Q_B be rectangular logic signals with a maximum value of "1" and a duty cycle of 0.5. Both signals have frequencies f_A and f_B, respectively, resulting in the Fourier series representation of the two

Table 2 Equivalent function of 6 logic gates

Logic gate	Equivalent function
AND	$Q_{G(\text{AND})} = Q_A Q_B$
NAND	$Q_{G(\text{NAND})} = 1 - Q_A Q_B = 1 - Q_{G(\text{AND})}$
NOR	$Q_{G(\text{NOR})} = (1 - Q_A)(1 - Q_B)$
OR	$Q_{G(\text{OR})} = 1 - [(1 - Q_A)(1 - Q_B)] = 1 - Q_{G(\text{NOR})}$
XNOR	$Q_{G(\text{XNOR})} = Q_A Q_B + (1 - Q_A)(1 - Q_B)$
XOR	$Q_{G(\text{XOR})} = 1 - [Q_A Q_B + (1 - Q_A)(1 - Q_B)] = 1 - Q_{G(\text{XNOR})}$

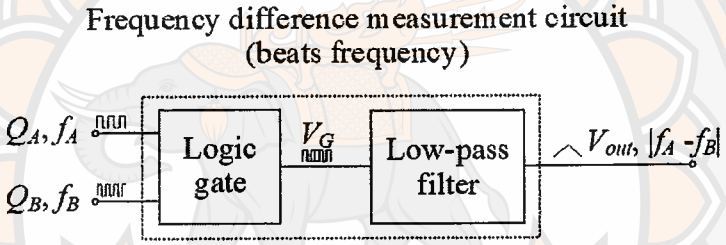

Figure 9 Detection of frequency difference in rectangular signals using logic gates and a low-pass filter.

signals as follows:

$$Q_A = \frac{1}{2} + \frac{2}{\pi}\sum_{n=1}^{\infty}\frac{1}{n}\sin(n\omega_A t) \quad ; n = 1, 3, 5, \ldots \tag{2.16}$$

$$Q_B = \frac{1}{2} + \frac{2}{\pi}\sum_{m=1}^{\infty}\frac{1}{m}\sin(m\omega_B t) \quad ; m = 1, 3, 5, \ldots \tag{2.17}$$

where $\omega_A = 2\pi f_A$, $\omega_B = 2\pi f_B$, and t represents time in seconds. Table 2 provides the AND gate logic.

$$\begin{aligned} Q_{G(\text{AND})} &= Q_A Q_B \\ &= \left(\frac{1}{2} + \frac{2}{\pi}\sum_{n=1}^{\infty}\frac{1}{n}\sin(n\omega_A t)\right)\left(\frac{1}{2} + \frac{2}{\pi}\sum_{m=1}^{\infty}\frac{1}{m}\sin(m\omega_B t)\right) \end{aligned} \tag{2.18}$$

and given that $\omega_A = \omega_B + \Delta\omega$ will get

$$\begin{aligned} Q_{G(\text{AND})} &= \frac{1}{4} + \frac{1}{\pi}\sum_{n=1}^{\infty}\frac{1}{n}\sin(n\omega_A t) + \frac{1}{\pi}\sum_{m=1}^{\infty}\frac{1}{m}\sin(m\omega_B t) \\ &\quad + \frac{2}{\pi^2}\sum_{n=1}^{\infty}\sum_{m=1}^{\infty}\frac{1}{nm}\left[\cos((n-m)\omega_B t + n\Delta\omega t)\right] \\ &\quad - \frac{2}{\pi^2}\sum_{n=1}^{\infty}\sum_{m=1}^{\infty}\frac{1}{nm}\left[\cos(n\omega_A t + m\omega_B t)\right] \end{aligned} \tag{2.19}$$

According to equation (2.19), when f_A and f_B are significantly higher than $|f_A - f_B|$, the low-pass filter can ideally function. This implies that the high-frequency components of the signal, f_A and f_B and those above, are eliminated. Consequently, a voltage signal will emerge from the low-pass filter circuit with a value of

$$\begin{aligned} V_{L(\text{AND})} &= \frac{1}{4} + \frac{2}{\pi^2}\sum_{i=1}^{\infty}\frac{1}{i^2}\cos(i\Delta\omega t) \\ &= \frac{1}{4} + \frac{2}{\pi^2}\sum_{i=1}^{\infty}\frac{1}{i^2}\cos(i2\pi|f_A - f_B|t) \quad ; i = 1, 3, 5, \ldots \end{aligned} \tag{2.20}$$

Equation (2.20) corresponds to the Fourier series of a triangular signal with a frequency equal to the frequency difference between Q_A and Q_B. This signal includes a DC component equal to 1/4 (equivalent to 1/4 times the voltage; for instance, it is 1/4 of 5V when the Logic Gate is 5V).

Similarly, for other logic operations, by substituting equations (2.16) and (2.17) with the properties outlined in Table 2, along with considering the operational characteristics of the low-pass filter circuit, the output of the circuit can be obtained using each of the remaining Logic Gates as follows

NAND-gate :

$$V_{L(\text{NAND})} = \frac{3}{4} - \frac{2}{\pi^2}\sum_{i=1}^{\infty}\frac{1}{i^2}\cos(i2\pi|f_A - f_B|t) \; ; i = 1, 3, 5, \ldots \tag{2.21}$$

NOR-gate :

$$V_{L(\text{NOR})} = \frac{1}{4} + \frac{2}{\pi^2}\sum_{i=1}^{\infty}\frac{1}{i^2}\cos(i2\pi|f_A - f_B|t) \; ; i = 1, 3, 5, \ldots \tag{2.22}$$

OR-gate :

$$V_{L(\mathrm{OR})} = \frac{3}{4} - \frac{2}{\pi^2}\sum_{i=1}^{\infty}\frac{1}{i^2}\cos(i2\pi|f_A - f_B|t)\ ; i = 1, 3, 5, ... \tag{2.23}$$

XNOR-gate :

$$V_{L(XNOR)} = \frac{1}{2} + \frac{4}{\pi^2}\sum_{i=1}^{\infty}\frac{1}{i^2}\cos(i2\pi|f_A - f_B|t)\ ; i = 1, 3, 5, ... \tag{2.24}$$

XOR-gate :

$$V_{L(\mathrm{XOR})} = \frac{1}{2} - \frac{4}{\pi^2}\sum_{i=1}^{\infty}\frac{1}{i^2}\cos(i2\pi|f_A - f_B|t)\ ; i = 1, 3, 5, ... \tag{2.25}$$

Figure 10 presents the experimental results obtained from a computer simulation using a 5V square wave signal with a duty cycle of 0.5. The input frequencies are set as $f_A = 100$ Hz and $f_B = 101$ Hz. The circuit configuration used to generate the input signals is shown in Figure 9, where various types of logic gates are applied to examine their roles as signal mixers. At the top of each subfigure in Figure 10, the corresponding input waveforms Q_A and Q_B, generated from this circuit, are displayed. The output signal exhibits a triangular waveform with a frequency equal to the difference between the two input signals, which is 1 Hz. Although the simulated voltage amplitude does not exactly match the analytical values, the results remain consistent with the equations (2.20) to (2.25), reflecting an equal attenuation ratio across all logic gates.

Figures 10(a)–(c) show the simulation results of various logic gates, as illustrated in each subfigure. The results consistently demonstrate that all gates produce a triangular output waveform with a frequency of 1 Hz, corresponding to the frequency difference $\Delta f = 1$ Hz. It can also be observed that each pair of outputs exhibits complementary behavior, reflecting the logical relationship between gate types. All logic gates consistently demonstrate signal mixing behavior aligned with the theoretical expectations.

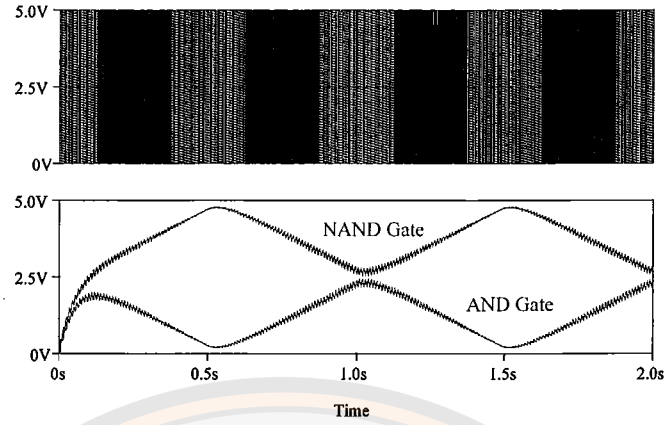

(a)

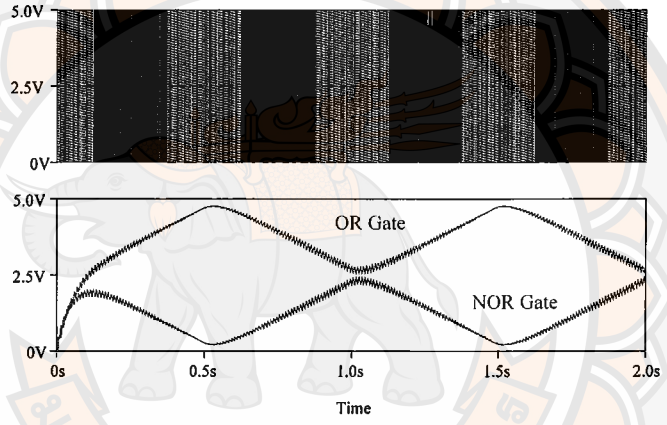

(b)

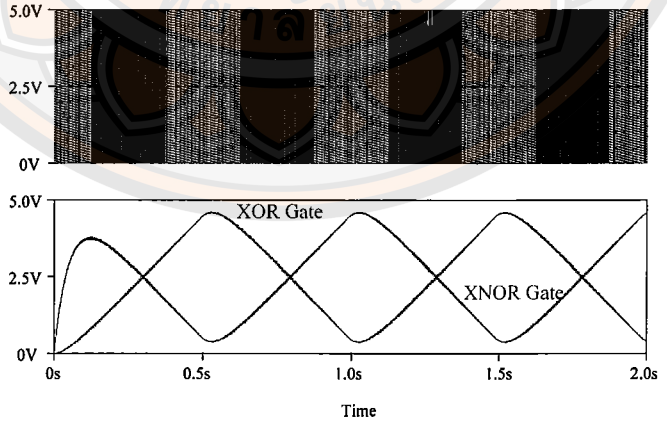

(c)

Figure 10 **Computer simulation results as shown in Figure 9 for $\Delta f = 1$: (a) AND and NAND gates; (b) OR and NOR gates; (c) XOR and XNOR gates.**

2.4 Chapter summary

This chapter provides the theoretical background and previous research that are essential to this study. It begins with the concept of beats in sound waves, where two waves with different frequencies combine and create a new pattern. The result is a variation in loudness that occurs at a frequency equal to the difference between the two original frequencies. This idea is useful for understanding the Moiré pattern, which is a similar effect but happens in space instead of time. The chapter then introduces the basic principles of Moiré patterns, which appear when two layers with slightly different line patterns are placed over each other. When this happens, a new visible pattern forms, showing alternating dark and bright bands. The frequency of these bands depends on how different the two layers are in terms of their line spacing. This principle has been used in several applications, such as counting threads in fabrics and detecting surface patterns. A simple frequency analysis of square wave signals is also presented. These signals can be expressed as a sum of sine and cosine terms using Fourier series. This method helps explain how the signal behaves over time and is important for later sections in the thesis. The square wave signals are then combined using logic gates like AND, OR, and XOR, and passed through low-pass filters to extract signals that depend on the frequency difference between the two inputs.

Finally, the chapter explains how these logic-based systems can detect frequency differences and produce output signals with clear patterns. The results of both theory and experiments show that this method works effectively and can be applied in real systems such as frequency-based metal detectors. In this thesis, it is hypothesized that the superposition of the base and revealing layers in the formation of Moiré patterns can be interpreted in terms of digital logic. The opaque lines are treated as logic "1" and the transparent spaces as logic "0." When the two layers are overlaid, the result is similar to an OR logic operation. After applying a

low-pass filter to the combined pattern, the resulting image is expected to resemble a triangular waveform, similar to the signals found in electronic circuits.

CHAPTER III

MOIRÉ PATTERN ANALYSIS USING LOGICAL AND AND OR

3.1 Overview of Moiré Pattern Analysis

In this chapter, the analytical framework for investigating Moiré patterns resulting from the superposition of parallel binary gratings is presented. The focus lies in exploring the effects of logical operations, particularly AND and OR operators, on the resulting waveform formed by overlapping rectangular binary signals. These binary signals represent opaque and transparent regions of the grating structures and are modeled using periodic rectangular waveforms. By applying logic operations to these signals, the interaction between the base and revealing layers can be theoretically analyzed, providing insights into the pattern formation process. The structure of this chapter begins with the definition and construction of rectangular binary signals, followed by the mathematical formulation of AND and OR operations. Subsequent sections simulate the superposition of binary gratings using both logic operators and analyze the corresponding output signals. The findings in this chapter lay the theoretical foundation for image-based Moiré analysis presented in the following chapters.

3.2 Rectangular Binary Signals and Logical Operators

In this study, a binary grating is defined using a rectangular waveform that alternates between logic values "1" and "0". The signal is a function of spatial position x, as illustrated in Figure 11. It starts at an initial phase ϕ_0 and has a period P. The values P_h and P_l represent the distances for which the signal remains at logic "1" and "0", respectively. Therefore, the total period is given by $P = P_h + P_l$. The spatial frequency is defined as $f = 1/P = 1/(P_h + P_l)$, and the angular frequency is calculated by $\omega = 2\pi f = 2\pi/P$.

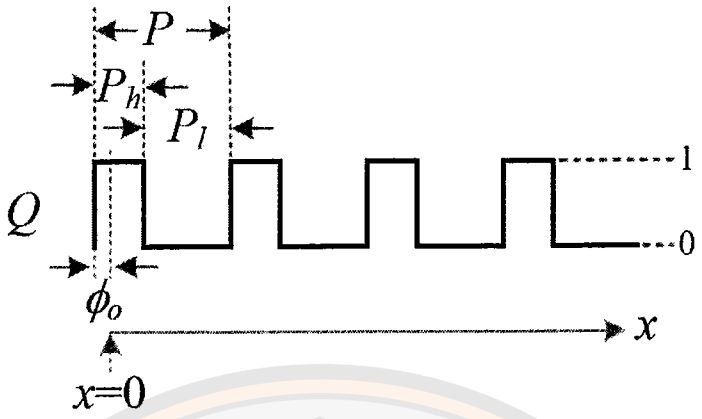

Figure 11 Rectangular binary signal representation

The *duty cycle* δ is defined as the ratio between the length of the signal at logic "1" and the total period, which can be written as:

$$\delta = \frac{P_h}{P} \tag{3.1}$$

To analyze the rectangular waveform in the frequency domain, a Fourier series expansion is used. The signal Q, as defined in Appendix ??, can be expressed as:

$$Q = \delta + \frac{1}{\pi}\sum_{n=1}^{\infty}\left(-\frac{1}{n}\sin(n(\omega x - 2\pi\delta + \phi_0))\right) + \frac{1}{\pi}\sum_{n=1}^{\infty}\left(\frac{1}{n}\sin(n(\omega x + \phi_0))\right) \tag{3.2}$$

In the special case where the initial phase $\phi_0 = 0$, and the signal has equal widths of logic "1" and logic "0" ($\delta = 0.5$), the waveform becomes symmetric and the Fourier series simplifies to:

$$Q = \frac{1}{2} + \frac{2}{\pi}\sum_{m=1,3,5,\ldots}^{\infty}\frac{1}{m}\sin(m\omega x) \tag{3.3}$$

To analyze the superposition of signals, the notations Q_A and Q_B are used to represent the input signals, while Q_{AND} and Q_{OR} represent the output signals obtained from the AND and OR operations, respectively. The logical behaviors of these operations have been previously discussed in [1], where the equivalent algebraic expressions are shown in Table 3 and defined by Equations (3.4) and (3.5) as follows:

Table 3 The logical truth tables of the AND and the OR operations are presented in [1]

Input		Output	
Q_A	Q_B	$Q_{\text{AND}} = Q_A$ AND Q_B	$Q_{\text{OR}} = Q_A$ OR Q_B
0	0	0	0
0	1	0	1
1	0	0	1
1	1	1	1
Equivalent algebraic equations:		$Q_{\text{AND}} = Q_A Q_B$	$Q_{\text{OR}} = Q_A + Q_B - Q_A Q_B$

$$Q_{\text{AND}} = Q_A Q_B \tag{3.4}$$

$$Q_{\text{OR}} = Q_A + Q_B - Q_A Q_B \tag{3.5}$$

As shown in Table 3, for the AND operation, the output is logic "1" only when both inputs are logic "1"; otherwise, the output is logic "0". In contrast, for the OR operation, the output is logic "0" only when both inputs are logic "0"; in all other cases, the output is logic "1". These differences in output behavior between the AND and OR operators will be further explained in the following section.

3.3 Overlap of Binary Gratings Based on Logical AND Operation

The overlapping between the Base and Revealing layers can be described as shown in Table 4. For the AND operator, the transparent area is considered equivalent to logic "0", while the opaque area is equivalent to logic "1." The superposition of the two layers is therefore analogous to the operation of an AND gate. However, one important difference between the two systems is that the electrical logic gate operates with respect to time, whereas the formation of the Moiré pattern is considered with respect to spatial position.

In addition, the analysis presented in [1] assumes that the duty cycle of the signal is fixed at 0.5. However, in the case of Moiré pattern formation, the duty cycle is not necessarily equal to 0.5. This variation in duty cycle affects the resulting analysis and may lead to different outcomes.

In this study, the Moiré pattern is analyzed using a model that mimics the behavior of an AND gate, where the duty cycle, initial phase, and spatial frequency are provided as input parameters. The conceptual diagram of this model is shown in Figure 12.

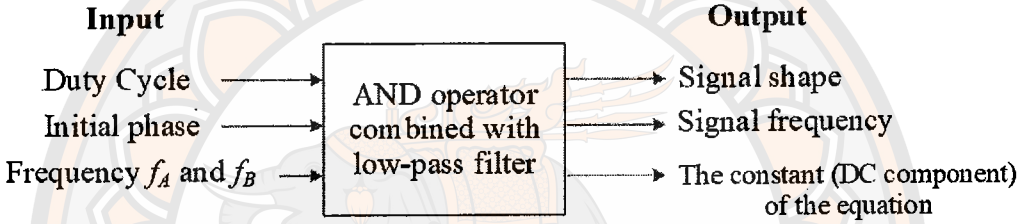

Figure 12 Analysis of Moiré pattern using the AND operator

Table 4 Effects of overlapping between Base and Revealing for AND -gates

AND-gate Input		AND-gate Output
Base	Revealing	Result
opaque (0)	opaque (0)	opaque (0)
opaque (0)	transparent (1)	opaque (0)
transparent(1)	opaque (0)	opaque (0)
transparent(1)	transparent (1)	transparent (1)

The overlapping between the gratings of the Base layer and the Revealing layer is illustrated in Figure 13. In general, the grating placed on top is the Revealing layer, which acts as a checker and can be designed by the user. Therefore, the signal of the Revealing layer is denoted by Q_r, and its duty cycle is set to 0.5

with an initial phase of zero ($\phi_0 = 0$). With these conditions, the Fourier series expansion of the signal follows Equation (3.3), and its angular frequency is given by $\omega_r = 2\pi f_r$.

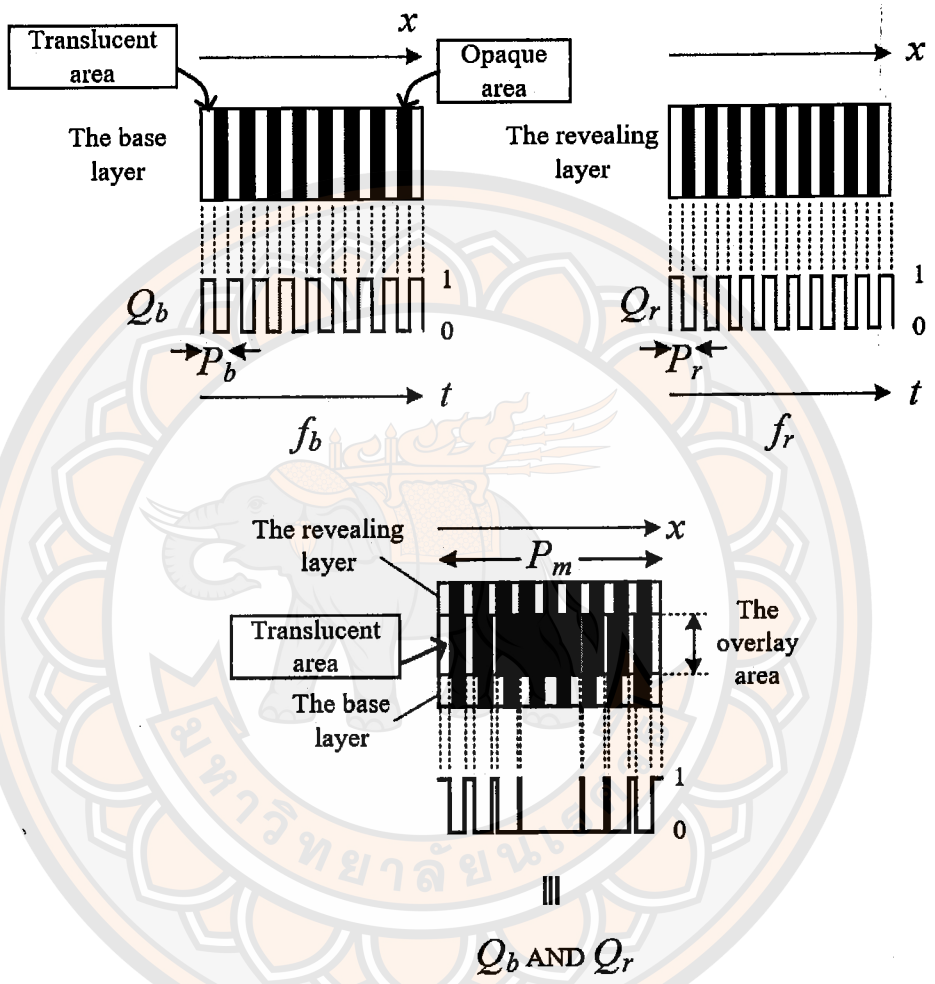

Figure 13 Analysis of Moiré pattern using the AND-operator

The Base layer represents the object being measured, such as the yarns in a fabric. As such, its duty cycle and initial phase cannot be predetermined. For this reason, the signal of the Base layer is denoted by Q_b, and its Fourier series expansion is described by equation (3.2), with an angular frequency $\omega_b = 2\pi f_b$.

The superposition of the two signals is modeled using the AND operator, as defined in Equation (3.4). By substituting the expressions for Q_b and Q_r, the

following relationships are obtained:

$$Q_b(x) = \delta + \frac{1}{\pi}\sum_{n=1}^{\infty}\left(-\frac{1}{n}\sin(n(\omega_b x - 2\pi\delta + \phi_0)) + \frac{1}{n}\sin(n(\omega_b x + \phi_0))\right) \tag{3.6}$$

$$Q_r(x) = \frac{1}{2} + \frac{2}{\pi}\sum_{m=1,3,5,\ldots}^{\infty}\frac{1}{m}\sin(m\omega_r x) \tag{3.7}$$

$$\begin{aligned} Q_{\text{AND}} &= Q_b Q_r \\ &= \left[\delta + \frac{1}{\pi}\sum_{n=1}^{\infty}\left(-\frac{1}{n}\sin(n(\omega_b x - 2\pi\delta + \phi_0))\right)\right. \\ &\quad \left. + \frac{1}{\pi}\sum_{n=1}^{\infty}\left(\frac{1}{n}\sin(n(\omega_b x + \phi_0))\right)\right] \\ &\quad \times \left[\frac{1}{2} + \frac{2}{\pi}\sum_{m=1}^{\infty}\left(\frac{1}{m}\sin(m\omega_r x)\right)\right] \end{aligned} \tag{3.8}$$

From equation (3.8), we expand the multiplication and regroup terms as follows:

$$\begin{aligned} Q_{\text{AND}} = \frac{\delta}{2} &+ L_1 + L_2 + L_3 \\ &+ \frac{2}{\pi^2}\sum_{m=1}^{\infty}\sum_{n=1}^{\infty}\left(-\frac{1}{nm}\sin\left(n(\omega_b x - 2\pi\delta + \phi_0)\right)\sin(m\omega_r x)\right) \\ &+ \frac{2}{\pi^2}\sum_{m=1}^{\infty}\sum_{n=1}^{\infty}\left(\frac{1}{nm}\sin\left(n(\omega_b x + \phi_0)\right)\sin(m\omega_r x)\right) \end{aligned} \tag{3.9}$$

where

$$L_1 = \frac{2\delta}{\pi}\sum_{m=1}^{\infty}\left(\frac{1}{m}\sin(m\omega_r x)\right) \tag{3.10}$$

$$L_2 = \frac{1}{2\pi}\sum_{n=1}^{\infty}\left(-\frac{1}{n}\sin(n(\omega_b x - 2\pi\delta + \phi_0))\right) \tag{3.11}$$

$$L_3 = \frac{1}{2\pi}\sum_{n=1}^{\infty}\left(-\frac{1}{n}\sin(n(\omega_b x + \phi_0))\right) \tag{3.12}$$

Applying the trigonometric identity $\sin A \sin B = \frac{1}{2}\cos(A - B) - \frac{1}{2}\cos(A + B)$, Equation (3.9) can be rewritten as:

$$Q_{\text{AND}} = \frac{\delta}{2} + L_1 + L_2 + L_3$$

$$+\frac{2}{\pi^2}\sum_{m=1}^{\infty}\sum_{n=1}^{\infty}\left(-\frac{1}{nm}\left[\frac{1}{2}\cos(n\omega_b x - n2\pi\delta + n\phi_0 - m\omega_r x)\right.\right.$$
$$\left.\left.-\frac{1}{2}\cos(n\omega_b x - n2\pi\delta + n\phi_0 + m\omega_r x)\right]\right)$$
$$+\frac{2}{\pi^2}\sum_{m=1}^{\infty}\sum_{n=1}^{\infty}\left(\frac{1}{nm}\left[\frac{1}{2}\cos(n\omega_b x + n\phi_0 - m\omega_r x)\right.\right.$$
$$\left.\left.-\frac{1}{2}\cos(n\omega_b x + n\phi_0 + m\omega_r x)\right]\right) \tag{3.13}$$

In equation (3.13), although the expression consists of several terms, it can be categorized into five distinct groups. The first group is the constant term $\delta/2$. The second group contains cosine functions whose frequency is equal to that of the Base layer (represented by L_2 and L_3). The third group includes cosine functions whose frequency corresponds to the Revealing layer (represented by L_1). The fourth group consists of cosine terms whose frequencies are equal to the sum of the Base and Revealing layer frequencies. The last group includes cosine terms whose frequencies correspond to the difference between the two layers.

In practice, the Base and Revealing layers generally have high spatial frequencies, while the frequency difference between them is relatively low. Although every term in equation (3.13) contributes to the resulting signal, it is hypothesized that the low-frequency components primarily influence the formation of the Moiré pattern.

To emphasize the visually perceptible features, a conceptual low-pass filter is applied by averaging the signal over one period, typically based on the average of the Base and Revealing layer periods. This approach removes high-frequency components and retains the dominant low-frequency structure. In signal processing terms, this is equivalent to applying an ideal low-pass filter.

Let $Q_{\mathrm{AND(L)}}$ denote the result of applying this ideal low-pass filtering to equation (3.13). In this process, the second through fourth groups of harmonic terms are discarded. From the fifth group, only terms with $m = n$ are retained,

because these terms generate frequency components equal to the difference between the angular frequencies of the Base and Revealing layers, that is, $|\omega_b - \omega_r|$. This frequency is typically low and corresponds directly to the dominant Moiré pattern observed in practice. On the other hand, when $m \neq n$, the resulting terms involve combinations such as $n\omega_b \pm m\omega_r$, which produce higher spatial frequencies. These components oscillate rapidly with respect to the spatial variable x and do not contribute significantly to the visually dominant structure of the Moiré pattern. Therefore, an ideal low-pass filter removes these high-frequency components, preserving only the low-frequency behavior responsible for the perceptual changes in the pattern.

3.3.1 Signal Overlap Analysis for the AND Operator when $f_b = f_r$

After obtaining the signal $Q_{\text{AND(L)}}$, which has been processed through the low-pass filtering step, this section analyzes the case where the signals Q_b and Q_r have equal frequencies. By substituting $m = n = i$ into equation (3.13), we obtain:

$$Q_{\text{AND(L)}} = \frac{\delta}{2} + \frac{1}{\pi^2}\sum_{i=1}^{\infty}\frac{-1}{i^2}\cos(i\phi_0 - i2\pi\delta) + \frac{1}{\pi^2}\sum_{i=1}^{\infty}\frac{1}{i^2}\cos(i\phi_0) \tag{3.14}$$

where $i = m = n = 1, 3, 5, \ldots$.

Case 1: AND Operator with $f_b = f_r$ and $\delta = 0.5$

By setting $\delta = 0.5$, equation (3.14) simplifies to:

$$Q_{\text{AND(L)}} = \frac{1}{4} + \frac{2}{\pi^2}\sum_{i=1,3,5,\ldots}^{\infty}\frac{1}{i^2}\cos(i\phi_0) \tag{3.15a}$$

$$= \frac{1}{2} - \frac{|\phi_0|}{2\pi} \tag{3.15b}$$

To show how equation (3.15a) transforms into equation (3.15b), we make use of the Fourier series expansion of the absolute value function $f(\phi_0) = |\phi_0|$, which is given in equation (3.16) as:

$$|\phi_0| = \frac{\pi}{2} - \frac{4}{\pi}\sum_{i=1,3,5,\ldots}^{\infty}\frac{1}{i^2}\cos(i\phi_0) \tag{3.16}$$

Rewriting equation (3.16) to isolate the summation term:

$$\sum_{i=1,3,5,\ldots}^{\infty} \frac{1}{i^2}\cos(i\phi_0) = \frac{\pi^2}{8} - \frac{\pi}{4}|\phi_0|$$

Substituting this result into equation (3.15a) yields:

$$Q_{\text{AND(L)}} = \frac{1}{4} + \frac{2}{\pi^2}\left(\frac{\pi^2}{8} - \frac{\pi}{4}|\phi_0|\right)$$

Simplifying:

$$Q_{\text{AND(L)}} = \frac{1}{2} - \frac{|\phi_0|}{2\pi}$$

This confirms that equation (3.15a) can be rewritten as equation (3.15b) by using the Fourier expansion of the absolute value function from equation (3.16).

To further confirm the equivalence between equations (3.15a) and (3.15b), both expressions are plotted and visually compared. Equation (3.15a) is evaluated numerically by summing the first 100 odd terms of the infinite series (i.e., $i = 1, 3, 5, \ldots, 199$), which provides a sufficiently accurate approximation. Equation (3.15b), on the other hand, is computed directly from its analytical expression involving the absolute value function $|\phi_0|$.

Figure 14(a) shows the result obtained from the series expansion in equation (3.15a), while Figure 14(b) illustrates the corresponding curve based on the analytical expression in equation (3.15b). Both plots are generated over the interval $\phi_0 \in [-\pi, \pi]$.

As seen from the comparison, the two curves are identical within numerical precision, validating the correctness of the transformation from the Fourier series to the analytical expression. This agreement not only confirms the mathematical derivation but also emphasizes the usefulness of the analytical representation for further analysis in the subsequent sections.

From equation (3.15b), it is evident that the magnitude of $Q_{\text{AND(L)}}$ depends explicitly on the initial phase ϕ_0. The function exhibits a triangular shape, with

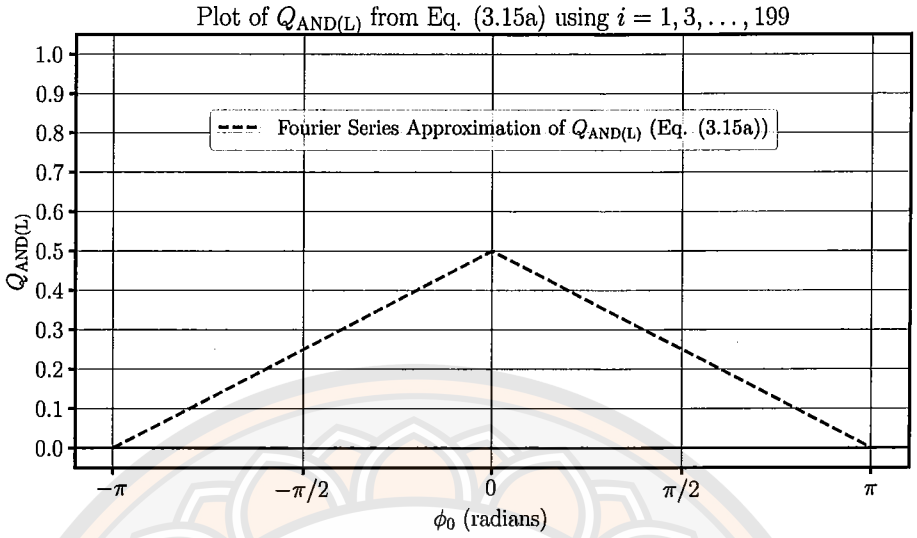

(a) Plot of $Q_{\text{AND(L)}}$ using the Fourier series in equation (3.15a).

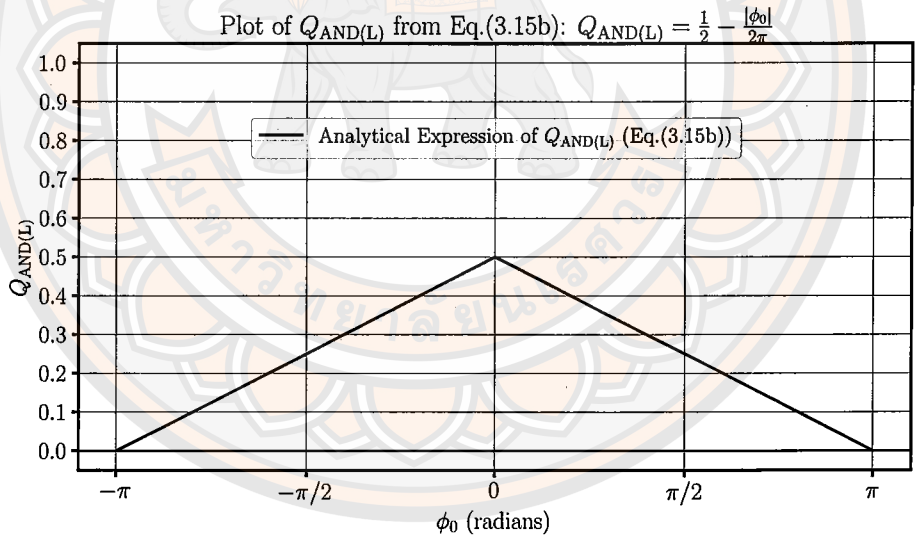

(b) Plot of $Q_{\text{AND(L)}}$ using the analytical expression in equation (3.15b).

Figure 14 **Comparison of $Q_{\text{AND(L)}}$ for $\Delta f = 0$, obtained from (a) the Fourier series approximation in equation (3.15a), and (b) the analytical expression in equation (3.15b).**

a maximum value of $1/2$, a minimum value of 0, and a median value of $1/4$. This range of variation, which spans from 0 to $1/2$ is the widest among all possible values of δ, highlighting the significance of the special case $\delta = 0.5$. When ϕ_0 is fixed, the perceived average brightness along the entire spatial domain remains constant and depends solely on the chosen initial phase. However, if ϕ_0 varies continuously over the interval $-\pi$ to π, such as through controlled relative motion between the Base and Revealing layers, the signal magnitude varies linearly and forms a triangular profile. This behavior provides insight into the phase-dependent nature of the resulting Moiré pattern, particularly under dynamic conditions.

Case 2: AND Operator with $f_b = f_r$ and arbitrary δ

While the case $\delta = 0.5$ leads to a compact analytical expression involving the absolute value function $|\phi_0|$, such simplification is no longer straightforward when δ takes on arbitrary values. In the general case, the term $\cos(i\phi_0 - i2\pi\delta)$ cannot be directly combined with $\cos(i\phi_0)$ as in the special case. Therefore, the resulting signal must be analyzed numerically or expressed as a double-cosine series, which captures the combined effects of both the duty cycle and the phase shift. This leads to more complex brightness variations that depend explicitly on the value of δ, as will be analyzed in the following section.

Starting from equation (3.14), we proceed with the analysis in the general case where δ is arbitrary. We adopt the same strategy used in the case $\delta = 0.5$, representing the cosine terms in terms of known Fourier expansions of absolute value functions.

The second summation term in the original expression corresponds to the standard Fourier series of $|\phi_0|$, as given in equation (3.16). Rearranging that expression, we obtain:

$$\sum_{i=1,3,5,\ldots}^{\infty} \frac{1}{i^2}\cos(i\phi_0) = \frac{\pi^2}{8} - \frac{\pi}{4}|\phi_0|$$

Analogously, the first summation term involving $\cos(i\phi_0 - i2\pi\delta)$ can be

interpreted as a phase-shifted triangular waveform, centered at $\phi_0 = 2\pi\delta$. It can be expressed as:

$$\sum_{i=1,3,5,\ldots}^{\infty} \frac{1}{i^2}\cos(i(\phi_0 - 2\pi\delta)) = \frac{\pi^2}{8} - \frac{\pi}{4}|\phi_0 - 2\pi\delta|$$

Substituting both expressions into the original formula and simplifying, we obtain:

$$\begin{aligned} Q_{\text{AND(L)}} &= \frac{\delta}{2} - \frac{1}{\pi^2}\left(\frac{\pi^2}{8} - \frac{\pi}{4}|\phi_0 - 2\pi\delta|\right) + \frac{1}{\pi^2}\left(\frac{\pi^2}{8} - \frac{\pi}{4}|\phi_0|\right) \\ &= \frac{\delta}{2} + \frac{|\phi_0 - 2\pi\delta|}{4\pi} - \frac{|\phi_0|}{4\pi} \end{aligned}$$

This expression can be rewritten in a more compact form:

$$Q_{\text{AND(L)}} = \frac{\delta}{2} + F_1 + F_2 \tag{3.17}$$

where

$$F_1 = \frac{|\phi_0 - 2\pi\delta|}{4\pi}, \quad \text{for } -\pi < (\phi_0 - 2\pi\delta) < \pi \tag{3.18}$$

$$F_2 = -\frac{|\phi_0|}{4\pi}, \quad \text{for } -\pi < \phi_0 < \pi \tag{3.19}$$

In the analysis of the signal $Q_{\text{AND(L)}}$, which is expressed as a combination of the functions F_1 and F_2, it is observed that the term $F_1 = \frac{|\phi_0 - 2\pi\delta|}{4\pi}$ forms a head-up triangular function whose vertex always occurs at $\phi_0 = 2\pi\delta$. In the case where $\delta = 0.5$, the vertex lies precisely at $\phi_0 = \pi$, which falls within the domain $(-\pi, \pi)$. However, when $\delta \neq 0.5$, the vertex shifts outside this interval, resulting in a function that is incomplete or discontinuous within the desired domain.

To address this issue, a domain-shifting technique is applied by shifting the function F_1 leftward by 2π, resulting in a modified expression $\frac{|\phi_0 - 2\pi\delta + 2\pi|}{4\pi}$. This transformation effectively wraps the part of the function that exceeds π back into the interval $(-\pi, \pi)$. Such shifting resembles a modulo operation on a periodic function, ensuring that $Q_{\text{AND(L)}}$ remains fully defined and continuous within the desired interval.

This approach leads to the construction of a piecewise representation of $Q_{\text{AND(L)}}$, as shown in equation (3.20), which combines the shifted and unshifted forms of F_1 along with F_2. The resulting expression ensures a smooth and continuous waveform across the full range of ϕ_0, and can be written as follows:

$$Q_{\text{AND(L)}} = \begin{cases} \dfrac{\delta}{2} - \dfrac{|\phi_0|}{4\pi} + \dfrac{|\phi_0 - 2\pi\delta + 2\pi|}{4\pi}, & \text{for } -\pi < \phi_0 < -\pi + 2\pi\delta \\ \dfrac{\delta}{2} - \dfrac{|\phi_0|}{4\pi} + \dfrac{|\phi_0 - 2\pi\delta|}{4\pi}, & \text{for } -\pi + 2\pi\delta < \phi_0 < \pi \end{cases} \tag{3.20}$$

Equation (3.20) defines the function $Q_{\text{AND(L)}}$ as a piecewise expression. Each interval uses a differently shifted form of F_1 to ensure continuity over the domain $\phi_0 \in (-\pi, \pi)$.

In the first interval, $-\pi < \phi_0 < -\pi + 2\pi\delta$, the term $\frac{|\phi_0 - 2\pi\delta + 2\pi|}{4\pi}$ is used. This representation results from shifting the original function F_1 leftward by 2π, effectively mapping the vertex at $\phi_0 = 2\pi\delta$ back into the valid domain. In the second interval, $-\pi + 2\pi\delta < \phi_0 < \pi$, the unshifted form $\frac{|\phi_0 - 2\pi\delta|}{4\pi}$ is applied, as it already lies within the desired interval.

To illustrate the piecewise structure of equation (3.20), a numerical example is considered for $\delta = 0.2$, and the results are shown in Figure 15. The figure consists of four subplots that individually present the key components contributing to the composite signal $Q_{\text{AND(L)}}$.

Figure 15(a) illustrates the constant value $\delta/2$, which serves as the base level in the construction of the output signal. In this example, where $\delta = 0.2$, the constant value equals 0.1 across the entire domain $\phi_0 \in (-\pi, \pi)$.

Figure 15(b) presents the piecewise-defined function F_1, which exhibits an inverted triangular shape with its vertex (minimum point) located at $\phi_0 = 2\pi\delta = 0.4\pi$. Although this vertex lies within the domain $(-\pi, \pi)$, the complete triangular waveform spans a width of 2π, and part of it extends beyond the domain boundary

on the right. To preserve continuity over the domain $(-\pi, \pi)$, the portion exceeding the right endpoint is shifted leftward by 2π, resulting in a wrapped segment that re-enters the domain from the left.

Consequently, the function F_1 is divided into two segments. The left portion (Range 1), defined over the interval $-\pi < \phi_0 < -\pi + 2\pi\delta = -0.6\pi$, employs the shifted form $|\phi_0 - 2\pi\delta + 2\pi|/(4\pi)$, as illustrated by the blue curve in Figure 15(b). The right portion (Range 2), defined over $-\pi + 2\pi\delta < \phi_0 < \pi$, uses the unshifted form $|\phi_0 - 2\pi\delta|/(4\pi)$, as illustrated by the green dashed curve in Figure 15(b). This decomposition allows the triangular waveform to remain continuous and correctly represented within the prescribed domain.

Figure 15(c) displays the triangular waveform $F_2 = -|\phi_0|/(4\pi)$, which symmetrically decreases from zero at $\phi_0 = 0$ towards the minimum value of -0.25 at both ends of the domain.

Finally, Figure 15(d) shows the resulting signal $Q_{\text{AND(L)}}$, obtained by summing the constant value $\delta/2$, the piecewise function F_1, and the symmetric triangular waveform F_2. The resulting curve is continuous and smooth throughout $(-\pi, \pi)$, clearly reflecting the piecewise structure defined in equation (3.20).

To further illustrate the behavior of equation (3.20), the case of $\delta = 0.8$ is considered. Figure 16(a)–(d) present each component of the piecewise function $Q_{\text{AND(L)}}$, constructed in the same manner as before.

Figure 16(a) shows the constant baseline $\delta/2 = 0.4$, valid throughout the interval $\phi_0 \in (-\pi, \pi)$.

Figure 16(b) displays the function F_1, which remains a inverted triangle with vertex at $\phi_0 = 2\pi\delta = 1.6\pi$. Since this vertex lies outside the domain on the right, it is shifted leftward by 2π, resulting in a new vertex at $\phi_0 = -0.4\pi$. The waveform is split into two parts: the left portion (Range 1), defined for $-\pi < \phi_0 < -\pi + 2\pi\delta = 0.6\pi$, uses the shifted form $|\phi_0 - 2\pi\delta + 2\pi|/(4\pi)$, shown in blue;

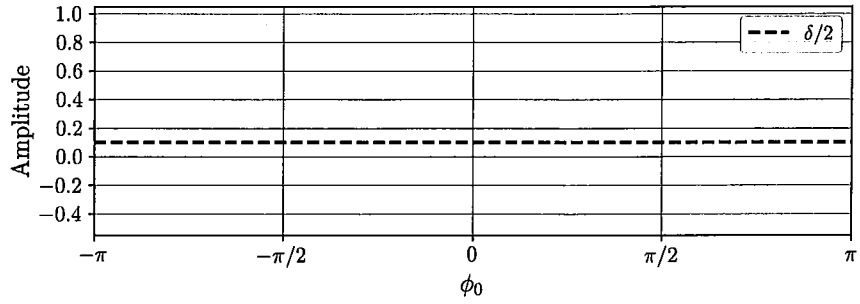

(a) Plot of $\delta/2$

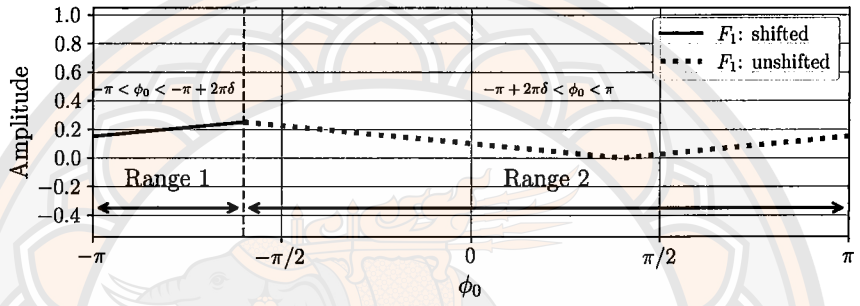

(b) Plot of F_1

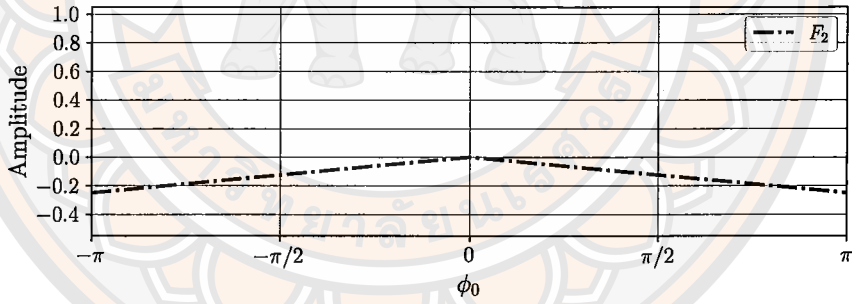

(c) Plot of F_2

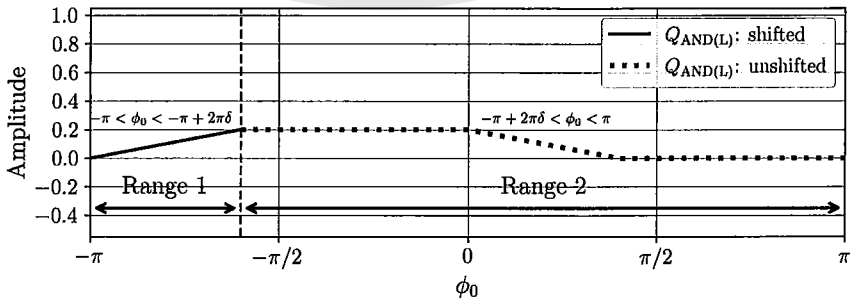

(d) Plot of $Q_{\mathrm{AND(L)}}$

Figure 15 Constructing $Q_{\mathrm{AND(L)}}$ for $\delta = 0.2$ using equation (3.20) with $\Delta f = 0$; (a) $\delta/2$, (b) F_1, (c) F_2, (d) result.

the right portion (Range 2), defined for $0.6\pi < \phi_0 < \pi$, uses the unshifted form $|\phi_0 - 2\pi\delta|/(4\pi)$, shown in green dashed.

Figure 16(c) presents the symmetrical triangular function $F_2 = -|\phi_0|/(4\pi)$, which decreases from 0 at $\phi_0 = 0$ to -0.25 at the boundaries.

Finally, Figure 16(d) shows the resulting waveform $Q_{\text{AND(L)}}$, computed by summing the three components: $\delta/2$, F_1, and F_2. The resulting waveform remains continuous and reflects the piecewise structure corresponding to the shifted vertex.

3.3.2 Signal Overlap Analysis for the AND Operator when $f_b \neq f_r$

To simplify the analysis in cases where the frequencies of the Base and Revealing layers differ, both signals are assumed to have an initial phase of zero. Thus, equation (3.13) can be rewritten as

$$\begin{aligned} Q_{\text{AND(L)}} = \frac{\delta}{2} &+ \frac{1}{\pi^2}\sum_{i=1}^{\infty}\frac{-1}{i^2}\cos(i(\Delta\omega)x - i2\pi\delta) \\ &+ \frac{1}{\pi^2}\sum_{i=1}^{\infty}\frac{-1}{i^2}\cos i(\Delta\omega)x \end{aligned} \tag{3.21}$$

where $i = m = n = 1, 3, 5, \ldots$

$$\Delta\omega = |\omega_r - \omega_b| = 2\pi|f_r - f_b| = 2\pi\Delta f = 2\pi\frac{|P_r - P_b|}{P_bP_r} = \frac{2\pi}{P_m} \tag{3.22}$$

Case 1: AND Operator with $f_b \neq f_r$ and $\delta = 0.5$

When considering the specific case where $\delta = 0.5$, equations (3.21) and (3.22) can be simplified as follows:

$$\begin{aligned} Q_{\text{AND(L)}} &= \frac{1}{4} + \frac{2}{\pi^2}\sum_{i=1}^{\infty}\frac{1}{i^2}\cos(i\Delta\omega x) \\ &= \frac{1}{4} + \frac{2}{\pi^2}\sum_{i=1}^{\infty}\frac{1}{i^2}\cos(i2\pi\Delta f x) \\ &= \frac{1}{4} + \frac{2}{\pi^2}\sum_{i=1}^{\infty}\frac{1}{i^2}\cos\left(i2\pi\frac{|P_r - P_b|}{P_rP_b}x\right) \end{aligned} \tag{3.23}$$

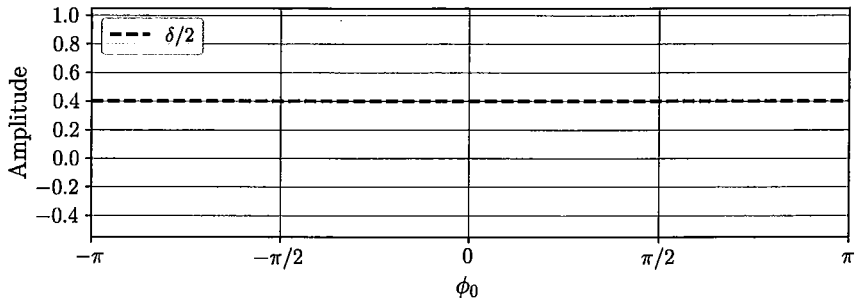

(a) Plot of $\delta/2$

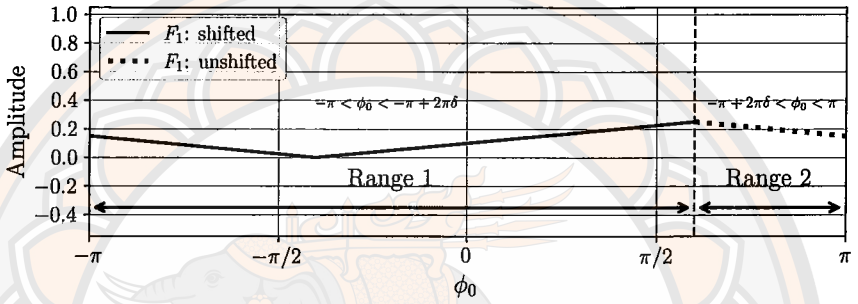

(b) Plot of F_1

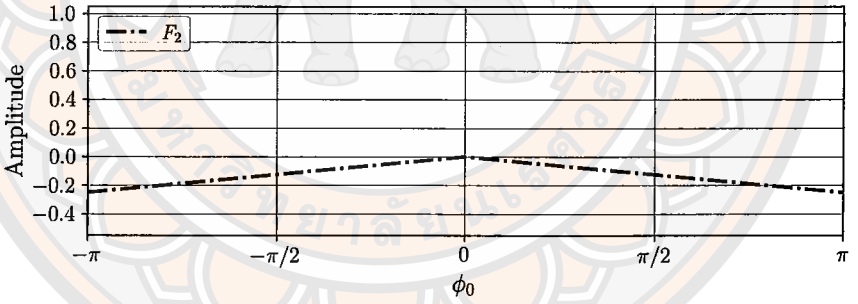

(c) Plot of F_2

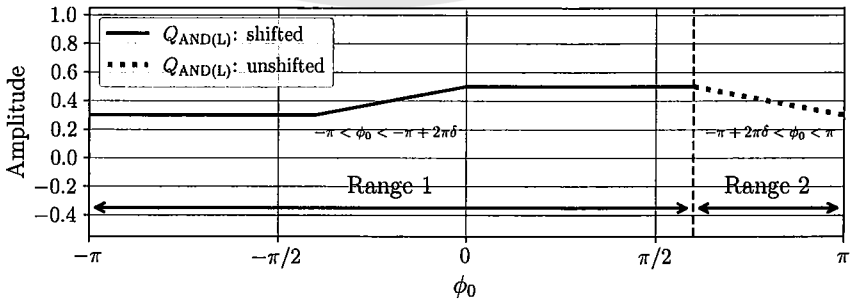

(d) Plot of $Q_{\mathrm{AND(L)}}$

Figure 16 Constructing $Q_{\mathrm{AND(L)}}$ for $\delta = 0.8$ using equation (3.20) with $\Delta f = 0$; (a) $\delta/2$, (b) F_1, (c) F_2, (d) result.

$$= \frac{1}{4} + \frac{2}{\pi^2}\sum_{i=1}^{\infty}\frac{1}{i^2}\cos\left(i\frac{2\pi}{P_m}x\right)$$
$$= \frac{1}{2} - \frac{|x|}{P_m} = \frac{1}{2} - \Delta f|x|; \quad (-P_m/2) < x < (P_m/2)$$

$$\text{where } \Delta f = \frac{1}{P_m} = \frac{|P_r - P_b|}{P_r P_b} \tag{3.24}$$

As illustrated by equation (3.23), the resulting waveform takes the form of a triangular function that varies with position x over the interval $(-P_m/2, P_m/2)$. This waveform exhibits a central value of $1/4$, a maximum magnitude of $1/2$, and a minimum of zero. Among all possible values of δ, this configuration yields the broadest magnitude range.

The equation reveals that the variation in the width of the translucent bands formed by the overlapping gratings manifests as a triangular profile. This profile oscillates at a frequency corresponding to the difference between the frequencies of the two input signals. When observing from $x = 0$ to $x = P_m$, by translating the function originally defined over $(-P_m/2, 0)$ into the domain $(P_m/2, P_m)$, the magnitude of $Q_{\text{AND(L)}}$ linearly decreases from $1/2$ to 0 at $x = P_m/2$, and then increases back to $1/2$ at $x = P_m$.

To better illustrate the translation of the signal, Figure 17(a) shows an inverted triangular waveform defined over the interval $(-P_m/2, P_m/2)$, which corresponds to the result of equation (3.23) in the case where $\delta = 0.5$. In this example, the parameters are set as $P_m = 1$ and $\Delta f = 1$, resulting in a signal that reaches its maximum value at $x = 0$ and decreases linearly toward zero at both ends of the interval.

By translating the segment $(-P_m/2, 0)$ to the interval $(P_m/2, P_m)$, the waveform is shifted to occupy the range $(0, P_m)$, as shown in Figure 17(b). The resulting waveform maintains the same shape, with its peak at $x = P_m/2$ and a maximum value of $Q_{\text{AND(L)}}$.

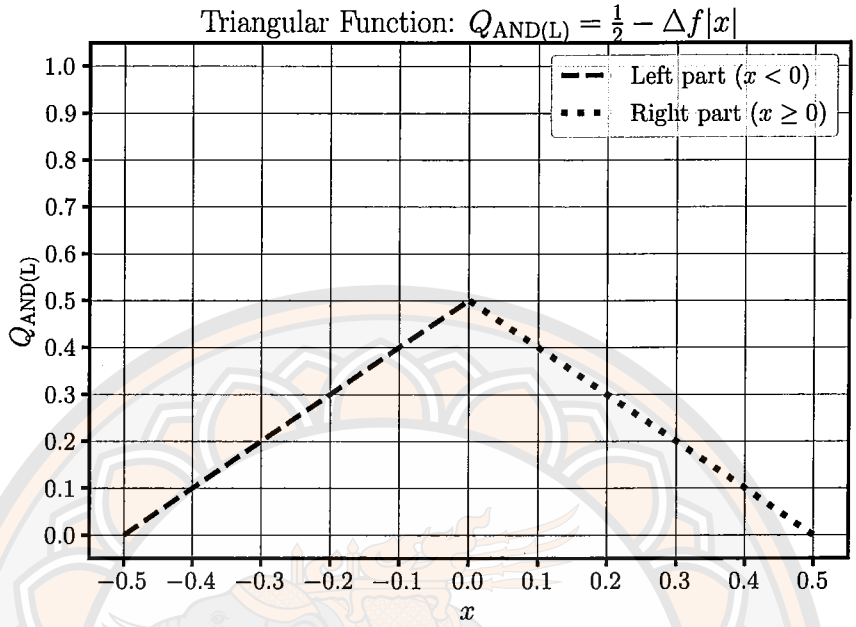

(a) Triangle wave, $x \in [-0.5, 0.5]$

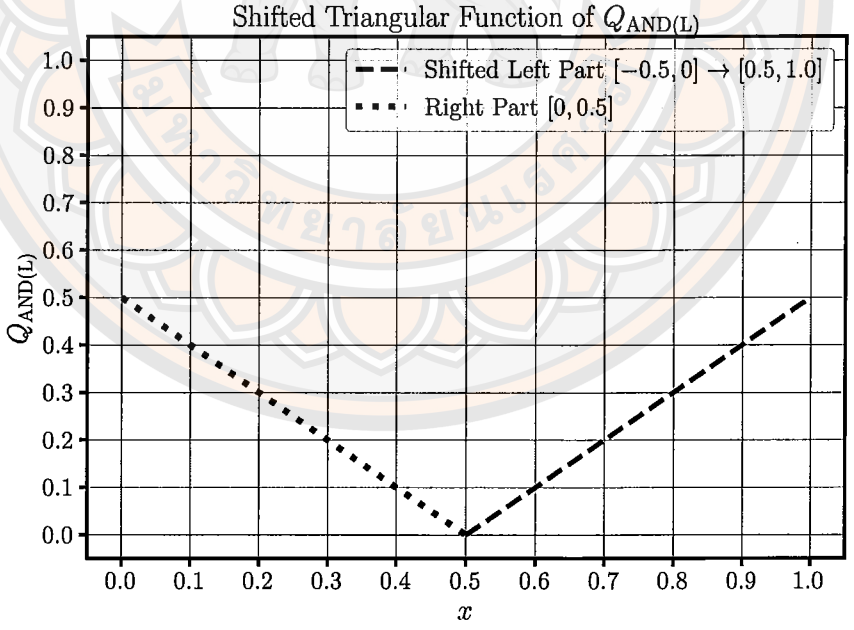

(b) Left-half shift: $[-0.5, 0] \rightarrow [0.5, 1.0]$

Figure 17 Comparison of the triangular function $Q_{\text{AND(L)}}$ before and after shifting the left segment.

This translation makes it easier to observe the variation in brightness as a function of position x, particularly when comparing the waveform to signals obtained from experiments or image processing results.

Case 2: AND Operator with $f_b \neq f_r$ and arbitary δ

For arbitrary values of δ, the same technique used in the case where $f_b = f_r$ can be applied. This involves comparing the series with the Fourier series expansion of the function $f(x) = |x|$ and utilizing signal-shifting properties. Accordingly, equation (3.21) can be rewritten as

$$Q_{\text{AND(L)}} = \begin{cases} \dfrac{\delta}{2} - \dfrac{|\Delta\omega x|}{4\pi} + \dfrac{|\Delta\omega x - 2\pi\delta + 2\pi|}{4\pi}; \\ \qquad (-\pi) < \Delta\omega x < (-\pi + 2\pi\delta) \\ \dfrac{\delta}{2} - \dfrac{|\Delta\omega x|}{4\pi} + \dfrac{|\Delta\omega x - 2\pi\delta|}{4\pi}; \\ \qquad (-\pi + 2\pi\delta) < \Delta\omega x < \pi \end{cases} \tag{3.25}$$

By expressing the function in terms of the spatial variable x, the equation becomes

$$Q_{\text{AND(L)}} = \begin{cases} \dfrac{\delta}{2} - \dfrac{|x/P_m|}{2} + \dfrac{|(x/P_m) - \delta + 1|}{2}; \\ \qquad (-P_m/2) < x < ((-P_m/2) + \delta P_m) \\ \dfrac{\delta}{2} - \dfrac{|x/P_m|}{2} + \dfrac{|(x/P_m) - \delta|}{2}; \\ \qquad ((-P_m/2) + \delta P_m) < x < (P_m/2) \end{cases} \tag{3.26}$$

Similar to the case described in equation (3.20), when $\delta = 0.5$, equation (3.26) produces a triangular waveform when plotted as a function of the spatial variable x. However, when $\delta \neq 0.5$, the waveform of $Q_{\text{AND(L)}}$ takes on the shape of a clipped triangle, or equivalently, a trapezoidal form. Despite this change in shape, the frequency remains equal to the difference between the frequencies of the two input signals.

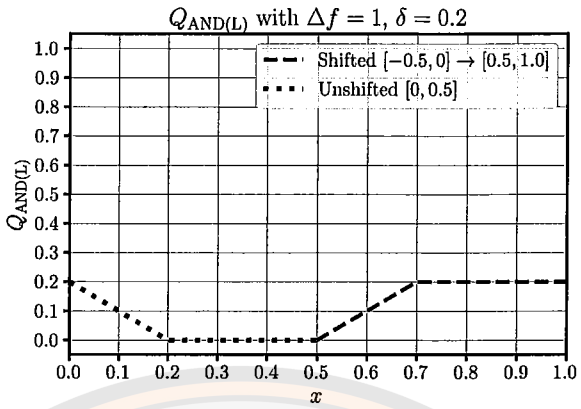

(a) $\delta = 0.2$

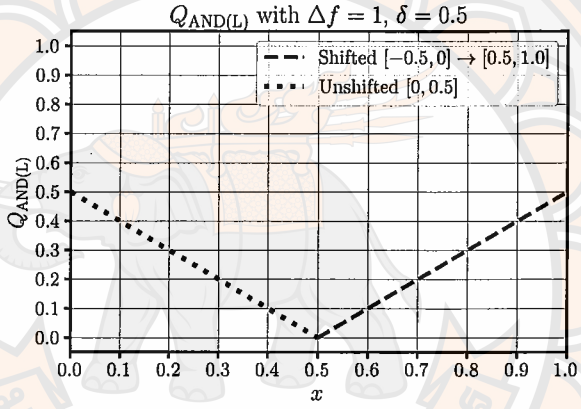

(b) $\delta = 0.5$

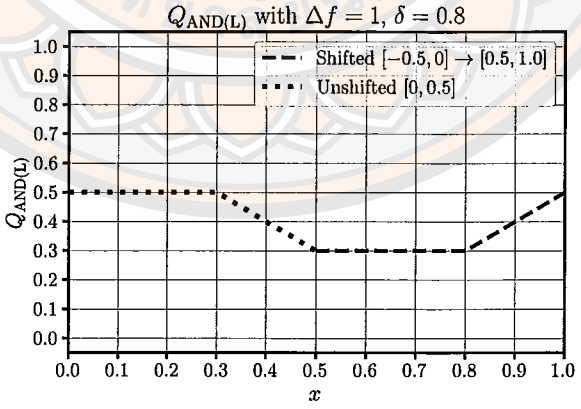

(c) $\delta = 0.8$

Figure 18 **Examples of $Q_{\text{AND(L)}}$ waveforms generated using equation (3.26) for different values of δ under $\Delta f = 1$. (a) $\delta = 0.2$, (b) $\delta = 0.5$, and (c) $\delta = 0.8$.**

For instance, when the frequency difference is set to $\Delta f = 1$, and the duty cycle is set to either $\delta = 0.2$ or $\delta = 0.8$, the resulting waveform derived from equation (3.26) clearly exhibits trapezoidal characteristics, as illustrated in Figures 18(a) and 18(c), respectively. These waveforms differ from the symmetric triangular case observed when $\delta = 0.5$ (Figure 18(b)), in that the width of the flat region varies according to the duty cycle, while the periodicity remains governed by the frequency difference.

This variation in the waveform directly influences the perceived width of the translucent region that appears due to the overlapping gratings. For values of $\delta > 0.5$, the maximum value of $Q_{\text{AND(L)}}$ is limited to 0.5, while the minimum value becomes $\delta - 0.5$. Conversely, when $\delta < 0.5$, the waveform reaches a maximum of δ and drops to a minimum of zero.

3.4 Overlap of Binary Gratings Based on Logical OR Operation

Similar to the AND operation, the overlap between the Base and Revealing layers can also be described using logical interpretation, as presented in Table 5. In this context, opaque regions are interpreted as a logic "1" and transparent regions as a logic "0" in the electrical sense. It is important to note that this logic behavior is the inverse of the AND operation.

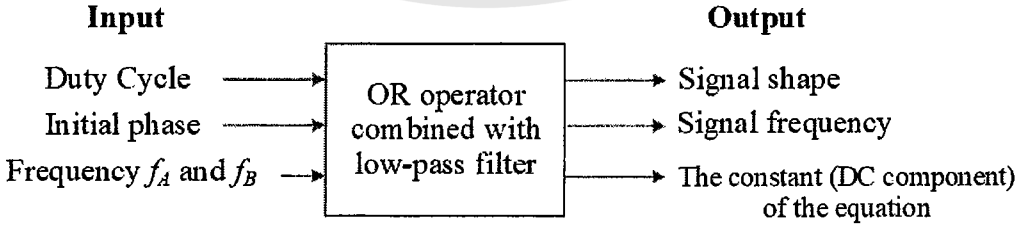

Figure 19 Block diagram of Moiré analysis using OR operator

The model shown in Figure 19 emulates the behavior of an OR gate. It receives fixed values for duty cycle, initial phase, and frequency as inputs. These

Table 5 Effects of overlapping between Base and Revealing for OR-gates

OR-gate Input		OR-gate Output
Base	Revealing	Result
transparent (0)	transparent (0)	transparent (0)
transparent (0)	opaque (1)	opaque (1)
opaque (1)	transparent (0)	opaque (1)
opaque (1)	opaque (1)	opaque (1)

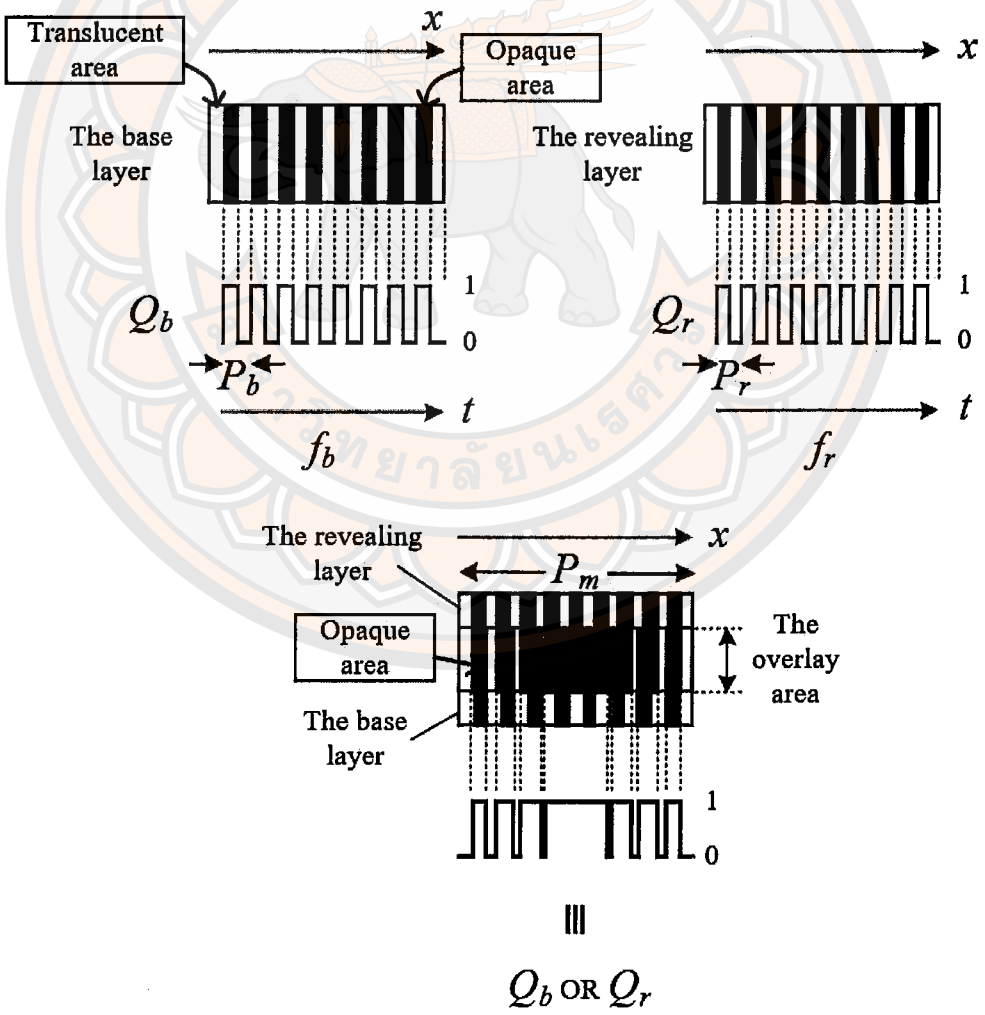

Figure 20 Analysis of Moiré pattern using the OR-operator

parameters are used to analyze the resulting Moiré pattern produced by the overlapping of the two gratings.

The analysis of the overlapping between the Base and Revealing layers for the OR operation is illustrated in Figure 20. As described in Section 3.3, the Revealing layer is a configurable component, allowing users to define its characteristics directly. Hence, it is possible to select an optimal value for δ, with $\delta = 0.5$ being the most suitable choice. This value allows the output of the logical operation to achieve its maximum possible width. In contrast, the value of δ for the Base layer depends on the intrinsic properties of the material being measured and generally cannot be adjusted.

Therefore, in the context of the OR operation, the overlapping analysis adopts the relationships defined in equations (3.5), (3.6), and (3.7) to model the resulting signal generated by the superposition of the two grating layers. The output signal is expressed as:

$$\begin{aligned} Q_{\text{OR}} &= Q_b + Q_r - Q_b Q_r \\ &= \left[\delta + \frac{1}{\pi}\sum_{n=1}^{\infty}\left(\frac{-1}{n}\sin n(\omega_b x - 2\pi\delta + \phi_0)\right)\right. \\ &\quad \left. + \frac{1}{\pi}\sum_{n=1}^{\infty}\left(\frac{1}{n}\sin n(\omega_b x + \phi_0)\right)\right] \\ &\quad + \left[\frac{1}{2} + \frac{2}{\pi}\sum_{m=1}^{\infty}\left(\frac{1}{m}\sin m\omega_r x\right)\right] \\ &\quad - \left[\delta + \frac{1}{\pi}\sum_{n=1}^{\infty}\left(\frac{-1}{n}\sin n(\omega_b x - 2\pi\delta + \phi_0)\right)\right. \\ &\quad \left. + \frac{1}{\pi}\sum_{n=1}^{\infty}\left(\frac{1}{n}\sin n(\omega_b x + \phi_0)\right)\right] \\ &\quad \times \left[\frac{1}{2} + \frac{2}{\pi}\sum_{m=1}^{\infty}\left(\frac{1}{m}\sin m\omega_r x\right)\right] \end{aligned} \tag{3.27}$$

We will get

$$
\begin{aligned}
Q_{\mathrm{OR}} &= A + B + C + D + E \\
&\quad -\frac{1}{\pi^2}\sum_{m=1}^{\infty}\sum_{n=1}^{\infty}\frac{-1}{nm}\left(\cos(n\omega_b x - n2\pi\delta + n\phi_0 - m\omega_r x)\right. \\
&\quad \left. -\cos(n\omega_b x - n2\pi\delta + n\phi_0 + m\omega_r x)\right) \\
&\quad -\frac{1}{\pi^2}\sum_{m=1}^{\infty}\sum_{n=1}^{\infty}\frac{-1}{nm}\left[\cos(n\omega_b x + n\phi_0 - m\omega_r x)\right. \\
&\quad \left. -\cos(n\omega_b x - n2\pi\delta + n\phi_0 + m\omega_r x)\right] \qquad (3.28)
\end{aligned}
$$

where

$$A = \frac{\delta}{2} \qquad (3.29)$$

$$B = \frac{1}{2\pi}\sum_{n=1}^{\infty}\frac{-1}{n}\sin(n\omega_b x - n2\pi\delta + n\phi_0) \qquad (3.30)$$

$$C = \frac{1}{2\pi}\sum_{n=1}^{\infty}\frac{1}{n}\sin(n\omega_b x + n\phi_0) \qquad (3.31)$$

$$D = \frac{1}{2} \qquad (3.32)$$

$$E = \frac{2-2\delta}{\pi}\sum_{m=1}^{\infty}\frac{1}{m}\sin(m\omega_r x) \qquad (3.33)$$

It can be observed that equation (3.28) comprises several terms similar to those in equation (3.13), which describes the case of the AND operator. Therefore, the analytical approach used here follows a similar methodology. Specifically, equation (3.28) can be decomposed into five distinct groups.

The first group consists of terms that are independent of the spatial variable x, namely terms A and D. The second group includes sine functions oscillating at the frequency of the Base layer (terms B and C). The third group contains sine functions at the frequency of the Revealing layer (term E). The fourth group is composed of cosine functions whose frequencies are equal to the sum of the frequencies of the Base and Revealing layers. Finally, the fifth group consists of cosine functions with frequencies corresponding to the difference between the two layers.

In general, the second through fourth groups are considered high-frequency components when compared with the fifth group. Although all the terms in equation (3.28) contribute to the overall appearance of the overlapping pattern, it is assumed that the low-frequency components play the most significant role in the formation of Moiré patterns. This assumption is consistent with the analysis previously discussed in the case of the AND operator.

Within the fifth group, only the terms that satisfy the condition $m = n$ are considered dominant. By eliminating the high-frequency components and retaining only the low-frequency terms, the resulting signal, denoted as $Q_{\mathrm{OR(L)}}$, is defined as the low-pass filtered version of Q_{OR}. This filtered signal will be analyzed further in the following sections, covering two cases: when the two input signals have identical frequencies and when they have different frequencies.

3.4.1 Signal Overlap Analysis for the OR Operator when $f_b = f_r$

To analyze the signal $Q_{\mathrm{OR(L)}}$ after high-frequency components have been removed, we consider the case where $f_b = f_r$. By substituting $m = n = i$ into equation (3.28), we obtain:

$$Q_{\mathrm{OR(L)}} = \frac{1+\delta}{2} - \frac{1}{\pi^2}\sum_{i=1}^{\infty}\frac{-1}{i^2}\cos(i\phi_0 - i2\pi\delta) - \frac{1}{\pi^2}\sum_{i=1}^{\infty}\frac{1}{i^2}\cos i\phi_0 \tag{3.34}$$

where $i = m = n = 1, 3, 5, \ldots$.

Case 1: OR Operator with $f_b = f_r$ and $\delta = 0.5$

By setting $\delta = 0.5$, equation (3.34) simplifies to:

$$Q_{\mathrm{OR(L)}} = \frac{3}{4} - \frac{2}{\pi^2}\sum_{i=1}^{\infty}\frac{1}{i^2}\cos(i\phi_0) \tag{3.35a}$$

$$= \frac{1}{2} + \frac{|\phi_0|}{2\pi}, \quad \text{for } -\pi < \phi_0 < \pi \tag{3.35b}$$

Equations (3.35a) and (3.35b) is structurally similar to equations (3.15a) and (3.15b) for the AND operator, but with an opposite sign in the second term, as illustrated in Figure 21. As a result, the waveform of $Q_{\mathrm{OR(L)}}$ appears as an

inverted triangle compared to that of the AND case. The function ranges from 1/2 to 1, with an average of 3/4. This confirms that $\delta = 0.5$ provides the widest amplitude variation for both logical operations.

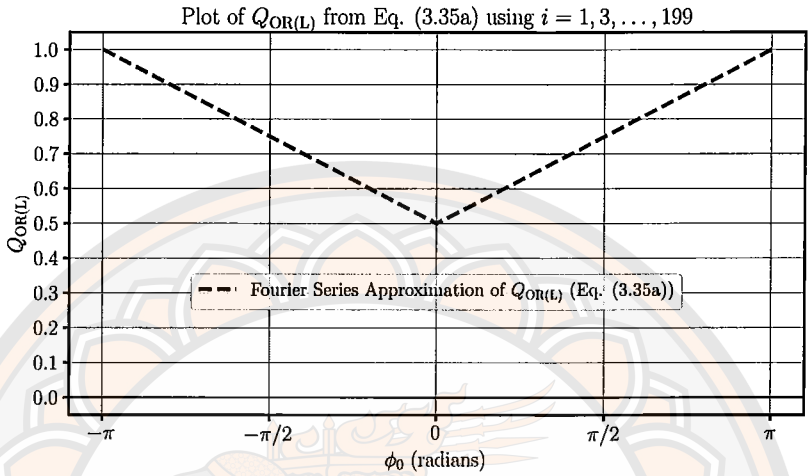

(a) Plot of $Q_{OR(L)}$ using the Fourier series in equation (3.35a).

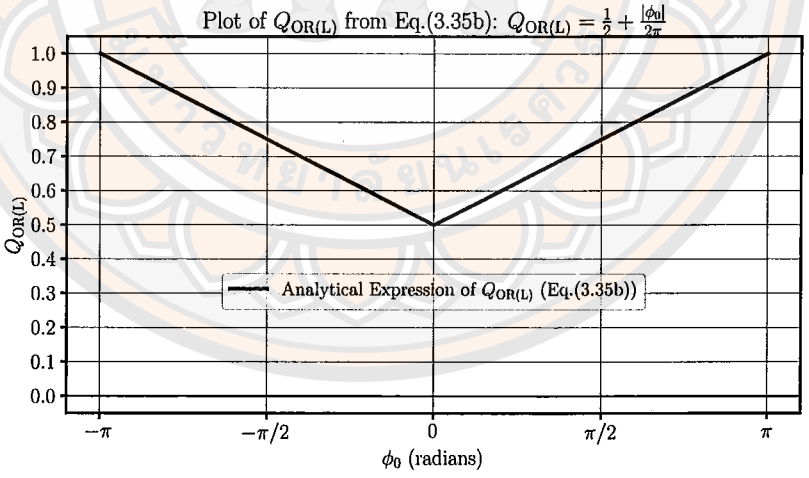

(b) Plot of $Q_{OR(L)}$ using the analytical expression in equation (3.35b).

Figure 21 **Comparison of $Q_{OR(L)}$ obtained from (a) the Fourier series approximation in equation (3.35a), and (b) the analytical expression in equation (3.35b).**

Figure 21(a) displays the waveform derived from the Fourier series representation in equation (3.35a), constructed by summing the first 100 odd harmonics of the cosine series. Figure 21(b), in contrast, shows the corresponding waveform obtained directly from the analytical expression $Q_{\mathrm{OR(L)}} = \frac{1}{2} + \frac{|\phi_0|}{2\pi}$, which is a linearly increasing function of the absolute phase. The close match between the two curves confirms the validity of the derivation and demonstrates that the analytical form accurately captures the behavior of the Fourier-based representation.

Case 2: OR Operator with $f_b = f_r$ and arbitrary δ

For arbitrary values of δ, equation (3.34) leads to a more complex expression, where the cosine terms cannot be combined directly. A piecewise form of the solution can be derived similarly to the AND case, using known Fourier expansions of absolute value functions. The resulting expression is given as:

$$Q_{\mathrm{OR(L)}} = \begin{cases} \dfrac{1+\delta}{2} + \dfrac{|\phi_0|}{4\pi} - \dfrac{|\phi_0 - 2\pi\delta + 2\pi|}{4\pi}, \text{for } -\pi < \phi_0 < -\pi + 2\pi\delta \\ \dfrac{1+\delta}{2} + \dfrac{|\phi_0|}{4\pi} - \dfrac{|\phi_0 - 2\pi\delta|}{4\pi}, \text{for } -\pi + 2\pi\delta < \phi_0 < \pi \end{cases} \tag{3.36}$$

Similar to the case of the AND operator, equation (3.36) for the OR operator is also divided into two regions: Range 1 ($-\pi < \phi_0 < -\pi + 2\pi\delta$) and Range 2 ($-\pi + 2\pi\delta < \phi_0 < \pi$). In this case, the signal $Q_{\mathrm{OR(L)}}$ is constructed from the combination of three main components: a constant term $\frac{1+\delta}{2}$, an absolute-value term $\frac{|\phi_0|}{4\pi}$, and a final term that differs depending on the region. Specifically, for Range 1, the expression includes the shifted component $-\frac{|\phi_0 - 2\pi\delta + 2\pi|}{4\pi}$, while for Range 2, the unshifted component $-\frac{|\phi_0 - 2\pi\delta|}{4\pi}$ is used. The summation of these three parts yields the overall waveform of $Q_{\mathrm{OR(L)}}$.

Figure 22(a) illustrates the resulting waveform of $Q_{\mathrm{OR(L)}}$ when $\delta = 0.2$. It can be observed that Range 1, which includes the shifted component, is shorter than Range 2, which contains the unshifted component. In contrast, Figure 22(c) shows

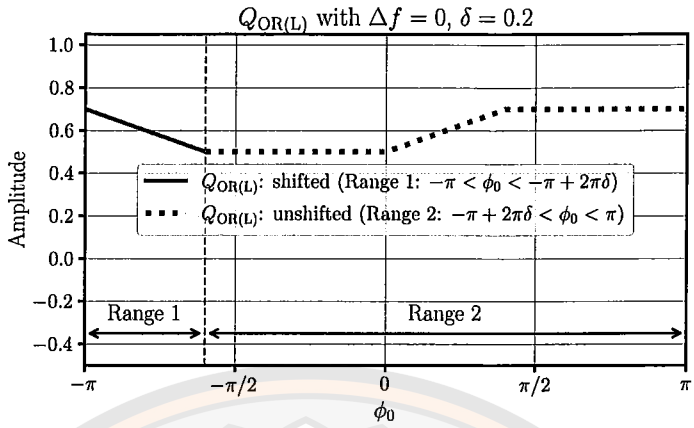

(a) $Q_{OR(L)}$ for $\delta = 0.2$

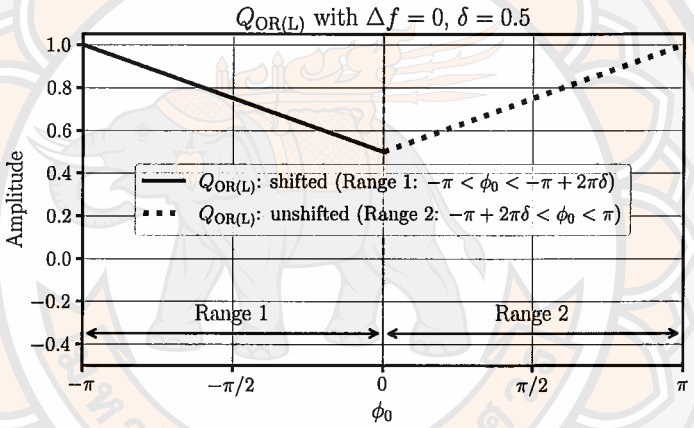

(b) $Q_{OR(L)}$ for $\delta = 0.5$

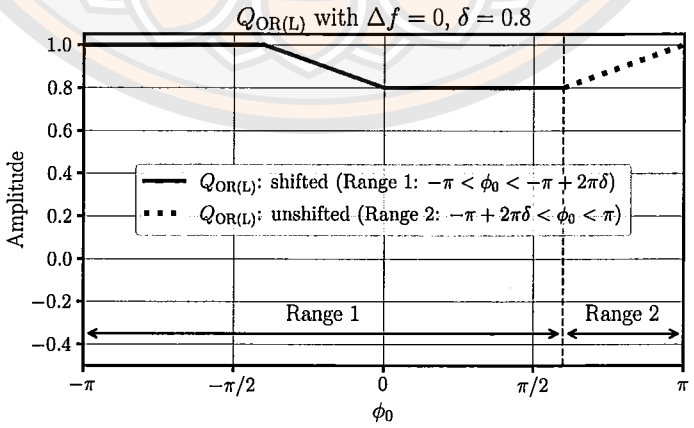

(c) $Q_{OR(L)}$ for $\delta = 0.8$

Figure 22 Waveform of $Q_{OR(L)}$ as derived from equation (3.36) for different values of δ, under the condition $\Delta f = 0$.

the case where $\delta = 0.8$, resulting in a longer shifted region and a shorter unshifted region. As a special case, Figure 22(b) presents the scenario when $\delta = 0.5$, where the shifted and unshifted parts exhibit perfect symmetry across the domain.

According to equation (3.36), the maximum, minimum, and average values of $Q_{\mathrm{OR(L)}}$ vary depending on the value of δ. When $\delta = 0.5$, the signal exhibits the widest range, with a minimum value of 0.5, a maximum value of 1, and an average of 0.75. For the case $\delta < 0.5$, the maximum value becomes $\delta + 0.5$, the minimum remains fixed at 0.5, and the average value is $(1 + \delta)/2$, which lies between 0.5 and 0.75. Conversely, when $\delta > 0.5$, the maximum value is limited to 1, while the minimum value increases to δ, and the average value again equals $(1 + \delta)/2$, ranging between 0.75 and 1.

3.4.2 Signal Overlap Analysis for the Case of $f_b \neq f_r$

In the analysis of the case where $f_b \neq f_r$, the initial phase is set to zero, similar to the case of the AND operator. Therefore, equation (3.28) yields the low-pass filtered signal $Q_{\mathrm{OR(L)}}$ as follows:

$$Q_{\mathrm{OR(L)}} = \frac{1+\delta}{2} - \frac{1}{\pi^2}\sum_{i=1}^{\infty}\frac{-1}{i^2}\cos(i(\Delta\omega)x - i2\pi\delta) - \frac{1}{\pi^2}\sum_{i=1}^{\infty}\frac{1}{i^2}\cos i(\Delta\omega)x \quad (3.37)$$

where $i = m = n = 1, 3, 5, ...$

$$\Delta\omega = |\omega_r - \omega_b| = 2\pi|f_r - f_b| = 2\pi\Delta f = 2\pi\frac{|P_r - P_b|}{P_b P_r} = \frac{2\pi}{P_m} \quad (3.38)$$

When considering the specific case of $\delta = 0.5$, equations (3.27) and (3.28) can be related as:

$$\begin{aligned} Q_{\mathrm{OR(L)}} &= \frac{3}{4} - \frac{2}{\pi^2}\sum_{i=1}^{\infty}\frac{1}{i^2}\cos i(\Delta\omega)x \\ &= \frac{3}{4} - \frac{2}{\pi^2}\sum_{i=1}^{\infty}\frac{1}{i^2}\cos i2\pi(\Delta f)x \\ &= \frac{3}{4} - \frac{2}{\pi^2}\sum_{i=1}^{\infty}\frac{1}{i^2}\cos i2\pi\frac{|P_r - P_b|}{P_r P_b}x \end{aligned} \quad (3.39)$$

$$
\begin{aligned}
&= \frac{3}{4} - \frac{2}{\pi^2}\sum_{i=1}^{\infty}\frac{1}{i^2}\cos i\frac{2\pi}{P_m}x \\
&= \frac{1}{2} + \frac{|x|}{P_m} = \frac{1}{2} + \Delta f|x| \; ; \\
&\qquad (-P_m/2) < \phi_0 < (P_m/2) \\
\text{where } \Delta f &= \frac{1}{P_m} = \frac{|P_r - P_b|}{P_r P_b}
\end{aligned} \tag{3.40}
$$

The analysis of equation (3.39) follows the same approach as in the AND case. It reveals that the resulting signal exhibits a triangular waveform that varies with position x within the interval $(-P_m/2, P_m/2)$. However, unlike the AND case, the average value of $Q_{\mathrm{OR(L)}}$ is 3/4, with a maximum value of 1 and a minimum value of 1/2. The magnitude of the signal reaches its highest value when $\delta = 0.5$.

Equation (3.39) demonstrates that the variation in the visible opaque region forms a triangular shape similar to the AND case. The difference lies in the opposite phase and different average values. When observing from $x = 0$ to $x = P_m$, the section from $x = -P_m/2$ to $x = 0$ must be shifted to replace the interval $(P_m/2, P_m)$. As a result, the signal $Q_{\mathrm{OR(L)}}$ starts at 1/2 at $x = 0$, increases to 1 at $x = P_m/2$, then decreases back to 1/2 at $x = P_m$.

For any value of δ, the technique of comparison with the function $f(x) = |x|$ and shifting the signal into the range $(-\pi, \pi)$ is applied, as done in the previous section. Therefore, equation (3.37) can be rewritten as:

$$
Q_{\mathrm{OR(L)}} = \begin{cases}
\dfrac{1+\delta}{2} + \dfrac{|\Delta\omega x|}{4\pi} - \dfrac{|\Delta\omega x - 2\pi\delta + 2\pi|}{4\pi}; \\
\qquad -\pi < \Delta\omega x < -\pi + 2\pi\delta \\
\dfrac{1+\delta}{2} + \dfrac{|\Delta\omega x|}{4\pi} - \dfrac{|\Delta\omega x - 2\pi\delta|}{4\pi}; \\
\qquad -\pi + 2\pi\delta < \Delta\omega x < \pi
\end{cases} \tag{3.41}
$$

When rewritten in terms of position x, the equation becomes:

$$Q_{\mathrm{OR(L)}} = \begin{cases} \dfrac{1+\delta}{2} + \dfrac{|x/P_m|}{2} - \dfrac{|(x/P_m) - \delta + 1|}{2}; \\ \qquad -P_m/2 < x < (-P_m/2 + \delta P_m) \\ \dfrac{1+\delta}{2} + \dfrac{|x/P_m|}{2} - \dfrac{|(x/P_m) - \delta|}{2}; \\ \qquad (-P_m/2 + \delta P_m) < x < P_m/2 \end{cases} \tag{3.42}$$

The analysis of equation (3.42) indicates that when $\delta = 0.5$, the signal $Q_{\mathrm{OR(L)}}$ takes the shape of a triangle that varies with position x. However, for $\delta \neq 0.5$, the waveform becomes a clipped triangle. Still, the frequency remains equal to the difference in frequencies between the two input signals. This reflects the change in the width of the visible opaque lines.

When $\delta > 0.5$, the signal $Q_{\mathrm{OR(L)}}$ reaches a maximum value of 1 and a minimum value of δ. If $\delta < 0.5$, the signal attains a maximum value of $0.5 + \delta$ and a minimum value of 0.5.

These characteristics are clearly illustrated in Figure 23, where the waveforms for $\delta = 0.2$, 0.5, and 0.8 are plotted. Figure 23b shows the symmetric triangular shape for $\delta = 0.5$, while Figures 23a and 23c demonstrate the asymmetric clipped shapes resulting from $\delta < 0.5$ and $\delta > 0.5$, respectively.

3.5 Computer Simulation of Overlap Signal Results

3.5.1 Parameter Setup for Logical Signal Verification Using Low-Pass Filtering

This section presents the parameter setup used for verifying the output behavior of logical operators combined with low-pass filtering. The verification is performed through numerical simulations of the derived equations, covering both equal-frequency and unequal-frequency cases. A Python program was developed to simulate the logical signal models described in Sections 3.3 and 3.4.

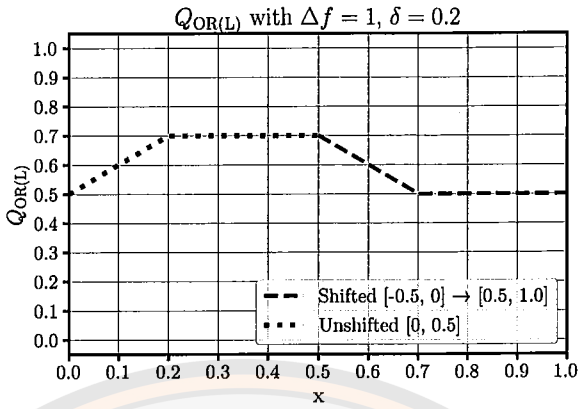

(a) $\delta = 0.2$

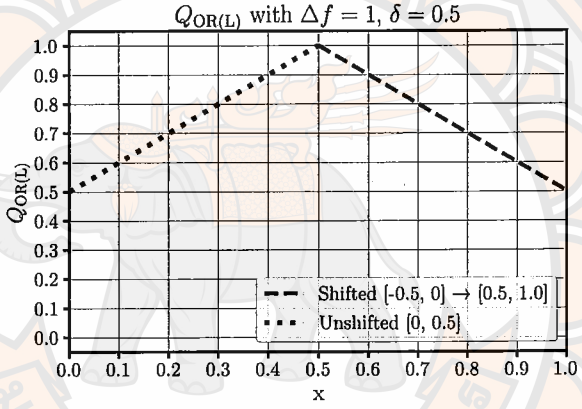

(b) $\delta = 0.5$

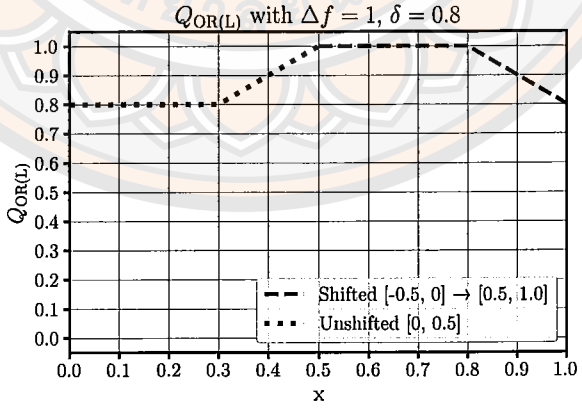

(c) $\delta = 0.8$

Figure 23 **Examples of $Q_{OR(L)}$ waveforms generated using equation (3.42) for different values of δ under $\Delta f = 1$. (a) $\delta = 0.2$, (b) $\delta = 0.5$, and (c) $\delta = 0.8$.**

Case 1: Equal frequency ($f_b = f_r$)

In this case, both the Base and Revealing layers are assigned the same frequency, set to 1 unit. The duty cycle of the Revealing layer is fixed at 0.5, while the duty cycle of the Base layer is varied across a range from 0.1 to 0.9. The overlapping phase position, represented by ϕ_0, is defined within the interval $(-2\pi, 2\pi)$. A total of 400 points are used to discretize one complete cycle of the signal.

Using this setup, the output signals of the AND and OR operations, denoted as Q_{AND} and Q_{OR}, are computed point by point and normalized by dividing by 400. This process yields the low-frequency components of the logic signals, referred to as $Q_{\text{AND(L)}}(\text{G})$ and $Q_{\text{OR(L)}}(\text{G})$, respectively. The results are then plotted to obtain the output waveforms generated from the AND and OR operations. These waveforms are compared with those obtained from the analytical expressions given in equation (3.20) for the AND case and equation (3.36) for the OR case. This comparison allows for a clear evaluation of the consistency and characteristic behavior of the low-pass filtered signals produced by the two logical operators.

Case 2: Unequal frequency ($f_b \neq f_r$)

In the unequal frequency scenario, the frequency of the Revealing layer is fixed at 100 lines per unit length L, with a duty cycle of 0.5. The frequency of the Base layer is varied across 101, 102, and 103 lines per unit length L. In addition, its duty cycle is set to 0.2, 0.5, and 0.8 for different test cases. To ensure coverage of at least 100 signal cycles, each simulation uses 10,000 points for signal generation.

After generating the overlapped signals between the Base and Revealing layers, a moving average low-pass filter is applied. This filter computes the average of values within a window of ± 200 points centered at each target location. The filtered outputs, $Q_{\text{AND(L)}}(\text{G})$ and $Q_{\text{OR(L)}}(\text{G})$, are then used to analyze the low-frequency response of each logical operator under frequency mismatch conditions.

To further evaluate the theoretical consistency of the results, the simulation outputs are compared with analytical plots derived from equation (3.26) for the AND operation and equation (3.42) for the OR operation. These comparisons provide insights into the alignment between the behavior of the logic-based simulations and their corresponding mathematical models under unequal-frequency scenarios.

3.5.2 Computer Simulation Results of the AND Operator

This section presents the simulation results of the AND operator under two distinct configurations: (1) when the frequencies of the Base and Revealing layers are equal ($f_b = f_r$), and (2) when they are unequal ($f_b \neq f_r$). For each configuration, results from logic-based simulations are compared with those obtained from analytical expressions.

Case I: AND Operator with equal frequency ($f_b = f_r$)

Figure 24 illustrates the comparison between two methods used to obtain the signal $Q_{\mathrm{AND(L)}}$: one derived analytically from equation (3.20), and the other obtained from logic-based simulation using $Q_{\mathrm{AND}} = Q_b$ AND Q_r, followed by low-pass filtering to yield $Q_{\mathrm{AND(L)}}(\mathrm{G})$.

To analyze the effect of the duty cycle δ, the results are categorized into the following three conditions and are summarized in Table 6.

- **Condition A:** $\delta = 0.5$

  The signals exhibit a symmetric triangular waveform with the widest amplitude range. Both methods yield a maximum value of 0.5 and a minimum value of 0, resulting in an average of 0.25.

- **Condition B:** $\delta < 0.5$

  The waveform appears clipped at the top, reducing its range. The maximum value is δ, the minimum remains at 0, and the average value falls below 0.25. As δ increases toward 0.5, the amplitude range expands.

- **Condition C:** $\delta > 0.5$

  Here, the waveform is clipped at the bottom. The maximum remains at 0.5, while the minimum increases to $\delta - 0.5$, and the average value becomes greater than 0.25.

Table 6 Summary of $Q_{\text{AND(L)}}$ signal characteristics when $f_b = f_r$ and $f_b \neq f_r$

Condition	δ Value	Waveform Shape	Max	Min	Average
A	$\delta = 0.5$	Full triangular	0.5	0	0.25
B	$\delta < 0.5$	Clipped at top	δ	0	< 0.25
C	$\delta > 0.5$	Clipped at bottom	0.5	$\delta - 0.5$	> 0.25

As δ deviates from 0.5, the amplitude range of $Q_{\text{AND(L)}}$ decreases. Under $f_b = f_r$, the resulting image brightness remains relatively stable due to the fixed relative phase ϕ_0. However, if the revealing layer is gradually shifted, temporal variations in brightness become apparent, as shown in Figure 24.

Case II: AND Operator with unequal frequency ($f_b \neq f_r$)

A similar analysis is performed when the frequencies are unequal ($f_b \neq f_r$). Figure 25 compares the analytical waveform based on equation (3.26) and the logic-based simulation result $Q_{\text{AND(L)}}(\text{G})$.

Interestingly, the classification of waveform behavior using δ into Conditions A–C remains applicable. The resulting waveform frequency equals the frequency difference between the input signals, validating the analytical derivation.

However, the analytical waveform $Q_{\text{AND(L)}}$ (Eq. (26)) appears smoother than its simulated counterpart due to ideal low-pass filtering. In contrast, the simulation-derived signal still exhibits ripples, which are remnants of higher-order frequency components not fully eliminated in practice.

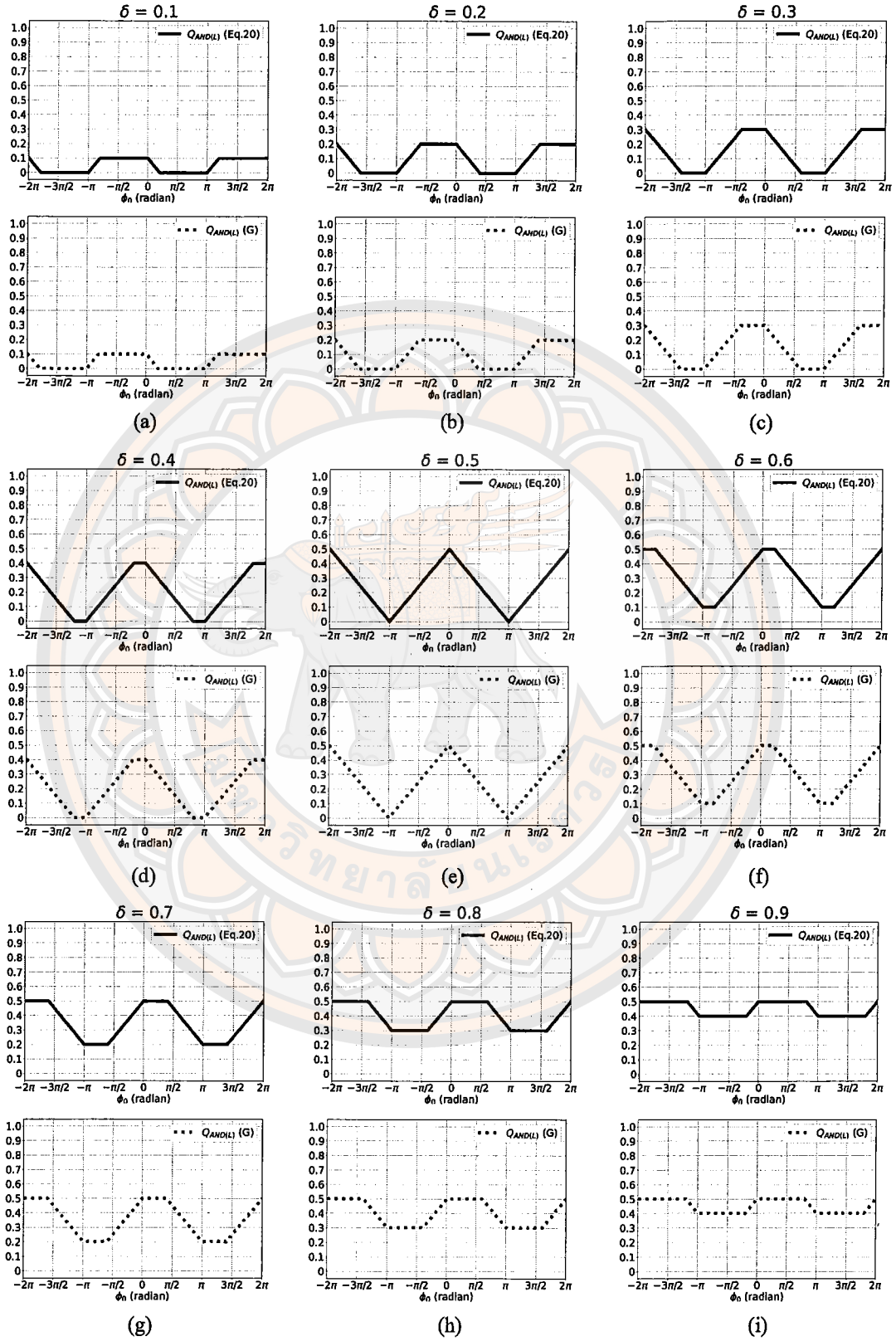

Figure 24 Simulation results of the AND operator for $f_b = f_r$, showing $Q_{\mathbf{AND(L)}}$ waveforms for $\delta = 0.1$ to 0.9.

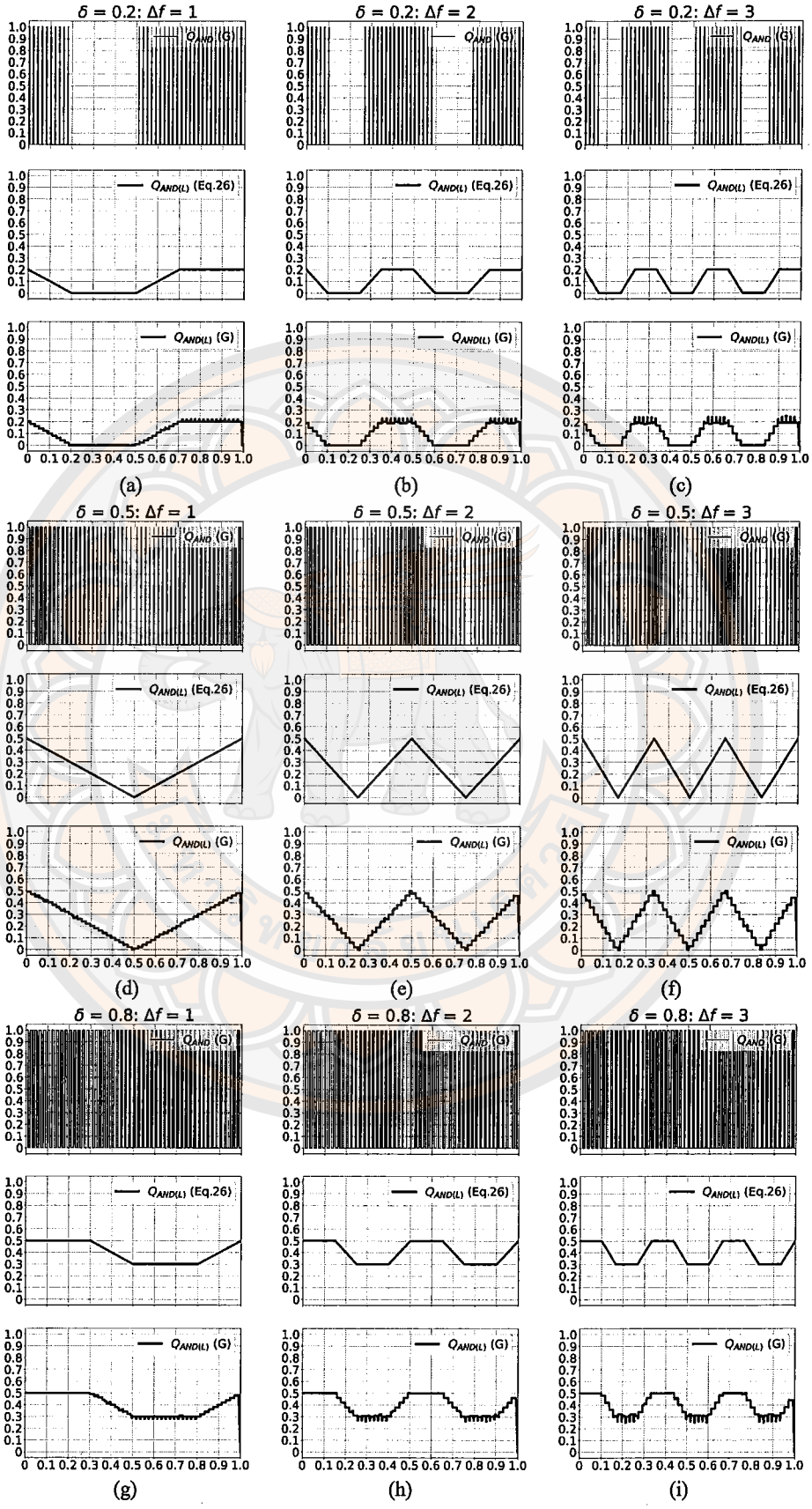

Figure 25 Simulation results of the AND operator for $f_b \neq f_r$, with $\delta = \{0.2, 0.5, 0.8\}$ and $\Delta f = \{1, 2, 3\}$.

3.5.3 Computer Simulation Results of the OR Operator

This section presents the simulation results of the OR operator under two different conditions: when the frequencies of the Base and Revealing layers are equal ($f_b = f_r$), and when they are unequal ($f_b \neq f_r$). In both cases, the results from logic-based simulations are compared with the analytical solutions to assess the consistency and behavior of the resulting signals.

Case I: OR Operator with equal frequency ($f_b = f_r$)

Figure 26 illustrates a comparison between two methods for generating the $Q_{\mathrm{OR(L)}}$ (Eq. (36)) signal. The first method is based on the analytical expression derived in equation (3.36), while the second method involves a logical OR operation between Q_b and Q_r ($Q_{\mathrm{OR}} = Q_b$ OR Q_r) followed by low-pass filtering, resulting in the signal $Q_{\mathrm{OR(L)}}(\mathrm{G})$.

To better understand the effect of the duty cycle δ on the output signal, the results are categorized into three conditions, as summarized in Table 7:

- **Condition A:** $\delta = 0.5$

  The output waveform is triangular with the maximum range. The signal oscillates between 1 and 0.5, resulting in a median value of 0.75.

- **Condition B:** $\delta < 0.5$

  The waveform becomes clipped at the top and the bottom. The maximum value is $0.5 + \delta$, the minimum remains 0.5, and the median value is less than 0.75.

- **Condition C:** $\delta > 0.5$

  The waveform is also a triangle clipped at both the top and bottom. The maximum value remains at 1.0, while the minimum increases to δ. As a result, the median value becomes greater than 0.75.

It is evident that the waveforms produced by both methods are identical,

Table 7 **Summary of $Q_{\mathrm{OR(L)}}$ signal characteristics when $f_b = f_r$ and $f_b \neq f_r$**

Condition	δ Value	Waveform Shape	Max	Min	Average
A	$\delta = 0.5$	Triangular	1.0	0.5	0.75
B	$\delta < 0.5$	Clipped triangle	$0.5 + \delta$	0.5	< 0.75
C	$\delta > 0.5$	Clipped triangle	1.0	δ	> 0.75

verifying that equation (3.36) accurately represents the behavior of the OR operator. Notably, when $\delta = 0.5$, the resulting waveform is triangular and exhibits the highest amplitude compared to other values of δ.

Case II: OR Operator with unequal frequency ($f_b \neq f_r$)

Figure 27 illustrates the results of analyzing the characteristics of the OR operator in the case where $f_b \neq f_r$. Two methods are compared: the analytical expression based on equation (3.42), denoted as $Q_{\mathrm{OR(L)}}$ (Eq. (42)), and the signal $Q_{\mathrm{OR(L)}}$ (G), which is obtained by applying the logical OR operation to Q_b and Q_r ($Q_{\mathrm{OR}} = Q_b$ OR Q_r), followed by low-pass filtering via averaging.

Both signals exhibit consistent behavior. The frequency of the resulting waveform in each method corresponds exactly to the frequency difference $\Delta f = |f_r - f_b|$. However, $Q_{\mathrm{OR(L)}}$ (G) still shows slight ripple due to the non-ideal nature of the averaging method, while $Q_{\mathrm{OR(L)}}$ (Eq. (42)) represents the ideal low-pass filtered signal and therefore appears smoother.

The magnitudes and shapes of the resulting waveforms can be categorized into the same three conditions based on the value of δ, as summarized in Table 7. The signal characteristics in each δ condition for the case $f_b \neq f_r$ remain consistent with those observed in the $f_b = f_r$ case.

This observed consistency in waveform shape across both frequency con-

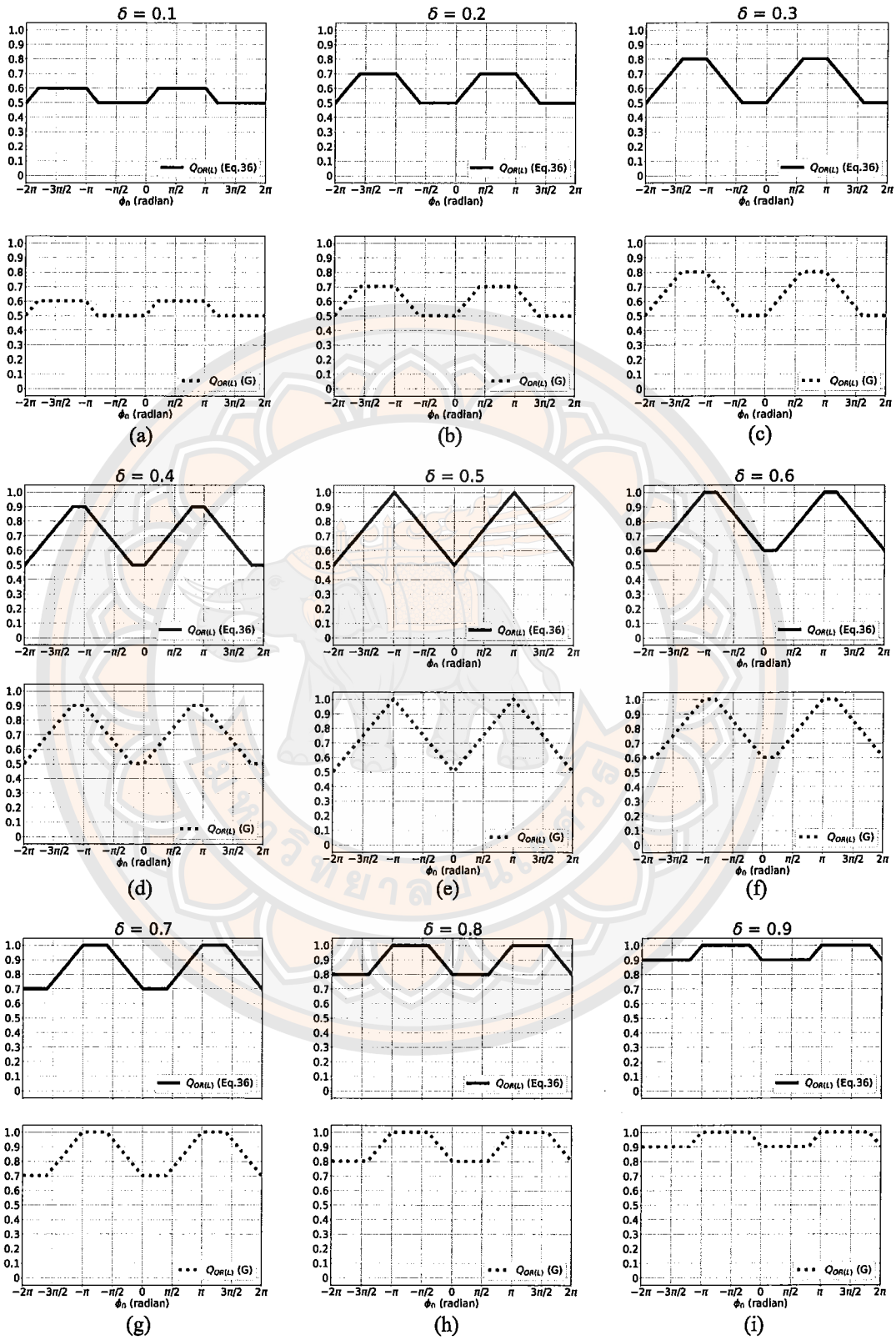

Figure 26 Simulation results of the OR operator for $f_b = f_r$; (a)–(i): $\delta = 0.1$–0.9.

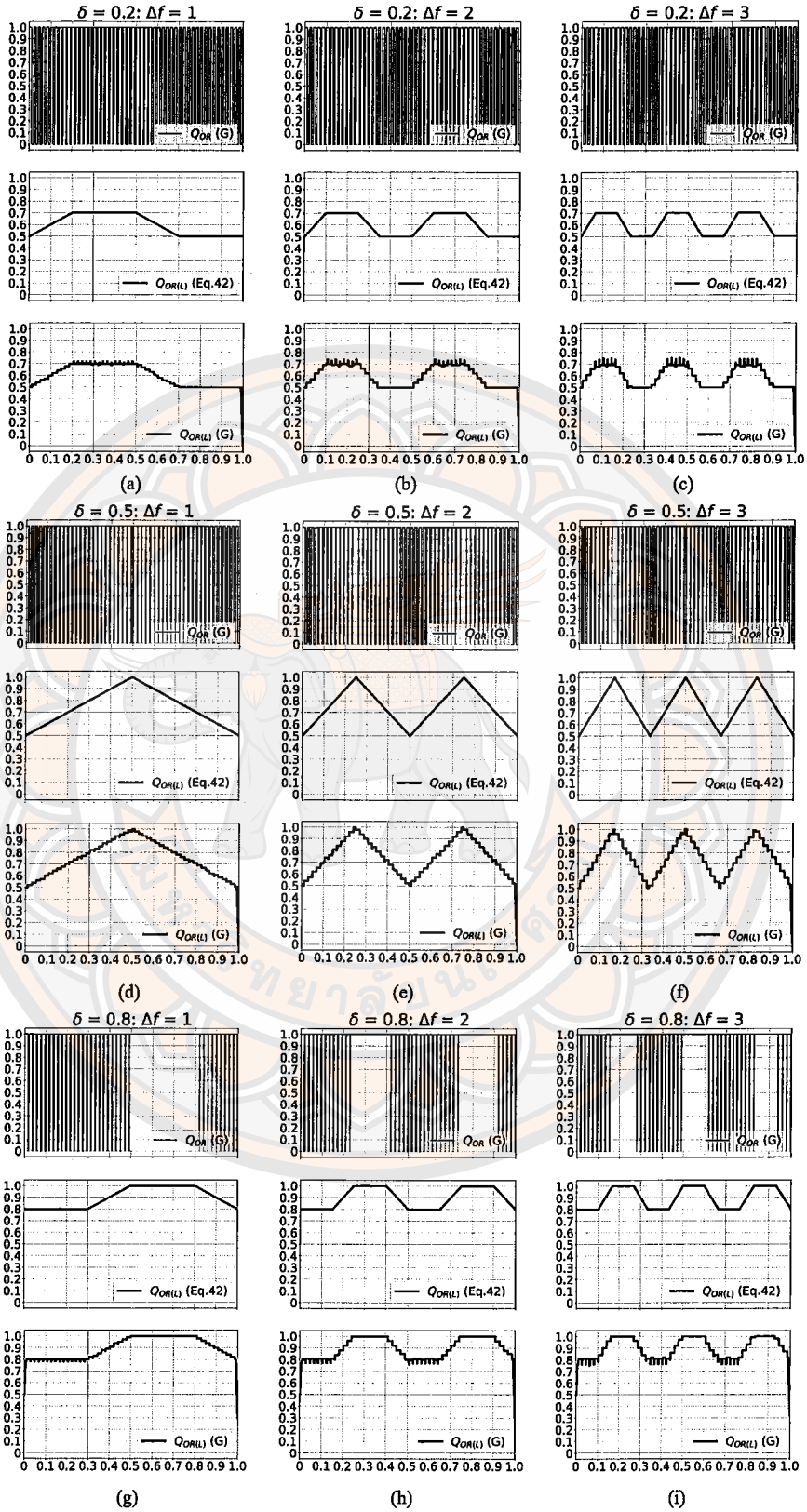

Figure 27 **Simulation results of the OR operator for $f_b \neq f_r$; (a)–(i): $\delta = \{0.2, 0.5, 0.8\}$, $\Delta f = \{1, 2, 3\}$.**

ditions ($f_b = f_r$ and $f_b \neq f_r$) confirms that the analytical formulation of $Q_{\mathrm{OR(L)}}$ reliably represents the behavior of the OR operator. While the waveform shape remains unchanged for a given value of δ, the key distinction lies in the temporal behavior of the signal. Specifically, when $f_b \neq f_r$, the signal is modulated at a beat frequency of $\Delta f = |f_r - f_b|$, and the simulation result $Q_{\mathrm{OR(L)}}(\mathrm{G})$ may exhibit slight ripples due to the limitations of averaging-based low-pass filtering. In contrast, for the equal-frequency case ($f_b = f_r$), the waveform is stationary with respect to the phase offset ϕ_0, and both the analytical and simulated signals are identical and ripple-free.

A comparison between the AND and OR operators reveals that the AND operator consistently generates signals whose magnitudes do not exceed 0.5, whereas the OR operator always produces signals with magnitudes equal to or greater than 0.5. Furthermore, although both operators yield waveforms with the same overall shape, the phases of the resulting signals are reversed relative to each other.

3.6 Discussion of Moiré pattern analysis

This study does not address the distinction between real-Moiré and pseudo-Moiré effects, as discussed in [36]. Instead, the observed dark-light shading, resulting from the overlapping of two gratings, is interpreted as arising from the low-frequency components embedded within the governing equations. In this context, the algebraic relationships represented by the AND and OR logical operators, are formulated as multiplicative expressions in equations (3.4) and (3.5) [1].

By substituting values for the duty cycle, frequency, and phase difference into the Fourier series and processing them through equations (3.4) and (3.5), the resulting output signal can be decomposed into five distinct subgroups. Upon removing the high-frequency terms, the remaining low-frequency component determines the brightness and contrast patterns of the Moiré image.

Equations (3.23)–(3.26) and (3.39)–(3.42) are best applied within a frequency range where the ratio between the frequencies f_r and f_b satisfies the condition $f_r/f_b < 2$ and $f_b/f_r < 2$. This ensures that the low-pass filter can sufficiently separate the difference frequency $|f_r - f_b|$ from the base frequencies themselves. For example, if $f_b = 50$, then f_r should fall between 25 and 100 to meet this criterion.

Nevertheless, the filtering results, as illustrated in Figures 25 and 27, demonstrate that the signal magnitude after low-pass filtering, represented by $Q_{\mathrm{AND(L)}}$ and $Q_{\mathrm{OR(L)}}$, decreases as the value of Δf increases. This attenuation is influenced by the amount of data used in averaging or by the effective cutoff frequency of the low-pass filter.

The primary contribution of this study, compared to previous works, lies in its analytical framework, which characterizes both the shape and magnitude of the low-pass filtered signal. Beyond enhancing the understanding of the dark-light stripe behavior in Moiré patterns, the results offer practical implications for image processing. Specifically, the filtered output can be used to detect differences in line frequencies between a target and reference image, similar to the operating principle of beat frequency oscillator (BFO) systems used in electronic signal processing.

CHAPTER IV

MOIRÉ PATTERN APPLICATION FOR STRIPE MEASUREMENT

4.1 Overview of the Moiré Pattern for Stripe Density Measurement

The process of stripe density measurement using the Moiré effect begins with understanding how visual patterns are generated when two sets of periodic lines are overlaid on one another. These patterns, known as Moiré patterns, arise due to the interference between the stripe frequencies of the target image and a set of computer-generated grid lines. The resulting visual effect can reveal underlying periodic structures through amplified low-frequency patterns, making it possible to estimate the density of the stripes with greater accuracy.

In this study, the technique is applied to fabric images by first generating synthetic horizontal grid lines on a computer screen and superimposing them over the target image. The nature of the resulting Moiré pattern depends on various parameters, including the frequency and duty cycle of the stripes, as well as their initial alignment. Once the overlapping is established, the system performs a series of image processing steps, including thresholding, noise reduction, and low-frequency signal extraction, to convert the visual pattern into a signal that can be analyzed for stripe counting.

This approach offers a reliable alternative to traditional manual methods, particularly in cases where the stripe patterns are too dense or inconsistent for direct visual measurement. It also allows for automated processing, making it more scalable for real-world applications involving textiles or other structured surfaces. The following sections detail the underlying principles of stripe overlapping, the design of the measurement system, and the procedures used to analyze and extract stripe density from a variety of test images.

4.2 Principles of Overlapping Lines on a Computer Screen

4.2.1 Definition of Related Terms

In the application of the Moiré pattern for stripe density measurement, a set of target stripes to be counted and a computer-generated grid are defined, as illustrated in Figure 28. Figure 28(a) shows the target stripes to be measured, while Figure 28(b) displays the grid lines generated by a computer program. These two sets of stripes are considered to be ideal binary patterns, in which each pixel can take on one of two logic states: logic "1" or logic "0". In this study, the variables illustrated in Figure 28 are defined as follows:

f_s: The frequency (density) of the target stripes to be counted, expressed in lines per unit length (L^{-1}).

f_v: The frequency (density) of the grid stripes generated by the computer program (L^{-1}).

$T_s = 1/f_s$: The period of the target stripes, expressed in length units (L).

$T_v = 1/f_v$: The period of the computer-generated grid stripes (L).

$\delta_s = T_{s1}/T_s$: The duty cycle of the target stripe pattern.

$\delta_v = T_{v1}/T_v$: The duty cycle of the computer-generated grid pattern.

T_{s1}: The length over which the target stripe has a logic state of "1" (L).

T_{v1}: The length over which the computer-generated grid has a logic state of "1" (L).

Note: This study does not include calibration of the image scale to match the actual physical length of the object in the original image. Instead, the focus is placed on frequency measurement using low-frequency signal detection. Consequently, the stripe period is defined in terms of relative length units.

To define the initial phase of the stripe pattern, the starting position on the left side of the white stripe in the target pattern is designated as the reference point, where the initial phase is considered to be zero. For the computer-generated

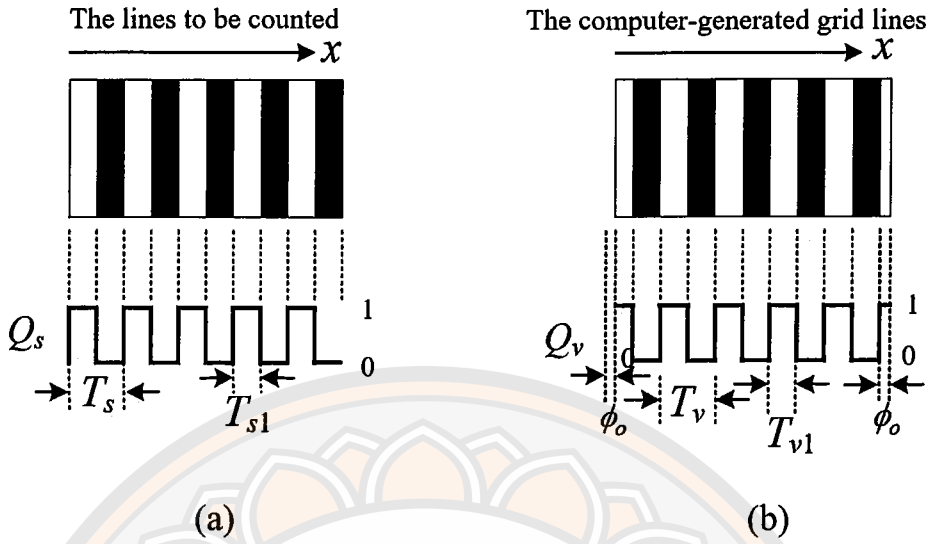

Figure 28 Stripes and logic signals (Q_s and Q_v): (a) The strips to be counted; (b) The Computer-generated grid strips.

stripe pattern, the starting position of the white stripe is assigned as the initial phase position, denoted by ϕ_0, which represents the phase difference between the two stripe patterns.

Both the target and computer-generated patterns are converted into black-and-white images, allowing them to be represented as logic signals with states of "0" and "1." These binary representations are equivalent to square-wave logic signals with an amplitude of 1.

Based on the definitions of the previously mentioned variables, the signal representing the target stripe pattern Q_s, and the signal for the generated stripe pattern Q_v, can be expressed as Fourier series as follows:

$$Q_s = \delta_s + \frac{1}{\pi}\sum_{n=1}^{\infty}\left(\frac{-1}{n}\sin n(\omega_s x - 2\pi\delta_s)\right) + \frac{1}{\pi}\sum_{n=1}^{\infty}\left(\frac{1}{n}\sin n(\omega_s x)\right) \tag{4.1}$$

$$Q_v = \delta_v + \frac{1}{\pi}\sum_{n=1}^{\infty}\left(\frac{-1}{n}\sin n(\omega_v x - 2\pi\delta_v + \phi_0)\right) + \frac{1}{\pi}\sum_{n=1}^{\infty}\left(\frac{1}{n}\sin n(\omega_v x + \phi_0)\right) \tag{4.2}$$

where $\omega_s = 2\pi f_s$ is the angular frequency of the signal Q_s, $\omega_v = 2\pi f_v$ is the

angular frequency of the signal Q_v, and x is the position under consideration.

From equation (4.2), in designing the digital stripe pattern, it is permissible to set $\delta_v = 0.5$, leading to a simplified expression of Q_v as follows:

$$Q_v = \frac{1}{2} + \frac{1}{\pi}\sum_{n=1}^{\infty}\left(\frac{-1}{n}\sin n(\omega_v x - \pi + \phi_0)\right) + \frac{1}{\pi}\sum_{n=1}^{\infty}\left(\frac{1}{n}\sin n(\omega_v x + \phi_0)\right) \tag{4.3}$$

4.2.2 Overlapping of Two Sets of Stripes

If the background of the display window on the computer screen is a color other than black, the black lines displayed are typically interpreted as regions where the signal is in the logic "1" state. However, from the computer's perspective, a black pixel on the screen has a grayscale value of 0, while a white pixel has a value of 255. When the grayscale values are normalized such that the maximum value is 1, a white pixel is considered to have a logic state of "1", and a black pixel is considered to have a logic state of "0". Therefore, the visible image resulting from the superposition of the target stripe pattern and the computer-generated stripe pattern can be considered as the output of a NOR operation between two logic signals. This relationship can be expressed in the form of logic as shown in equation (4.4).

$$Q_{\text{NOR}} = Q_s \text{ NOR } Q_v = 1 - (Q_s \text{ OR } Q_v) \tag{4.4}$$

From equation (4.4), by substituting equation (3.5), we obtain:

$$\begin{aligned} Q_{\text{NOR}} &= 1 - (Q_s + Q_v - Q_s Q_v) \\ &= 1 - Q_s - Q_v + Q_s Q_v \end{aligned} \tag{4.5}$$

By substituting equations (4.1) and (4.3) into equation (4.5) and analyzing in a manner similar to that discussed in Section 3.4, followed by applying a low-pass

filter to eliminate high-frequency components, the resulting signal $Q_{\text{NOR(L)}}$ can be derived. This signal is separated into two cases as follows.

In the case where $f_s = f_v$, the signal becomes:

$$Q_{\text{NOR(L)}} = \begin{cases} \dfrac{1-\delta_s}{2} - \dfrac{|\phi_0|}{4\pi} + \dfrac{|\phi_0 - 2\pi\delta_s + 2\pi|}{4\pi}; \\ \qquad (-\pi) < \phi_0 < (-\pi + 2\pi\delta_s) \\ \dfrac{1-\delta_s}{2} - \dfrac{|\phi_0|}{4\pi} + \dfrac{|\phi_0 - 2\pi\delta_s|}{4\pi}; \\ \qquad (-\pi + 2\pi\delta_s) < \phi_0 < \pi \end{cases} \tag{4.6}$$

In the case where $f_s \neq f_v$, the signal is given by:

$$Q_{\text{NOR(L)}} = \begin{cases} \dfrac{1-\delta_s}{2} - \dfrac{|x/T_m|}{2} + \dfrac{|(x/T_m) - \delta_s + 1|}{2}; \\ \qquad (-T_m/2) < x < ((-T_m/2) + \delta_s T_m) \\ \dfrac{1-\delta_s}{2} - \dfrac{|x/T_m|}{2} + \dfrac{|(x/T_m) - \delta_s|}{2}; \\ \qquad ((-T_m/2) + \delta_s T_m) < x < (T_m/2) \end{cases} \tag{4.7}$$

$$\text{where } T_m = \frac{1}{f_m} = \frac{1}{|f_s - f_v|} = \frac{T_s T_v}{|T_s - T_v|} \tag{4.8}$$

Equation (4.6) shows that when $f_s = f_v$, the signal $Q_{\text{NOR(L)}}$ becomes a constant value that depends on δ_s and ϕ_0. If ϕ_0 is varied by setting δ_s to three specific values, the signal characteristics differ accordingly.

In the case where $\delta_s = 0.5$, the signal exhibits a triangular waveform, with a maximum value of 0.5 and a minimum of 0. For $\delta_s < 0.5$, the maximum and minimum values are 0.5 and $0.5 - \delta_s$, respectively. For $\delta_s > 0.5$, the maximum is $1.0 - \delta_s$ and the minimum is 0. These values are summarized in Table 8.

Figure 29 illustrates the graphs based on equation (4.6) for $\delta_s = 0.3, 0.5,$ and 0.7. The signal magnitude and shape vary with δ_s. Specifically, at $\delta_s = 0.5$, the signal is triangular and exhibits the highest magnitude among the values considered.

From equation (4.6), when the maximum value $Q_{\mathrm{NOR(L)}}(\mathrm{Max})$ and the minimum value $Q_{\mathrm{NOR(L)}}(\mathrm{Min})$ of the signal $Q_{\mathrm{NOR(L)}}$ are plotted as a function of δ_s, the resulting relationship is shown in Figure 30. The midpoint or mean value of the signal $Q_{\mathrm{NOR(L)}}(\mathrm{Mean})$, defined as the average between $Q_{\mathrm{NOR(L)}}(\mathrm{Max})$ and $Q_{\mathrm{NOR(L)}}(\mathrm{Min})$, decreases as the value of δ_s increases.

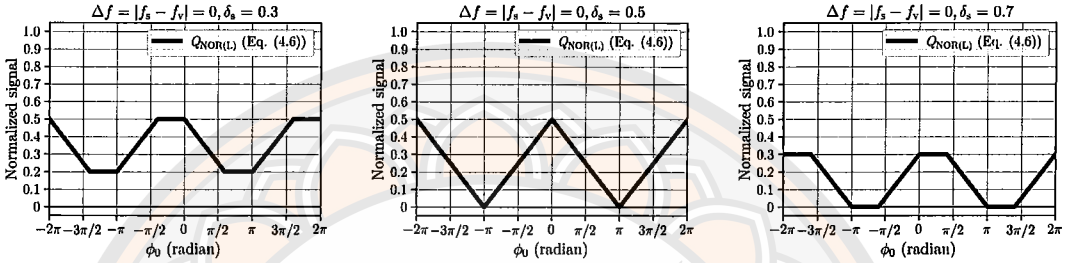

(a) $\delta_s = 0.3$ (b) $\delta_s = 0.5$ (c) $\delta_s = 0.7$

Figure 29 **The $Q_{\mathrm{NOR}(L)}$ signal where $\Delta f = |f_s - f_v| = 0$ and $\delta_v = 0.5$: (a) $\delta_s = 0.3$; (b) $\delta_s = 0.5$; (c) $\delta_s = 0.7$.**

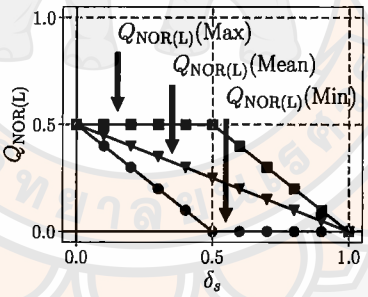

Figure 30 **The maximum ($Q_{\mathrm{NOR}(L)}(\mathrm{Max})$), minimum ($Q_{\mathrm{NOR}(L)}(\mathrm{Min})$), and mean ($Q_{\mathrm{NOR}(L)}(\mathrm{Mean})$) of signal $Q_{\mathrm{NOR}(L)}$.**

According to equations (4.7) and (4.8), when $f_s \neq f_v$, the signal $Q_{\mathrm{NOR(L)}}$ exhibits a frequency f_m, which corresponds to the absolute difference between the frequencies of the two stripe patterns. The waveform shape of this signal depends on the value of δ_s.

Figure 31 presents examples of graphs plotted based on these equations, considering the case where $\Delta f = |f_s - f_v| = 3\,\mathrm{L}^{-1}$, and δ_s is set to 0.3, 0.5, and 0.7, respectively.

Table 8 Summary of $Q_{\mathrm{NOR(L)}}$ signal characteristics when $f_s = f_v$ and $f_s \neq f_v$

Condition	δ Value	Waveform Shape	Max	Min	Average
1	$\delta_s = 0.5$	Triangular	0.5	0	0.25
2	$\delta_s < 0.5$	Clipped triangle	0.5	$0.5 - \delta_s$	> 0.25
3	$\delta_s > 0.5$	Clipped triangle	$1.0 - \delta_s$	0	< 0.25

- When $\delta_s = 0.3$, the signal has a maximum value of 0.5 and a minimum of 0.2, which corresponds to $0.5 - \delta_s$.
- When $\delta_s = 0.7$, the maximum value is $1.0 - \delta_s = 0.3$, and the minimum is 0.

Similarly, in the case where $f_s = f_v$, it is observed that when $\delta_s = 0.5$, the signal $Q_{\mathrm{NOR(L)}}$ takes the form of a triangular waveform when plotted with respect to the spatial coordinate x. In this case, the signal reaches a maximum value of 0.5 and a minimum of 0.

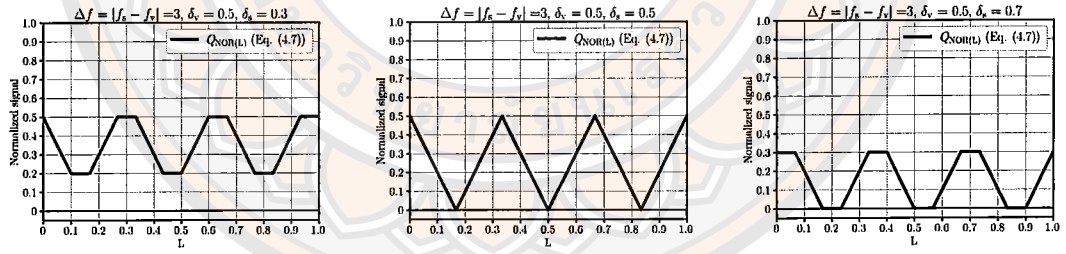

(a) $\delta_s = 0.3$ (b) $\delta_s = 0.5$ (c) $\delta_s = 0.7$

Figure 31 The $Q_{\mathrm{NOR}(L)}$ signal where $\Delta f = |f_s - f_v| = 3$ and $\delta_v = 0.5$: (a) $\delta_s = 0.3$; (b) $\delta_s = 0.5$; (c) $\delta_s = 0.7$.

4.3 Design of Image Processing System for Stripe Density Measurement

The overall process for measuring stripe density using the proposed method is summarized in Figure 32. The procedure begins with loading the target image into the system, followed by image preparation, which includes necessary prepro-

cessing steps such as adaptive thresholding and intensity averaging to enhance the visibility of stripe patterns.

Next, a grid is overlaid on the computer screen and aligned with the stripe pattern of the target image to generate a Moiré pattern. The system then extracts the low-frequency component from the Moiré pattern, after which the frequency of the processed signal is analyzed. Finally, the stripe density is calculated based on the detected frequency.

In the case of checkerboard-patterned fabric, additional preprocessing is required before performing adaptive thresholding. This is due to the alternating intensity levels inherent in checkerboard patterns. The user must first select a region of interest (ROI) where the stripe pattern is clearly visible. This step helps focus the measurement on relevant areas and reduces the influence of background noise caused by color alternation.

Once the ROI is defined, adaptive thresholding and intensity averaging are applied to the selected area to prepare the image for subsequent analysis.

4.3.1 Designing Program Windows

Figure 33 shows the program interface developed for studying and testing the system for measuring the stripe density (frequency) in a target image. The interface consists of four sub-windows that work together in sequence.

The first sub-window displays the superimposed image of the target stripe pattern and the computer-generated grid, which is designed to consist of horizontal stripes. This window is configured with a resolution of 600 pixels in width and 800 pixels in height. When the user clicks the "Load Image" button, the image is automatically resized to fit the designated area. At the top of this window, a frequency sliding bar allows the user to select a column position of interest. The selected column is displayed in a text box labeled H_m (h_m), and the corresponding frequency value is shown in another text box labeled F_m (f_m).

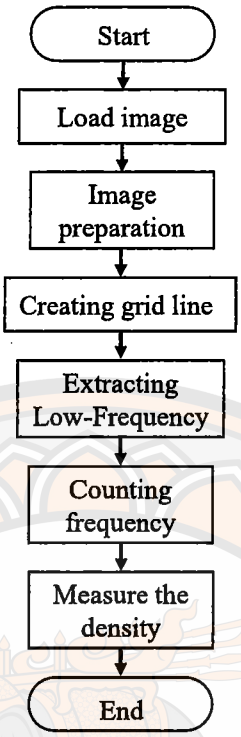

Figure 32 Flowchart of the process

The second sub-window (800 × 256 pixels) shows the $Q_{\mathrm{NOR(L)}}$ signal, which is obtained by extracting the low-frequency component of the Moiré signal at the selected column from the first sub-window. The display scale in this window is set with a minimum value of 0 (black) and a maximum of 255 (white). At the top of this window, there is a text box for the user to input the value of N, which is the window size parameter for the moving average low-pass filter. Additionally, there are buttons for filtering the signal, clearing the output, and adjusting the reference signal level Q_{ref} using a sliding bar. The reference level is used to convert the $Q_{\mathrm{NOR(L)}}$ signal into a square wave signal Q_{sq}.

The third sub-window displays the Q_{sq} signal, which assists the user in selecting an appropriate value for Q_{ref}. For the conversion to be accurate, the frequency of the Q_{sq} signal should match that of the $Q_{\mathrm{NOR(L)}}$ signal. This window also contains command buttons to convert the signal (Sig-to-sq), clear the display, count the frequency of Q_{sq}, and show the frequency count result.

The fourth sub-window shows the measured frequencies of the $Q_{\mathrm{NOR(L)}}$ signal across all columns in the image, based on the data from the first sub-window. An "Auto" function is provided to automatically detect the column where the frequency is zero. Alternatively, the user can manually adjust the sliding bar to browse through column positions, or activate the automatic detection function using the "Auto" button.

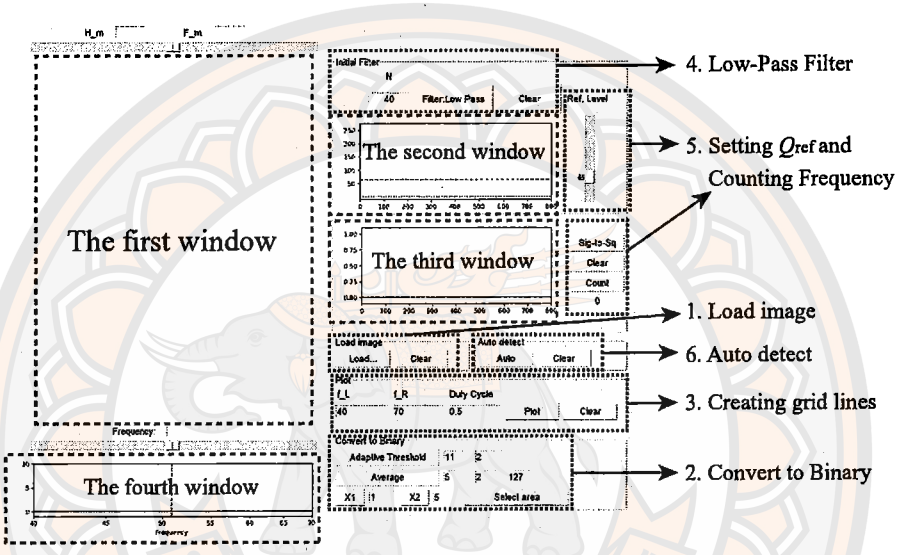

Figure 33 Graphical User Interface (GUI) of the Program with labeled components.

4.3.2 Special Tools for Image Preparation

To ensure that the target stripe pattern image is sufficiently clean and suitable for subsequent processing in this study, several image adjustment tools have been implemented as follows:

- **Adaptive Thresholding**: Activated via the "Adaptive Threshold" button [37], this tool converts the original image into a binary black-and-white format. The process begins by converting the image to grayscale using a method based on Gaussian distribution. Users can specify the block size (i.e., the size of the neighborhood considered for threshold calculation) and the constant C (a value subtracted from the computed threshold) to fine-

tune the result. This produces a grayscale image with a smooth intensity transition, which is then binarized to generate a clear binary representation of the stripe pattern.

- **Averaging Filter**: Accessed via the "Average" button, this tool performs two-dimensional low-pass filtering by averaging pixel values within a user-defined neighborhood around each pixel. It is designed to suppress noise and enhance stripe clarity. Users can specify the number of pixels used for averaging in both horizontal and vertical directions.
- **Cropping Tool**: This function allows the user to extract a specific region of interest from the image by selecting a column range between X_1 and X_2. The cropped image is then scaled to fit the first display window, making it ready for further processing.

4.3.3 Creating Grid Lines on the Computer screen

Creating grid lines on the computer screen, which are displayed horizontally in the first sub-window, serves two main purposes: (1) to overlay on the target image to produce Moiré patterns, and (2) to generate an idealized reference pattern for measurement. In both cases, the position of each point on the screen is determined using two variables: h and v, which represent the horizontal and vertical axes, respectively. The parameters h_0 and $h_{\max}$ denote the minimum and maximum positions along the horizontal axis, while v_0 and $v_{\max}$ represent the corresponding positions on the vertical axis, as illustrated in Figure 34.

The grid design interface includes input fields for entering the duty cycle and the number of stripes to be created. The variables f_L and f_R specify the number of stripe patterns at the left and right edges of the display window, respectively. The "Duty Cycle" field determines the ratio of the white stripe width to the total period in each pattern. If f_L and f_R are set to different values (e.g., $f_L < f_R$), the stripe frequency will gradually increase from the left side to the right side of the

display window.

As described in Section 4.3.1, the stripe frequency corresponding to each column in the first sub-window can be determined by moving the frequency sliding bar to the desired column, denoted by the variable h_m. The frequency value f_m at that column is calculated using equation (4.9):

$$f_m = \frac{f_L \times f_R}{((f_L - f_R) \times h_m / h_{\max}) + f_R} \tag{4.9}$$

This calculated frequency f_m is then displayed at the top of the first sub-window.

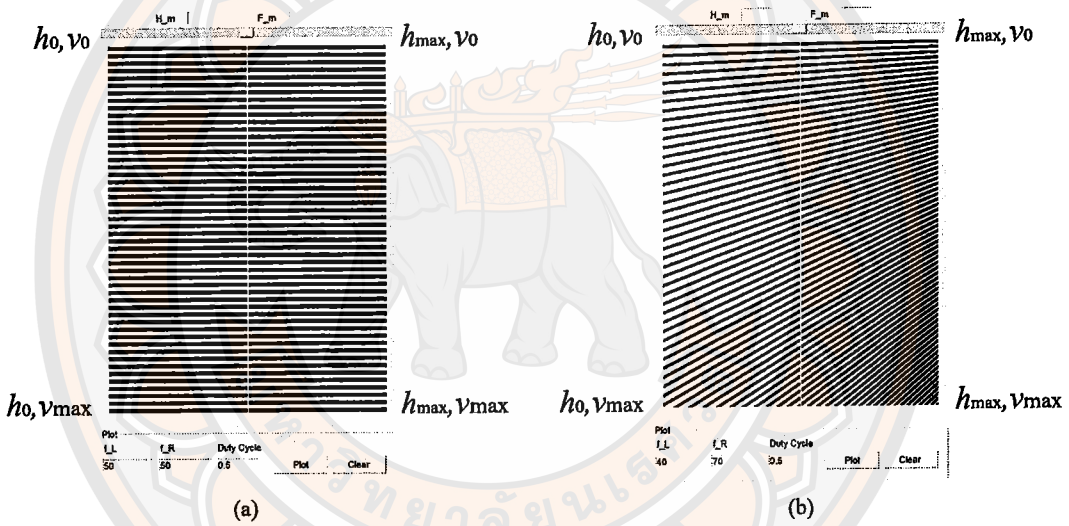

Figure 34 Illustration of the first sub-window under different frequency conditions.

Figure 34(a) illustrates the first display window when the values of f_L and f_R are equal, resulting in a uniform stripe distribution across the window. In this case, adjusting the frequency sliding bar yields $f_m = f_L = f_R$. By contrast, Figure 34(b) demonstrates a scenario where $f_L \neq f_R$, causing the stripe density to increase toward the right side. When the user moves the sliding bar, the program recalculates f_m according to equation (4.9).

The key distinction between the grid lines used for Moiré pattern generation and those used for idealized target images lies in image resolution. For actual target

images, no resolution adjustment is required, and the default size of 600 × 800 pixels is used. However, for simulated images intended for analysis, the resolution is increased to 6000 × 8000 pixels to allow a more detailed study of the low-pass filter performance, as discussed in Section 4.3.4. Once processed, the image is downscaled for display within the program window.

Figure 35 presents a series of results related to Moiré pattern generation and low-frequency signal extraction. In Figure 35(a), the original resolution image is used without enhancement, resulting in clipped low-frequency components due to limited sampling precision. Figure 35(b) shows the outcome after increasing the resolution, which yields a more complete signal consistent with the theoretical expectations described in Section 4.2.2 and supported by previous findings [38]. Figure 35(c) depicts the case where $f_L \neq f_R$ using high-resolution input, generating three visible Moiré fringes. This pattern is comparable to those observed in Figures 35(a) and 35(b).

Figure 36 displays the Moiré pattern generation process applied to a target image loaded without resolution enhancement. Figure 36(a) shows the original image, while Figure 36(b) presents its binarized form. Figures 36(c) and 36(d) illustrate the overlaying of stripe grids with constant and variable frequencies, respectively. The resulting low-frequency signals, displayed at the bottom of Figures 36(c) and 36(d), resemble sinusoidal waveforms. The system is capable of detecting and counting the frequencies of these signals accurately.

4.3.4 Extracting the low-frequency component of the Moiré image

When the "Filter Lowpass" button is activated, the high-frequency components of the Moiré pattern image in the first display window are removed. This operation is applied to the column position h_m selected by the frequency sliding bar. The variable Q_{NOR} refers to the original signal obtained from the Moiré pattern, while $Q_{\mathrm{NOR(L)}}$ denotes the low-frequency signal resulting from this process.

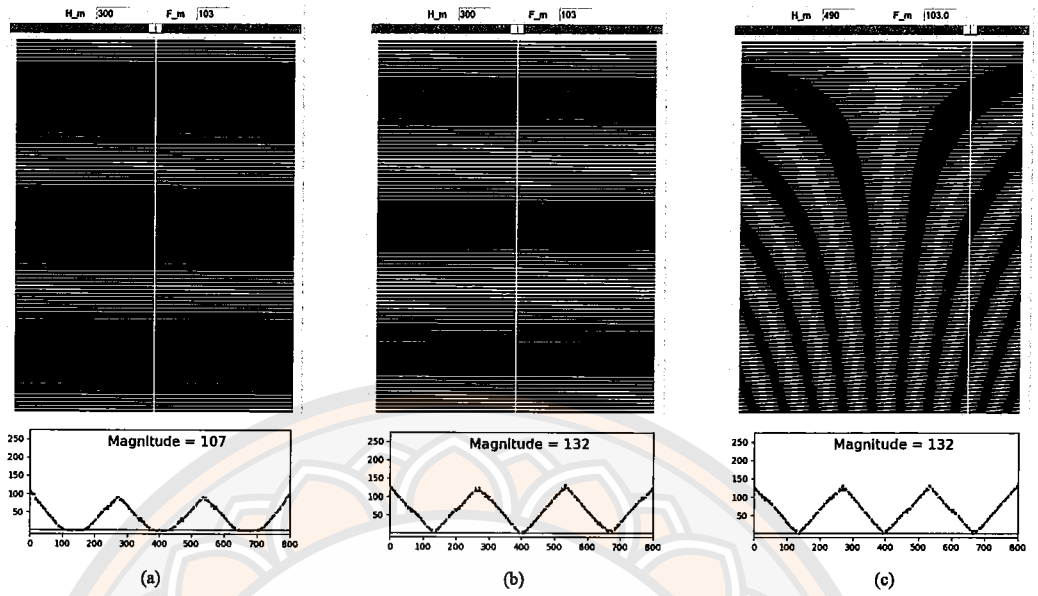

Figure 35 The First and Second Sub-Windows: Processing with and without Resolution scaling; (a) Without resolution scaling, $f_L = f_R$; (b) With 10x resolution scaling, $f_L = f_R$; (c) With 10x resolution scaling, $f_L \neq f_R$.

Although the Moiré pattern is inherently a two-dimensional (2D) image, the signal extraction process in this study focuses only on a single vertical column at position h_m. As a result, the extracted data can be considered a one-dimensional (1D) signal representing the intensity variation along the vertical axis. The vertical line used for averaging appears as a white stripe in the first display window, which serves as the reference position for signal extraction, as shown in Figures 35 to 37. The resulting signal consists of 800 values, corresponding to the height of the image (800 pixels), with intensity levels ranging from 0 to 255. This signal is displayed in the second window of the GUI, as illustrated at the bottom of Figure 35, and in Figure 36(c) and 36(d). Additionally, the peak magnitude of the signal is also visualized within this display.

The filtering procedure consists of two steps: (1) low-pass filtering using a moving average filter, and (2) signal smoothing using the Savitzky–Golay filter [39].

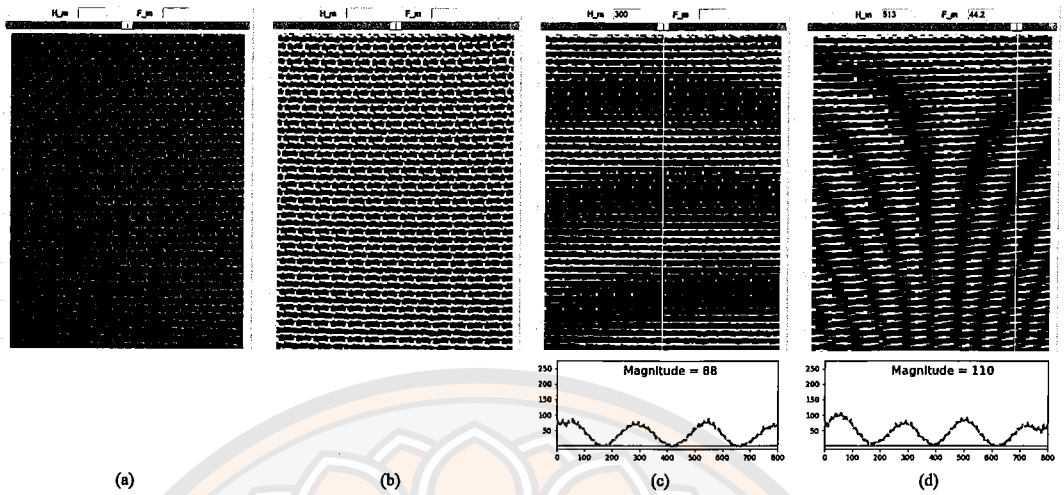

Figure 36 **Examples of image loading, preparation, and overlay drawing in two forms: (a) the original target image; (b) the image obtained by pressing the "Adaptive Threshold" button; (c) the image with a fixed-frequency grid overlay, and (d) the image with a variable-frequency grid overlay.**

In the first step, when the user provides a value for N, the program iterates vertically from (h_m, v_0) to $(h_m, v_{\max})$. At each vertical position v_n, the values of Q_{NOR} from (h_m, v_{n-N}) to (h_m, v_{n+N}) are averaged, and the result is assigned to the location (h_m, v_n), as shown in Figure 37(a).

If $n+N > v_{\max}$, the program averages the values from (h_m, v_0) to $(h_m, v_{n+N-v_{\max}})$, as an alternative, illustrated in Figure 37(b). If $n - N < 0$, the values from $(h_m, v_{n-N+v_{\max}})$ to $(h_m, v_{\max})$ are used instead, as shown in Figure 37(c).

Following the moving average filtering, the signal is further refined using the Savitzky–Golay filter to improve smoothness and reduce ripples. The window size and polynomial order for this filter were selected through empirical testing. A window size of 101 and polynomial order of 3 were chosen to achieve an optimal balance between noise suppression and preservation of signal characteristics.

Smaller window sizes (e.g., 51) retained finer details but allowed residual

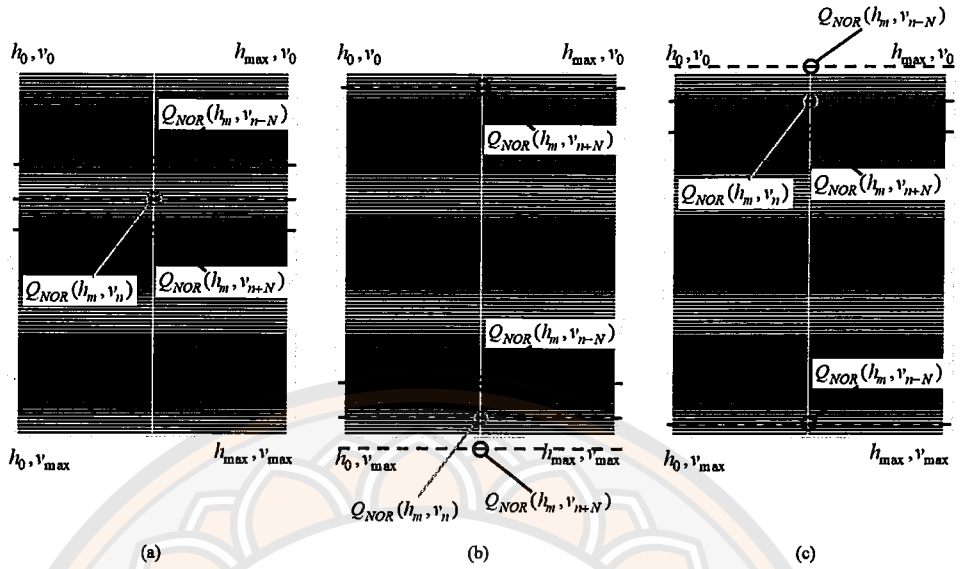

Figure 37 Utilizing data around the point of interest for the moving average filter: (a) $n - N > 0$ and $n + N <$ max; (b) $n + N >$ max; (c) $n - N < 0$.

noise, while larger sizes (e.g., 151) overly smoothed the signal and suppressed meaningful low-frequency content. Similarly, a polynomial order of 2 was insufficient to preserve signal curvature, whereas order 4 introduced undesirable oscillations. The selected parameters ensure that the filtered signal $Q_{\mathrm{NOR(L)}}$ remains both smooth and reliable for stripe density analysis.

The moving average filter was selected for this study based on its simplicity, computational efficiency, and proven effectiveness in extracting the low-frequency components of the $Q_{\mathrm{NOR(L)}}$ signal. Although wavelet transforms offer advantages such as multi-resolution analysis and better adaptability to transient frequency variations, they also require significantly more computational resources. In contrast, the moving average filter enables smooth signal transitions while avoiding phase distortion, which makes it well-suited for Moiré-based stripe density measurement. Experimental results demonstrate that with an appropriately chosen window size, the filter can effectively suppress high-frequency noise while preserving critical low-frequency information. Considering these advantages, particularly

in the context of real-time processing, the moving average filter was considered the most suitable approach for the present study.

4.3.5 Counting the frequency of the $Q_{\mathrm{NOR(L)}}$ signal

The frequency measurement of the $Q_{\mathrm{NOR(L)}}$ signal consists of two main steps. First, the signal is converted into a square waveform Q_{sq} by pressing the "Sig-to-Sq" button. The resulting square wave is displayed in the third sub-window. In the second step, the frequency of Q_{sq} is determined by detecting its rising edges.

During the first step, the original signal $Q_{\mathrm{NOR(L)}}$ is compared to a reference level Q_{ref}. Users can determine this reference value either by visually estimating the midpoint of the waveform or by positioning the vertical sliding bar in the second sub-window near the signal center. The corresponding value is then read and displayed by the program.

A key feature of this reference level is the incorporation of hysteresis, in which the decision threshold toggles between $Q_{\mathrm{ref}} + 5$ and $Q_{\mathrm{ref}} - 5$, similar to the operation of a hysteresis comparator in electronic circuits. Initially, if $Q_{\mathrm{NOR(L)}}$ is less than $Q_{\mathrm{ref}} - 5$, the output Q_{sq} is 0. When the signal exceeds $Q_{\mathrm{ref}} + 5$, the output switches to 1. The value returns to 0 when the signal drops below $Q_{\mathrm{ref}} - 5$.

Pressing the "Count" button initiates the counting process, where the program detects rising edges in Q_{sq} and calculates the frequency. The result is shown in the text box located beneath the "Count" button.

Figure 38 (upper) shows an example of the $Q_{\mathrm{NOR(L)}}$ signal extracted using low-pass filtering, where $f_s = 100$, $f_v = 103$, and $N = 15$. The dashed line indicates the reference level Q_{ref}, and the comparison signal alternates between $Q_{\mathrm{ref}} \pm 5$. Figure 38 (lower) displays the resulting Q_{sq} signal obtained through this process, with a counted frequency of 3.

Several sources of error can affect the accuracy of frequency measurement

for $Q_{\text{NOR(L)}}$, thereby impacting the reliability of stripe density estimation. One significant factor is image resolution. As demonstrated in Figure 35(a), lower resolution may cause aliasing and obscure the extraction of accurate low-frequency components. Additionally, converting $Q_{\text{NOR(L)}}$ into Q_{sq} may introduce distortion, particularly if the threshold value Q_{ref} is not appropriately chosen. If the system incorrectly detects noise as a real signal change, the frequency count may become inaccurate, as illustrated in Figure 38.

The window size N used in low-pass filtering also influences measurement performance. A small N may leave residual high-frequency noise, while a large N can excessively smooth the signal, diminishing the magnitude of $Q_{\text{NOR(L)}}$ and reducing meaningful signal features. Likewise, when the frequency difference Δf is too large, the signal magnitude decays too quickly, causing errors in frequency extraction.

Hysteresis characteristics can further introduce delay or missed transitions if not properly configured. Because hysteresis is defined by $Q_{\text{ref}} \pm 5$, selecting an inappropriate reference level may result in unstable or inaccurate detection, again demonstrated in Figure 38.

To reduce these errors and improve measurement accuracy, it is essential to optimize image resolution, adjust the window size N, and carefully fine-tune the threshold parameters, particularly the reference value Q_{ref}.

4.3.6 Measuring the density of stripe patterns

Once the image of the target stripe pattern is displayed in the first window, the measurement procedure begins with the conversion of the image into a black-and-white format. A computer-generated grid is then overlaid, with its frequency gradually increasing from f_L at the left edge to f_R at the right edge of the window. When the condition $f_L < f_s < f_R$ is true, Moiré patterns appear as curved dark and light bands across the image.

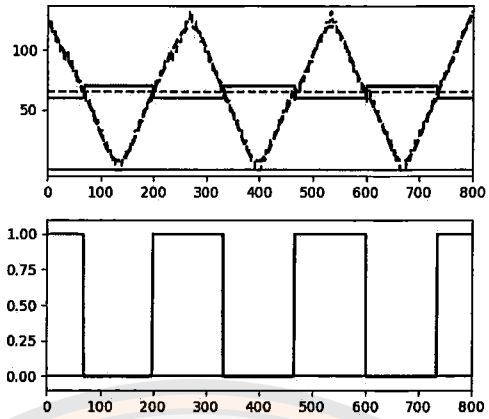

Figure 38 The conversion of the $Q_{\mathbf{NOR}(L)}$ signal into a square wave: Upper-The $Q_{\mathbf{NOR}(L)}$ signal in the second sub-window; Lower-The resulting square wave signal $Q_{\mathbf{sq}}$ in the third sub-window.

There are two ways to perform the density measurement. The first relies on manual adjustment. The user moves the horizontal frequency sliding bar, located at the top of the first display window, to a position where the Moiré bands appear nearly straight. The corresponding value shown as f_m reflects the stripe density at that location.

The second method uses automatic detection. When the "Auto" function is activated, the program begins scanning from the top-left corner at coordinates (h_0, v_0), moving vertically down each column and proceeding from left to right across the entire image. For each column, the program extracts the low-frequency content and calculates the frequency of the $Q_{\mathrm{NOR(L)}}$ signal. The reference value Q_{ref} used in this step can either be set manually or taken from a column previously analyzed by the user. The resulting frequency values are displayed in the fourth window beneath the main image display.

As part of the detection process, the software checks for sequences of three or more consecutive columns where the frequency difference Δf becomes zero. If such a region is found, the program computes the average of the corresponding column

positions and presents it as the system's measured f_s value. To help users identify this region, vertical lines are drawn on the image at those positions. If preferred, the user may bypass the automatic function and instead use the frequency sliding bar in the fourth display window to manually align with the region where $\Delta f = 0$. The value obtained is then shown at the top of the interface.

4.4 Experiments and results

4.4.1 Testing the performance of the moving average filter

To investigate how the moving average filter affects both the magnitude and the shape of the $Q_{\text{NOR(L)}}$ signal, this section presents two sub-experiments. These two signal properties are critical, as they influence the accuracy of the frequency counting process.

In the first sub-experiment, the values of f_s and f_v are kept constant, with a duty cycle fixed at 0.5. The parameter N, which determines the size of the averaging window, is varied across a range. In the second sub-experiment, the value of f_s remains fixed (also with a duty cycle of 0.5), while both f_v and N are varied. Details of the first sub-experiment are provided below.

First Sub-Experiment: Here, f_s is set to 100 and f_v is set to 103, producing a frequency difference Δf of 3. This difference represents approximately 3% of the values of f_s and f_v. The parameter N is tested at twelve different values, ranging from 10 to 100. The results are shown in Figure 39. At $N = 10$, the $Q_{\text{NOR(L)}}$ signal still exhibits noticeable high-frequency ripples. If such a signal were used in frequency detection, these ripples could lead to erroneous counts. When N is increased to values between 15 and 20, the signal begins to resemble a triangular waveform, consistent with the theoretical discussion in Section 4.2.

As N increases further, the amplitude of the $Q_{\text{NOR(L)}}$ signal gradually decreases, and the waveform begins to resemble a sine wave. This transformation

results from the filter suppressing the higher-frequency components inherent in a triangular signal. The trend is illustrated in Figure 40, which plots the magnitude of the $Q_{\mathrm{NOR(L)}}$ signal against different values of N. The magnitude decreases from 146 to 33 as N increases from 10 to 100. If the magnitude of the signal is too low, it may be difficult to distinguish, which can lead to inaccuracies in the frequency counting process.

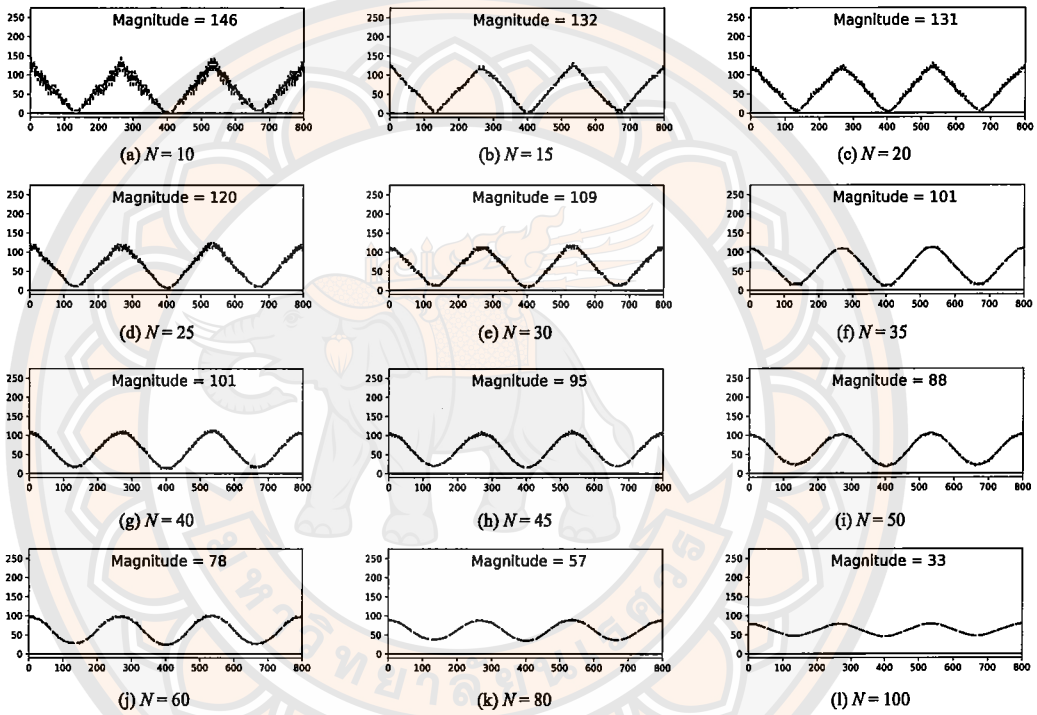

Figure 39 The $Q_{\mathrm{NOR}(L)}$ signal when varying N values from 10-100.

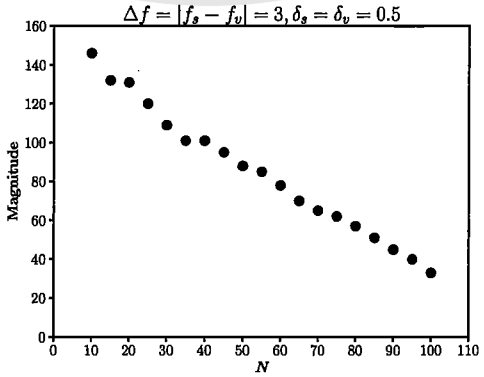

Figure 40 The magnitude of $Q_{\mathrm{NOR}(L)}$ when vary N values.

Second Sub-Experiment: In this experiment, the value of f_s is kept constant at 100, while f_v is varied from 101 to 109. For each value of f_v, the filter window size N is also adjusted across a range from 20 to 60 in separate trials. Figure 41 presents examples of the $Q_{\text{NOR(L)}}$ signal waveform when N is set to 50. The frequency difference $\Delta f = |f_v - f_s|$ is evaluated for values from 1 to 6.

When Δf equals 1, the resulting $Q_{\text{NOR(L)}}$ signal takes the form of a triangular waveform. As Δf increases, the waveform gradually transforms and begins to resemble a sine wave. This behavior occurs because the higher-frequency components are increasingly attenuated, illustrating the low-pass characteristics of the moving average filter.

In addition, the ripple amplitude caused by residual high-frequency components remains relatively unchanged, which can be attributed to the fixed filter window size of $N = 50$ throughout these cases. Figure 42 displays a plot of the $Q_{\text{NOR(L)}}$ signal magnitude as a function of both Δf and N. The results show that the signal magnitude decreases as Δf increases, with larger values of N causing a steeper decline in the amplitude of $Q_{\text{NOR(L)}}$.

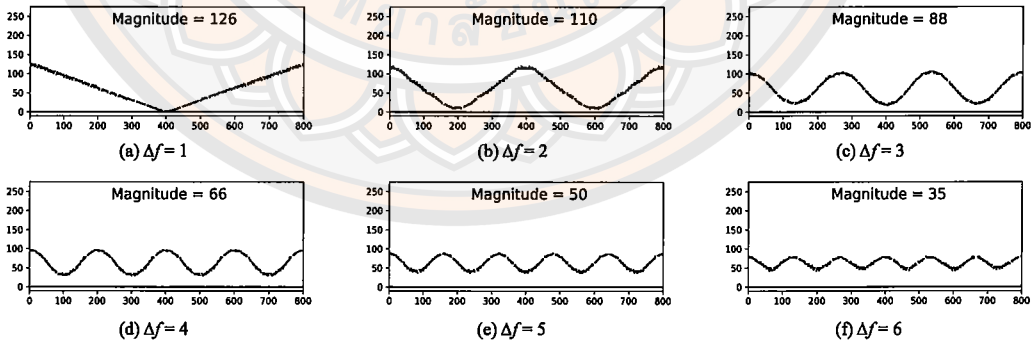

Figure 41 The $Q_{\text{NOR}(L)}$ signal when varying Δf in the range of 1-6 with $N = 50$.

4.4.2 Measuring the density of stripe patterns simulated by a computer program

To evaluate the performance of the proposed measurement system, parallel

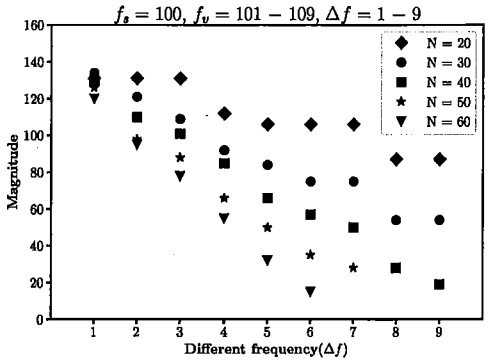

Figure 42 The magnitude of $Q_{\mathrm{NOR}(L)}$ when varying $\triangle f$ and N

binary stripe patterns with uniform frequency were generated using a computer simulation. This uniformity implies that the spacing between adjacent stripes remains constant. In accordance with the procedure described in Section 4.3.3, the resolution of the data used to create these patterns was increased by a factor of ten compared to the standard resolution.

For this test, the frequency of the target stripe pattern (f_s) was systematically varied from 30 to 180 L^{-1} in increments of 30 L^{-1}. The Revealing grid was designed so that its frequency gradually increased from left to right across the display window. The frequency at the left edge was set to $f_s - 5$ L^{-1}, while the frequency at the right edge was set to $f_s + 5$ L^{-1}.

Several values of Q_{ref} were selected, as listed in Table 9. For this experiment, the filter window size N was fixed at 50. The corresponding measurement results are shown in two columns: the manually obtained values are listed in the first column, while the values calculated using the proposed method are shown in the rightmost column.

As shown in Table 9, the values of f_s represent the stripe densities generated from simulation and are treated as the reference values measured manually. In comparison, the values labeled as F_m were obtained using the proposed measurement method. The results reveal that the automated method achieves perfect agreement with the reference values, as the measurement error is zero in all cases.

Table 9 Parameters and results for simulated stripe pattern images

f_s (L^{-1})	N	Q_{ref}	f_L	f_R	F_m
30	50	63	25	35	30.0
60	50	53	55	65	60.0
90	50	50	85	95	90.0
120	50	55	115	125	120.0
150	50	49	145	155	150.0
180	50	47	175	185	180.0

This high accuracy is largely due to the ideal nature of the test images used in the experiment. These images were generated synthetically with evenly spaced binary stripe patterns of consistent intensity, eliminating most forms of variation. Such controlled conditions provide a favorable environment for testing the algorithm. In contrast, real woven fabric images often contain irregularities such as non-uniform spacing, inconsistent thread thickness, and lighting variations, all of which can influence measurement accuracy. These more complex conditions and their effects are examined further in Table 10.

Figures 39 through 42 highlight the role of low-frequency component extraction in stripe density measurement. Figure 39 illustrates how adjusting the parameter N in the moving average filter influences the shape and magnitude of the extracted $Q_{NOR(L)}$ signal. Increasing N leads to a smoother waveform and helps suppress high-frequency noise.

Figure 40 presents a quantitative analysis of how different values of N influence the magnitude of the extracted signal. The observed trend provides practical guidance for selecting appropriate filter parameters to achieve accurate frequency detection. Figure 41 illustrates the effect of varying the frequency difference Δf on the extracted signal, with the filter window size fixed at $N = 50$. The results

indicate that when Δf exceeds 5 L^{-1}, the signal magnitude becomes too low for reliable frequency detection. These findings highlight the importance of selecting an appropriate range of Δf in relation to a given N value.

Figure 42 extends the analysis by examining the relationship between N and Δf across different frequency ranges. When $N = 40$, the system maintains accuracy across all Δf values and exhibits a nearly linear response. However, for $N = 20$ and $N = 30$, although the method still functions across the full range, the relationship between input and output becomes non-linear. For N values greater than 40, the usable range of Δf narrows, and the magnitude of the extracted signal decreases more rapidly, reducing the system's ability to resolve higher frequency variations.

Based on these observations, Figure 42 suggests that all tested N values remain effective when $\Delta f = 5$ L^{-1}. In practical applications, this implies that the frequency variation near the edges of an image should not exceed 5 L^{-1} to maintain stable and reliable measurement results. These insights are useful for defining the optimal parameter settings when applying low-frequency component extraction in real-world stripe density measurement tasks.

Figure 43 presents examples of the program in operation. In Figure 43(a), a Moiré pattern is shown, created by overlaying the simulated stripe pattern with the grid generated by the program. Figure 43(b) illustrates how the reference value Q_{ref} is selected. This involves analyzing the low-frequency component extracted from a chosen column to determine a suitable reference level. Figure 43(c) displays the result after activating the automatic detection function. The program processes the image, adjusts the frequency sliding bar in the fourth display window to the appropriate column where the low-frequency signal reaches zero, and presents the corresponding frequency value at the top of the window.

Figure 44 shows an example of the final output from the system when ap-

plied to simulated stripe images. The measured values are shown to be in close agreement with the test frequencies, confirming the system's accuracy under controlled conditions.

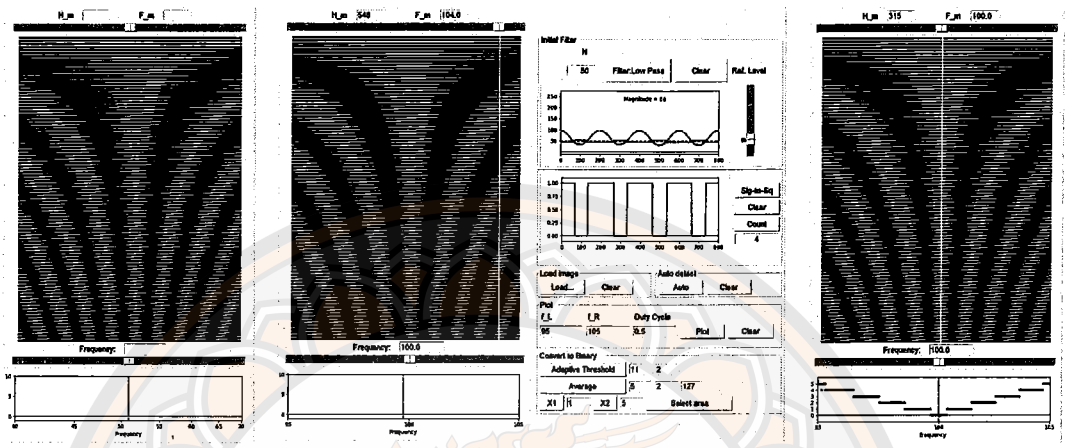

Figure 43 Program operation and the technique for selecting $Q_{\mathbf{ref}}$ when the target image is a simulated grid pattern.

4.4.3 Measuring the density of stripe patterns in fabric images

For stripe images that are relatively simple in appearance, such as monochrome fabric with evenly spaced lines and a density below 120 L^{-1}, an image resolution of 600×800 pixels has been found to be sufficient for accurate analysis in this study.

Figure 45 illustrates the full sequence of operations performed by the system. The process begins with loading the target image into the first display window, as shown in Fig. 45(a). The next step, Fig. 45(b), involves converting the image into a binary black-and-white version using the adaptive thresholding feature. Once binarized, grid lines are overlaid to form Moiré patterns, as shown in Fig. 45(c). In Fig. 45(d), the image is further processed using intensity averaging to reduce high-frequency noise. Finally, Fig. 45(e) displays the output after applying the automatic detection feature. For this particular sample, the stripe density detected by the system closely matches the result obtained through manual counting.

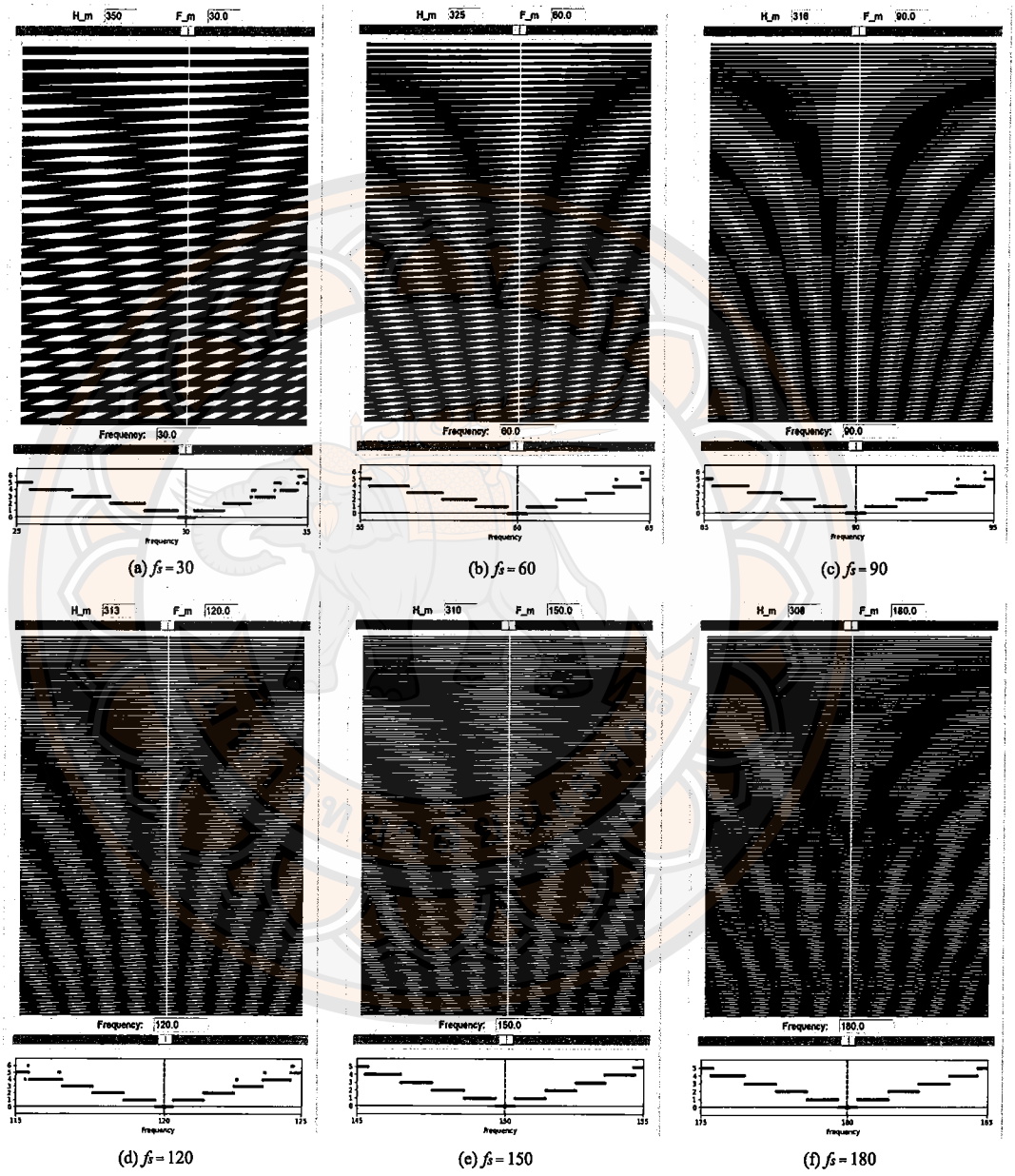

Figure 44 The frequency measurement results of simulated stripe patterns generated by the computer program.

Additional examples are presented in Fig. 46, which shows six different fabric samples with varying stripe densities. The measurement results and their corresponding parameters are summarized in Table 10. To assess the reliability of the proposed method, an error analysis was performed using the percentage deviation defined in equation (4.10):

$$\text{Error} = \frac{|x - y|}{y} \times 100\% \tag{4.10}$$

Here, x represents the frequency measured by the program, while y refers to the reference value obtained through manual counting. This formula provides a normalized percentage error, offering a consistent basis for comparison across different cases.

The selected error metric is consistent with previous work, such as that of Zhang et al. (2016) [24], who used the same method to evaluate the accuracy of automated systems for measuring fabric density. This approach has become a standard in the analysis of high-density woven materials, helping ensure consistent evaluation criteria across different studies.

Results from all six samples demonstrate that the proposed method can accurately estimate stripe density, with deviations remaining within ± 1 L^{-1}. Although Fig. 46 reveals minor discrepancies near the edges of the fourth display window, likely due to Moiré distortion and localized noise, the overall agreement with manual measurements remains strong.

A closer look at the error values shows that the highest deviation observed is 0.71%, while the average across all six samples is 0.24%. These findings confirm that the system not only performs with high precision under controlled conditions but also remains resilient in areas with modest noise interference.

4.4.4 Measuring the density of checkerboard stripe patterns

When the target fabric contains a checkerboard-style stripe pattern, such

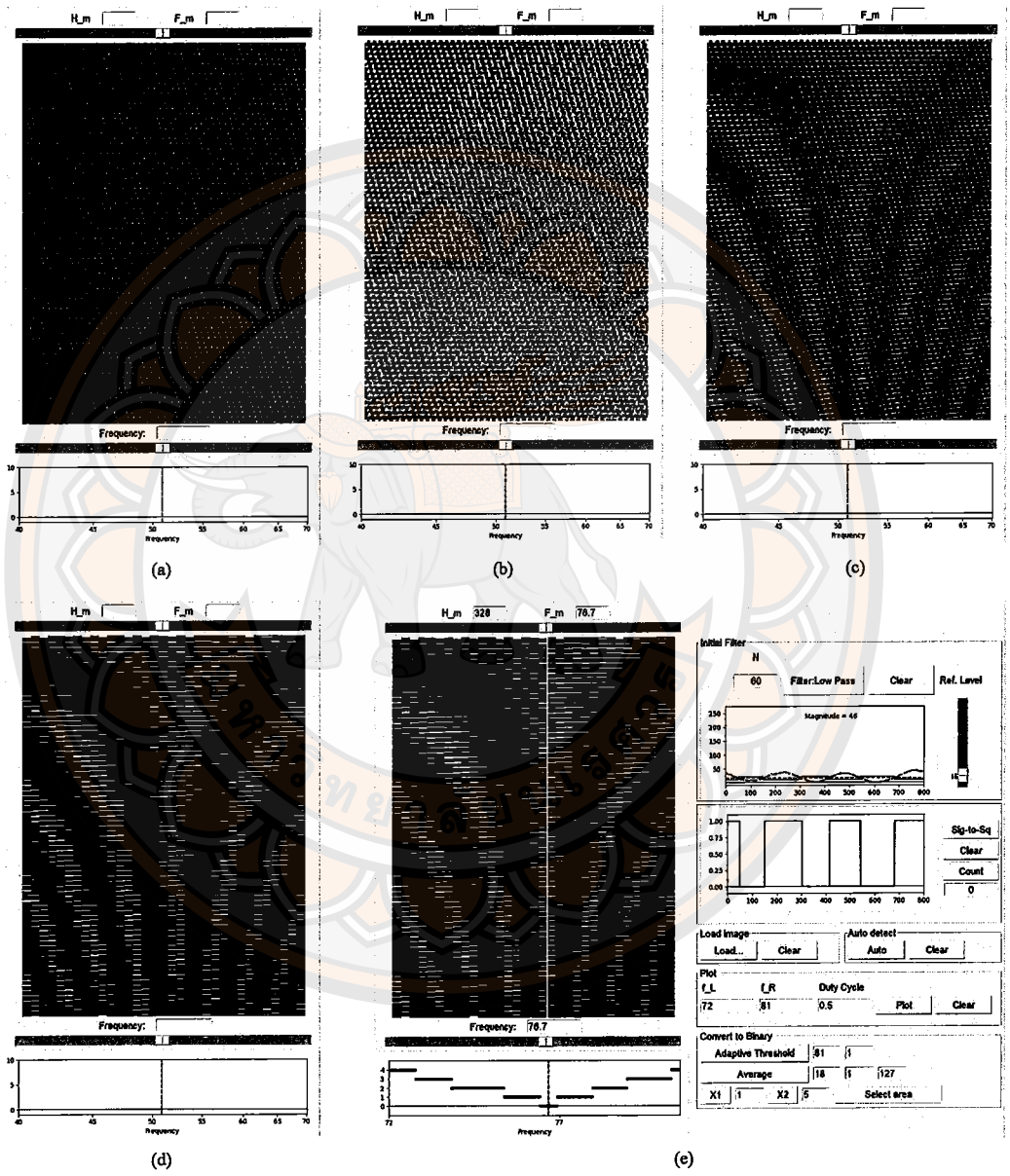

Figure 45 Program operation for processing a loaded target image.

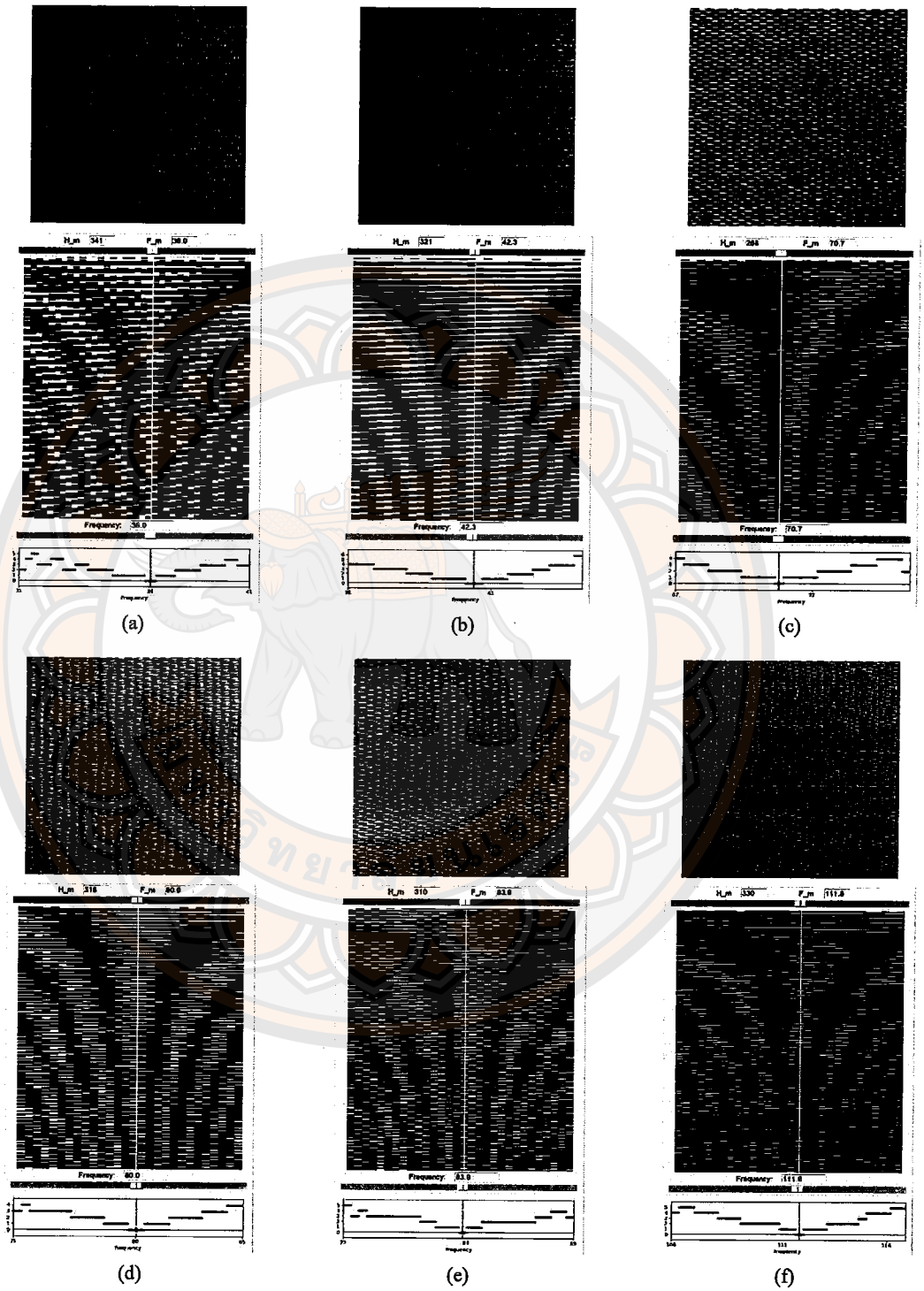

Figure 46 The stripe frequency measurement results from six fabric images.

Table 10 Parameters and results for six real fabric stripe pattern images

Fig. 46	N	Q_{ref}	f_L	f_R	Adap. Thr.		Avr.		F_m	Manual	Error
Sample			L^{-1}	L^{-1}	Thr.	C	x	y	L^{-1}	L^{-1}	(%)
(a) Sample1	50	51	31	41	51	2	16	4	36.0	36	0.00
(b) Sample2	40	60	38	47	71	2	21	1	42.3	42	0.71
(c) Sample3	60	28	67	76	101	4	21	1	70.7	71	0.42
(d) Sample4	60	45	75	85	21	1	21	4	80.0	80	0.00
(e) Sample5	50	45	79	89	31	1	20	2	83.9	84	0.12
(f) Sample6	50	32	106	117	21	1	20	1	111.8	112	0.18

as the one shown in Fig. 47(a), the overlay of grid lines tends to produce a disorganized Moiré pattern. This visual complexity makes it difficult to extract the low-frequency components needed for measuring stripe density with accuracy.

To resolve this issue, the program includes a tool that allows users to crop a specific section of the image. As illustrated in Fig. 47(b), the cropping area can be defined by adjusting the frequency sliding bar to focus on the region where the stripe pattern appears most uniform. Once the desired section is extracted, it is converted into a binary image. Although this process may still leave behind some visual noise, further refinement can be performed using the averaging function, as shown in Fig. 47(d). The resulting image closely resembles the simulated yarn structure discussed in Section 4.4.1, although slight variations in spacing and yarn thickness may still be observed.

After preprocessing, the program proceeds to generate a Moiré pattern by overlaying grid lines and then applies the automatic detection function. In this case, the system calculates a stripe density of 19.3 L^{-1}, as seen in Fig. 47(e). Since the measurement is based on half the checker pattern, doubling this value gives

38.6 L^{-1}, which is nearly identical to the manual count of 39 L^{-1}. This result confirms that the method maintains a high level of accuracy, even when analyzing more complex stripe patterns.

Although noise artifacts appear in the initial binarized image, as shown in Fig. 47(c), the averaging function significantly reduces these irregularities. Without this step, residual white lines could be mistaken for additional stripes, which would lead to an overestimated result. Likewise, variations in yarn spacing may cause inconsistencies in stripe recognition, reducing the reliability of the measurement. Figure 48(b) provides additional insight by comparing the original checkerboard fabric image with the processed version. The visual comparison highlights how noise removal and stripe normalization contribute to more accurate density estimation.

Figure 48(a) further demonstrates the method's effectiveness when applied to different types of fabric. The figure presents a side-by-side comparison of a fabric image from Fig. 45, showing the transformation from the raw input to the final processed output. This comparison confirms that the proposed system remains reliable across a range of fabric textures. By reducing visual artifacts and normalizing stripe characteristics, the program consistently produces results that are in close agreement with manual counting, even when dealing with complex patterns.

4.5 Discussion of Moiré Pattern Application

The findings presented in Section 4.4.1 confirm that applying a moving average filter serves as an effective method for removing high-frequency components from the $Q_{\mathrm{NOR(L)}}$ signal. Increasing the number of data points used in the averaging process produces a result comparable to decreasing the cutoff frequency in a conventional low-pass filter used in electronics. This leads to the suppression or elimination of high-frequency content in the signal.

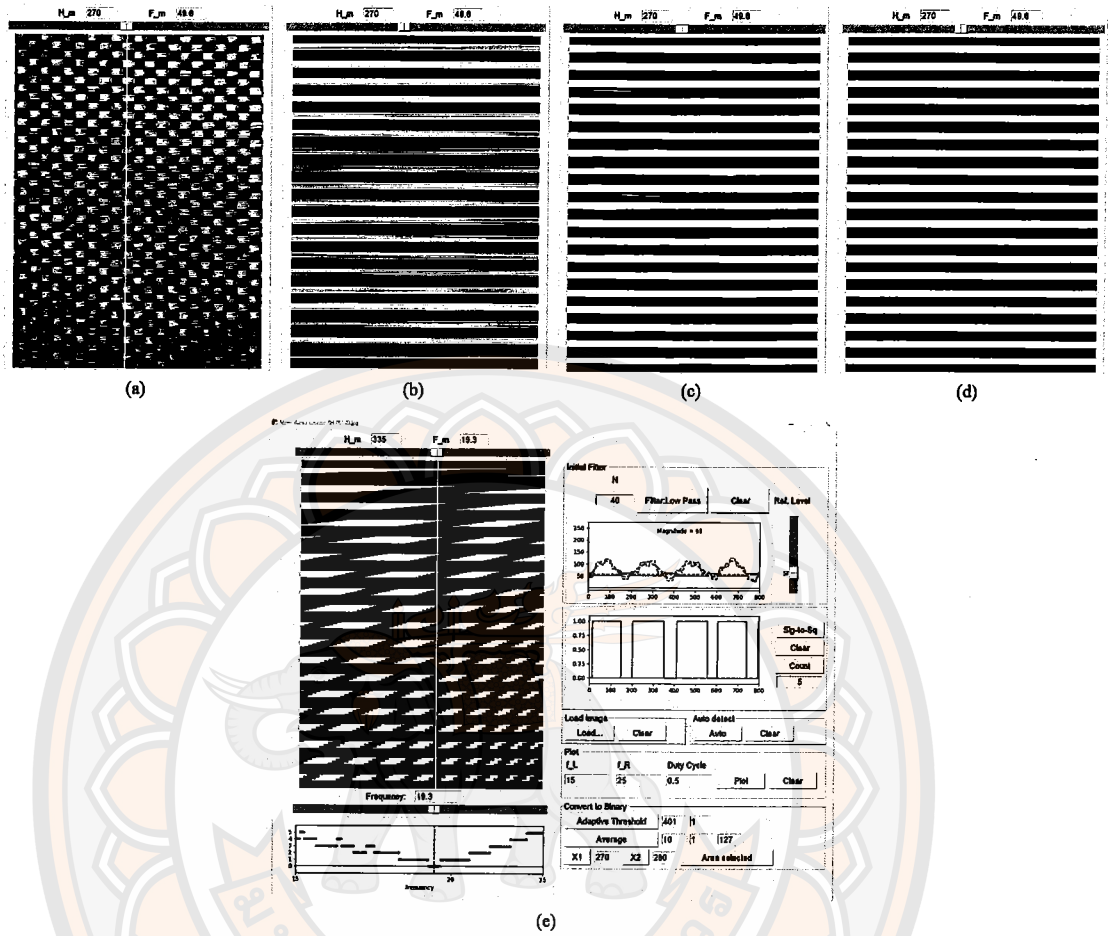

Figure 47 Stripe frequency measurement of a checkered fabric image.

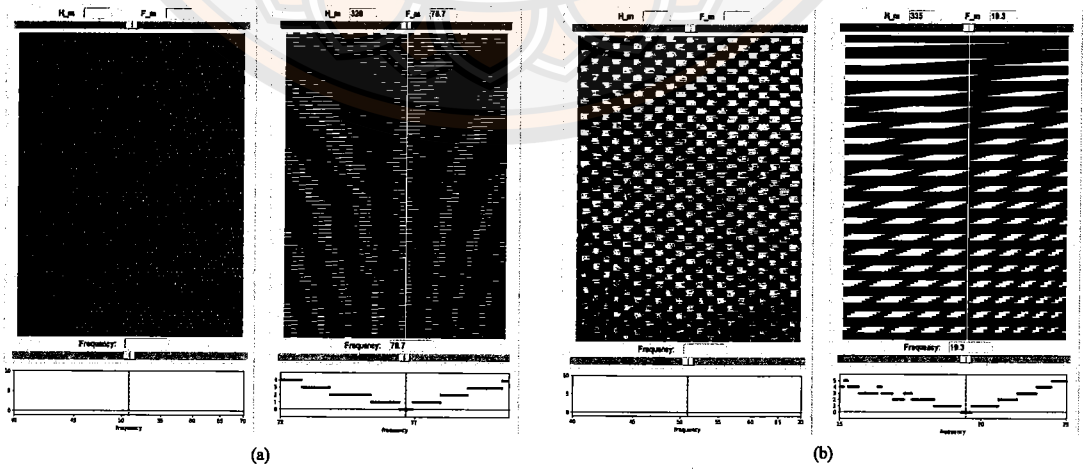

Figure 48 Comparative visualization of raw and processed images demonstrating the effectiveness of the proposed method.

Choosing an appropriate value for N, which represents the number of points used in the moving average filter, is essential for achieving accurate stripe density measurements. When the value of N is too small, residual high-frequency components may remain in the signal. On the other hand, using a value that is too large can cause the low-frequency component of interest to be reduced in magnitude, which may affect the measurement result.

The experiment described in Section 4.4.2 focused on stripe patterns generated under idealized conditions. These simulated patterns featured evenly spaced, straight lines without curvature, and their duty cycles were relatively uniform. Minor variations in spacing were attributed to the resolution of the display window used to draw the patterns. Compared to the tests conducted in Sections 4.4.3 and 4.4.4, this experiment used simpler input data, which allowed for clearer interpretation of the filter's behavior.

Based on the results, it was observed that the moving average filter performed more effectively when measuring high-density stripe patterns. In such cases, the separation between high- and low-frequency components becomes more distinct, enabling the filter to isolate the desired signal features with greater accuracy.

The experiments in Sections 4.4.3 and 4.4.4 were conducted using fabric stripe patterns that presented more complexity compared to ideal patterns. These samples featured vertical stripe orientations, non-uniform duty cycles, and frequency values that varied across different positions in the image. In addition, as the spacing between the threads increased, some yarn lines began to curve, further contributing to the irregularity. Despite these challenges, the images were successfully processed using the system's built-in enhancement tools. The proposed method was then able to measure stripe density effectively from these more complex fabric samples.

Figures 39 and 41 present results that help illustrate how the shape of

the $Q_{\mathrm{NOR(L)}}$ signal changes in response to these variations. In Figs. 39(a)–39(c) and 41(a)–41(b), the signal appears in the form of a triangular waveform. This result is consistent with the theoretical expressions in equations (4.7) and (4.8), which describe the case where the grid and target stripe frequencies differ ($f_v \neq f_s$). In contrast, the signals shown in Figs. 39(d)–39(l) and 41(c)–41(f) take on a sinusoidal shape. This transformation occurs due to the low-pass filter, which removes or attenuates high-frequency components, leaving behind a smoother signal.

In the special case where the frequencies are equal ($f_v = f_s$ or $\Delta f = 0$), equation (4.6) predicts that the $Q_{\mathrm{NOR(L)}}$ signal should exhibit a constant amplitude, depending on how the generated grid lines overlap with the fabric's stripe pattern. Although this study does not include experiments that vary the alignment position systematically, some visual evidence of the superposition effect can still be observed. This effect is most clearly seen in the first display window of the program interface, as shown in Figs. 43(c), 44(a)–44(f), and 45(e). In these examples, the column corresponding to the detected zero-frequency region is marked by a vertical white line, indicating the position of perfect alignment between the stripe pattern and the overlay grid.

A comparison between the proposed method and previously published approaches [28, 29, 40] reveals a shared foundational concept. All of these techniques rely on measuring high-frequency or high-density stripe patterns by suppressing the frequency components to isolate and analyze the resulting low-frequency signals. This strategy avoids the challenges associated with direct detection of high-frequency details. In particular, the methods introduced in [28] and [40] work by sampling image signals at frequencies that are close to the density of the stripe patterns. In contrast, both the present study and the method in [29] take a different approach, using computer-generated grid lines superimposed onto the target image to generate Moiré patterns.

One notable advantage of the grid-based superposition approach, as implemented in [29] and in this study, is its ability to serve as a visual tool for preliminary estimation or backtracking verification of stripe density. The Moiré patterns that result from the overlay process offer clear visual cues, such as the presence of straight or curved fringes. These cues help users evaluate the regularity of stripe distribution across the target image more effectively.

In terms of robustness, the proposed method has shown the ability to measure yarn density even when the image contains minor imperfections. These include slightly curved yarns or irregular spacing between the threads. In contrast, the sampling-based methods described in [28] and [40] are more appropriate for cases where the stripe spacing is uniform. Any deviation in the position of the stripes can have a direct impact on the accuracy of the measured signal. Additionally, since these methods focus on isolating low-frequency components only, it becomes more difficult to verify the quality or consistency of the extracted signals.

For practical applications, the proposed system could be further improved by integrating a real-time digital microscope for image capture. This would allow users to import images directly into the analysis system. The software interface could also be designed to support both automatic and manual operation modes, depending on the user's preference. Manual mode would be especially helpful for validating results or adjusting parameters such as frequency filtering and reference signal levels. Once suitable parameters have been established, the system can be switched to automatic mode to speed up the measurement process and ensure consistent accuracy across multiple samples of similar fabric types.

CHAPTER V

SUMMARY

5.1 Summary of Logical Operator Analysis for Binary Gratings

This study introduces a technique for analyzing Moiré patterns formed by overlapping binary parallel gratings. The approach models the interaction between two gratings as a logical operation, either AND or OR, applied to corresponding binary signals. Simulation results for both operations were found to be consistent with the analytical equations derived earlier.

The characteristics of the resulting Moiré patterns are influenced by several parameters, including the duty cycle, frequency, and initial phase or positional alignment of the gratings. The simulations also revealed that the transition between dark and light regions becomes most distinct when both gratings have a duty cycle of 0.5.

However, in many practical cases, it is not possible to control the duty cycle of the Base grating, since this layer often represents the object under investigation. In such situations, it becomes important to set the duty cycle of the Revealing layer to 0.5 in order to enhance the visibility of the resulting pattern and ensure accurate interpretation.

5.2 Summary of Moiré Pattern Application in Stripe density Measurement

This study presents an alternative approach to measuring stripe density by using image processing techniques that take advantage of the Moiré phenomenon and low-frequency component extraction. The method is designed to improve measurement accuracy while minimizing hardware complexity and cost. By applying a moving average filter, the system is able to isolate low-frequency signals, allowing it to work effectively with a range of structured surfaces, not limited to textiles.

Compared with manual counting methods, the proposed technique offers better consistency and higher accuracy, especially when analyzing non-uniform or high-density stripe patterns. Experimental results confirm that the extracted signals align well with theoretical expectations and previously published work [38]. The method achieves an average error of only 0.24%, as shown in Table 10.

Looking ahead, future developments may focus on extending the system's capabilities to handle more complex two-dimensional stripe patterns. Incorporating artificial intelligence for pattern recognition could also improve the system's ability to handle noise and irregularities. These improvements would support broader applications, including surface characterization in fields such as optics, printing, and semiconductor manufacturing.

Overall, the findings demonstrate that combining Moiré pattern analysis with low-frequency signal extraction provides a practical and scalable solution for stripe density measurement. The technique holds promise for further optimization and could serve as a foundation for automated quality control systems in various industrial settings.

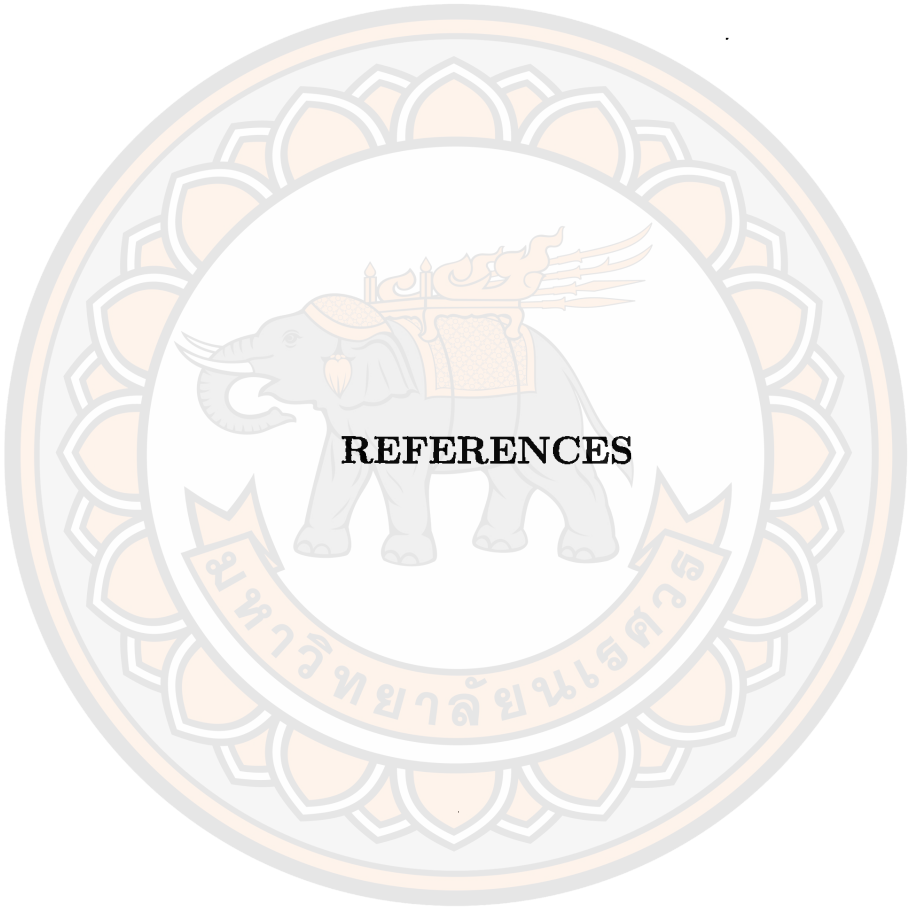

REFERENCES

REFERENCES

1. Kaewpoonsuk A, Sisuk N, Smerpitak K, Wardkein P. Analysis of beat frequency detector based on basic logic gates. ICIC Express Letters. 2018;12:815-22.

2. Li H, Cui L, Lin Z, Li L, Wang R, Zhang C. Signal detection for optical AC and DC voltage sensors based on Pockels effect. IEEE Sensors Journal. 2013;13:2245-52.

3. Harikrushna DI, Tiwari M, Singh JK, Khare A. Design, implementation and characterization of XOR phase detector for DPLL in 45 nm CMOS technology. Advanced Computing. 2011;2:45-57.

4. Reich G. A moiré pattern-based thread counter. The Physics Teacher. 2017;55:426-30.

5. Gabrielyan E. The basics of line moiré patterns and optical speedup. arXiv preprint physics/0703098. 2007.

6. Cadarso VJ, Chosson S, Sidler K, Hersch RD, Brugger J. High-resolution 1D moirés as counterfeit security features. Light: Science & Applications. 2013;2:e86.

7. Kim S, Jung Y, Jung Kim J, Byun G, Lee S, Lee H. Direct observation of nanometer-scale strain field around CoSi2/Si interface using scanning moiré fringe imaging. Applied Physics Letters. 2014;104:161610.

8. Asundi A, Sajan MR. Digital moiré for measurements on cylindrical objects. Journal of Optics. 1998;29:128-34.

9. Xie H, Wang Q, Kishimoto S, Dai F. Characterization of planar periodic structure using inverse laser scanning confocal microscopy moiré method and its application in the structure of butterfly wing. Journal of Applied Physics. 2007;101:103511.

10. Du H, Zhao H, Li B, Zhao J, Cao S. Three frames phase-shifting

shadow moiré using arbitrary unknown phase steps. Measurement Science and Technology. 2012;23:105201.

11. Kim S, Lee S, Kondo Y, Lee K, Byun G, Lee S, et al. Strained hetero interfaces in Si/SiGe/SiGe/SiGe multi-layers studied by scanning moiré fringe imaging. Journal of Applied Physics. 2013;114:053518.

12. Ishizuka A, Hytch M, Ishizuka K. STEM moiré analysis for 2D strain measurements. Microscopy. 2017;66:217-21.

13. Ohbuchi Y, Sakamoto H, Nagatomo N. Thermal image analysis of plastic deformation and fracture behavior by a thermo-video measurement system. Measurement Science and Technology. 2016;27:124015.

14. Zhu F, Lin X, Zhang W, Fan J, Liu S. Morphology Evaluation of Microelectronic Packaging Substrates Using Shadow Moiré Technique. IEEE Access. 2018;6:33099-110.

15. Chittari BL, Leconte N, Javvaji S, Jung J. Pressure induced compression of flatbands in twisted bilayer graphene. Electronic Structure. 2018;1:015001.

16. Naden AB, O'Shea KJ, MacLaren DA. Evaluation of crystallographic strain, rotation and defects in functional oxides by the moiré effect in scanning transmission electron microscopy. Nanotechnology. 2018;29:165704.

17. Jamshidi-Ghaleh K, Tavassoly MT, Mansour N. Diffusion coefficient measurements of transparent liquid solutions using Moiré deflectometry. Journal of Physics D: Applied Physics. 2004;37:1993-7.

18. Li Y, Tang M, Xie H, Zhu R, Luo Q, Gu C. A measuring system for mechanical characterization of thin films based on a compact in situ micro-tensile tester and SEM moiré method. Journal of Micromechanics and Microengineering. 2013;23:085021.

19. Schneider D, Gloy YS, Merhof D. Vision-Based On-Loom Measurement of Yarn Densities in Woven Fabrics. Instrumentation and Measurement, IEEE Transactions on. 2015;64:1063-74.

20. Reich G. A Moiré Pattern-Based Thread Counter. The Physics Teacher. 2017;55:426-30.

21. Lin JJ. Applying a Co-occurrence Matrix to Automatic Inspection of Weaving Density for Woven Fabrics. Textile Research Journal - TEXT RES J. 2002;72:486-90.

22. Wijayono A, Munandar T, Rudi R, Putra VGV. Woven Fabric Density Measurement Using Image Processing Techniques. In: Proceedings of the Indonesian Textile Conference: Textile 4.0 Clothing and Beyond vol. 3; 2019 Jul 27; Bandung, Indonesia: Penerbit Politeknik STTT Bandung; 2019. p. 174-80.

23. Pan R, Zhang J, Li Z, Gao W, Xu B, Li W. Applying Image Analysis for Automatic Density Measurement of High-tightness Woven Fabrics. Fibres and Textiles in Eastern Europe. 2016;24:66-72.

24. Zhang J, Pan R, Wang J, Gao W, Han Y. An efficient method for density measurement for high-tightness woven fabrics. Textile Research Journal. 2017;87:329-39.

25. Ravandi SAH, Toriumi K. Fourier Transform Analysis of Plain Weave Fabric Appearance. Textile Research Journal. 1995;65:676-83.

26. Pan R, Gao W, Li Z, Gou J, Zhang J, Zhu D. Measuring Thread Densities of Woven Fabric Using the Fourier Transform. Fibres and Textiles in Eastern Europe. 2015;23:35-40.

27. Le B, Troendle D, Jang B. Detecting fabric density and weft distortion in woven fabrics using the discrete fourier transform. In: Proceedings of the 2021 ACM Southeast Conference (ACMSE '21); 2021 Apr 15-17; New York, NY, USA. Association for Computing Machinery; 2021. p. 108-13.

28. Je UK, Park CK, Lim HW, Cho HS, Lee DY, Lee HW, et al. Evaluation of high grid strip densities based on the moiré artifact analysis for quality assurance: Simulation and experiment. Nuclear Instruments and Methods in Physics Research Section A: Accelerators, Spectrometers, Detectors and Associ-

ated Equipment. 2017;866:58-64.

29. Wu J, Zhong P, Ling J, Li Z, Tang X, Su S, et al. Design Method of Fabric Density Sensor Based on the Virtual Grating With Gradual Constant. IEEE Access. 2019;7:160345-62.

30. Wait P. Simple, sensitive metal detector. ETI561: How To Build Gold & Treasure Detectors. 1981:22-7.

31. Rakes C. BASIC CIRCUITRY Give up your day job and become a full-time beachcomber with the help of metal-detecting circuits. POPTRONICS-FARMINGDALE NY-. 2001;2:59-62.

32. Cheeseman G. Metal Detectors – Part 1. Electronics and Beyond. 1999;18:15-31.

33. Jawad AM, Jawad HM, Hock GC. Design of a Beat Frequency Oscillator Metal Detector. IOSR Journal of Electronics and Communication Engineering (IOSR-JECE). 2014;9:56-62.

34. Saha S, Kar R, Mandai T, Kumar N, Ghoshal S. Optimal linear phase FIR high pass filter design using PSOCFIWA-WM. In: Proceedings of the 2012 World Congress on Information and Communication Technologies (WICT); 2012 Oct 30 - 2012 Nov 2; Trivandrum, India: IEEE; 2012. p. 768-73.

35. Sapargaliyev Y, Kalganova T. Constrained and Unconstrained Evolution of "LCR" Low-Pass Filters with Oscillating Length Representation. In: Proceedings of the 2006 IEEE International Conference on Evolutionary Computation (CEC); 2016 Jul 16-21; Vancouver, BC, Canada: IEEE; 2006. p. 1529-36.

36. Yu L, Wang SR, Lin GY. An image domain approach to the interpretation of the visible moiré phenomenon. Journal of Optics. 2013;15:075407.

37. Roy P, Dutta S, Dey N, Dey G, Chakraborty S, Ray R. Adaptive thresholding: A comparative study. In: Proceedings of the 2014 International Conference on Control, Instrumentation, Communication and Computational Technologies (ICCICCT); 2014 Jul 10-11; Kanyakumari, India: IEEE; 2014. p. 1182-6.

38. Khokhuntod P, Kaewpoonsuk A. Analysis of Moiré pattern for parallel binary gratings based on AND and OR operators. Journal of Optics. 2024;26:085701.

39. Zhao AX, Tang XJ, Zhang ZH, Liu JH. The parameters optimization selection of Savitzky-Golay filter and its application in smoothing pretreatment for FTIR spectra. In: Proceedings of the 2014 9th IEEE Conference on Industrial Electronics and Applications (ICIEA); 2014 Jun 9-11; Hangzhou, China: IEEE; 2014. p. 516-21.

40. Je U, Kim J, Cho H, Lim H, Park C, Kim G, et al. Indirect measurement of high grid strip densities over Nyquist sampling rate based on the moiré pattern analysis for quality assurance in grid manufacturing. Measurement. 2016;91:634-40.

APPENDIX

APPENDIX A FOURIER SERIES DERIVATION FOR A SHIFTED RECTANGULAR PULSE

Step 1: Definition of the Shifted Rectangular Pulse

Let $Q(x)$ be a periodic rectangular pulse function defined as follows:

$$Q(x) = \begin{cases} 1, & \phi_0 < x \bmod P < \phi_0 + P_h \\ 0, & \text{otherwise} \end{cases} \tag{A.1}$$

where:

- P is the period of the function.
- P_h is the duration for which the pulse is at high level (equal to 1).
- $\delta = \frac{P_h}{P}$ is the duty cycle, a unitless ratio.
- ϕ_0 is the starting position of the pulse within each period, measured in the same units as x (e.g., millimeters, micrometers, or radians).

The use of x mod P ensures that the rectangular pulse is repeated periodically across the entire domain of x. Specifically, x mod P maps any real number x into the interval $[0, P)$ by taking the remainder after division by the period P. This allows the condition $\phi_0 < x \bmod P < \phi_0 + P_h$ to define a repeating pulse structure, where a high signal level occurs within the pulse width P_h starting at position ϕ_0 in every period. Without this modular operation, the pulse would only appear once, and the function would not be periodic, which is a necessary condition for a valid Fourier series representation.

Step 2: Fourier Series of the Shifted Rectangular Pulse

The function $Q(x)$ is a periodic rectangular pulse of period P, starting at $x = \phi_0$ and having a width P_h, such that the signal equals 1 in the interval $[\phi_0, \phi_0 + P_h)$ and 0 elsewhere in each period. This signal can be expanded in a

Fourier series as:

$$Q(x) = \frac{a_0}{2} + \sum_{n=1}^{\infty} \left[a_n \cos\left(\frac{2\pi n x}{P}\right) + b_n \sin\left(\frac{2\pi n x}{P}\right) \right] \tag{A.2}$$

where the Fourier coefficients a_0, a_n, and b_n are determined as follows.

Computation of a_0:

$$a_0 = \frac{2}{P} \int_{\phi_0}^{\phi_0 + P_h} 1 \, dx = \frac{2P_h}{P} = 2\delta \tag{A.3}$$

where $\delta = \frac{P_h}{P}$ is the duty cycle.

Computation of a_n:

$$a_n = \frac{2}{P} \int_{\phi_0}^{\phi_0 + P_h} \cos\left(\frac{2\pi n x}{P}\right) dx \tag{A.4}$$

Let $\omega = \frac{2\pi}{P}$, then:

$$a_n = \frac{2}{P} \int_{\phi_0}^{\phi_0 + P_h} \cos(n\omega x) \, dx = \frac{2}{n\omega P} \left[\sin(n\omega(\phi_0 + P_h)) - \sin(n\omega\phi_0) \right] \tag{A.5}$$

Apply the identity $\sin A - \sin B = 2\cos\left(\frac{A+B}{2}\right)\sin\left(\frac{A-B}{2}\right)$:

$$a_n = \frac{4}{n\omega P} \cos\left(n\omega\left(\phi_0 + \frac{P_h}{2}\right)\right) \sin\left(\frac{n\omega P_h}{2}\right) \tag{A.6}$$

Substituting $\omega = \frac{2\pi}{P}$ and $\delta = \frac{P_h}{P}$, we get:

$$a_n = \frac{2}{n\pi} \sin(n\pi\delta) \cos\left(n\omega\left(\phi_0 + \frac{P_h}{2}\right)\right) \tag{A.7}$$

Computation of b_n:

$$b_n = \frac{2}{P} \int_{\phi_0}^{\phi_0 + P_h} \sin\left(\frac{2\pi n x}{P}\right) dx = \frac{2}{P} \int_{\phi_0}^{\phi_0 + P_h} \sin(n\omega x) \, dx \tag{A.8}$$

Using the identity:

$$\cos A - \cos B = -2 \sin\left(\frac{A+B}{2}\right) \sin\left(\frac{A-B}{2}\right) \tag{A.9}$$

we obtain:

$$b_n = \frac{4}{n\omega P} \sin\left(n\omega\left(\phi_0 + \frac{P_h}{2}\right)\right) \sin\left(\frac{n\omega P_h}{2}\right) \tag{A.10}$$

Again, substituting $\omega = \frac{2\pi}{P}$ and $\delta = \frac{P_h}{P}$:

$$b_n = \frac{2}{n\pi} \sin(n\pi\delta) \sin\left(n\omega\left(\phi_0 + \frac{P_h}{2}\right)\right) \tag{A.11}$$

Compact cosine-phase form: Once the Fourier coefficients a_n and b_n have been derived, the signal can be expressed in a more compact form using the cosine-phase identity:

$$Q(x) = \delta + \sum_{n=1}^{\infty} A_n \cos(n\omega x - \phi_n) \tag{A.12}$$

where the amplitude A_n and phase ϕ_n are given by:

$$A_n = \sqrt{a_n^2 + b_n^2}, \quad \phi_n = \arctan\left(\frac{b_n}{a_n}\right) \tag{A.13}$$

Computation of A_n: Using the previously derived expressions:

$$a_n = \frac{2}{n\pi} \sin(n\pi\delta) \cos\left(n\omega\left(\phi_0 + \frac{P_h}{2}\right)\right), \quad b_n = \frac{2}{n\pi} \sin(n\pi\delta) \sin\left(n\omega\left(\phi_0 + \frac{P_h}{2}\right)\right) \tag{A.14}$$

Substituting into the formula for A_n:

$$\begin{aligned} A_n &= \sqrt{\left(\frac{2}{n\pi} \sin(n\pi\delta) \cos\left(n\omega\left(\phi_0 + \frac{P_h}{2}\right)\right)\right)^2 + \left(\frac{2}{n\pi} \sin(n\pi\delta) \sin\left(n\omega\left(\phi_0 + \frac{P_h}{2}\right)\right)\right)^2} \\ &= \frac{2}{n\pi} \sin(n\pi\delta) \cdot \sqrt{\cos^2\left(n\omega\left(\phi_0 + \frac{P_h}{2}\right)\right) + \sin^2\left(n\omega\left(\phi_0 + \frac{P_h}{2}\right)\right)} \\ &= \frac{2}{n\pi} \sin(n\pi\delta) \end{aligned}$$

Computation of ϕ_n: Likewise, the phase angle is computed as:

$$\begin{aligned} \phi_n &= \arctan\left(\frac{\frac{2}{n\pi} \sin(n\pi\delta) \sin\left(n\omega\left(\phi_0 + \frac{P_h}{2}\right)\right)}{\frac{2}{n\pi} \sin(n\pi\delta) \cos\left(n\omega\left(\phi_0 + \frac{P_h}{2}\right)\right)}\right) \\ &= \arctan\left(\frac{\sin\left(n\omega\left(\phi_0 + \frac{P_h}{2}\right)\right)}{\cos\left(n\omega\left(\phi_0 + \frac{P_h}{2}\right)\right)}\right) \\ &= n\omega\left(\phi_0 + \frac{P_h}{2}\right) \end{aligned}$$

Final expression: Substituting A_n and ϕ_n into the compact form gives:

$$Q(x) = \delta + \sum_{n=1}^{\infty} \left[\frac{2}{n\pi} \sin(n\pi\delta) \cdot \cos\left(n\omega x - n\omega\left(\phi_0 + \frac{P_h}{2}\right)\right)\right] \tag{A.15}$$

$$Q(x) = \delta + \sum_{n=1}^{\infty} \left[\frac{2}{n\pi} \sin(n\pi\delta) \cdot \cos\left(n\omega x - n\omega\phi_0 - n\omega \frac{P_h}{2} \right) \right] \tag{A.16}$$

Angular domain normalization:

To simplify the expression, we absorb the constant angular frequency $\omega = \frac{2\pi}{P}$ into the phase term ϕ_0, such that:

$$n\omega\phi_0 \to n\phi_0 \quad \text{and} \quad n\omega\frac{P_h}{2} = \pi n\delta \tag{A.17}$$

This yields the final compact expression:

$$Q(x) = \delta + \sum_{n=1}^{\infty} \left[\frac{2}{n\pi} \sin(n\pi\delta) \cdot \cos\left(n\omega x - n\phi_0 - \pi n\delta \right) \right] \tag{A.18}$$

This form emphasizes the frequency-domain interpretation in terms of physical position x, angular frequency $\omega = \frac{2\pi}{P}$, and phase offset ϕ_0.

Step 3: Conversion from Cosine to Sine Terms We apply the trigonometric identity:

$$\sin A \cdot \cos B = \frac{1}{2} \left[\sin(A + B) + \sin(A - B) \right] \tag{A.19}$$

to the term:

$$\sin(n\pi\delta) \cdot \cos(n\omega x - n\phi_0 - \pi n\delta) \tag{A.20}$$

with $A = n\pi\delta$ and $B = n\omega x - n\phi_0 - \pi n\delta$. We compute:

$$A + B = n\omega x - n\phi_0$$

$$A - B = -n\omega x + n\phi_0 + 2\pi n\delta = -(n\omega x - n\phi_0 - 2\pi n\delta)$$

Thus:

$$\sin(n\pi\delta) \cdot \cos(n\omega x - n\phi_0 - \pi n\delta) = \frac{1}{2} \left[\sin(n\omega x - n\phi_0) + \sin(-(n\omega x - n\phi_0 - 2\pi n\delta)) \right] \tag{A.21}$$

$$\sin(n\pi\delta) \cdot \cos(n\omega x - n\phi_0 - \pi n\delta) = \frac{1}{2} \left[\sin(n\omega x - n\phi_0) - \sin(n\omega x - n\phi_0 - 2\pi n\delta) \right] \tag{A.22}$$

Multiplying both sides by $\frac{2}{n\pi}$ yields:

$$\frac{2}{n\pi}\sin(n\pi\delta)\cdot\cos(n\omega x-\pi n\delta-n\phi_0) = \frac{1}{n\pi}\left[\sin(n\omega x - n\phi_0) - \sin(n\omega x - n\phi_0 - 2\pi n\delta)\right] \tag{A.23}$$

Final Result

Therefore, the Fourier series can be written in the form:

$$\boxed{Q(x) = \delta + \frac{1}{\pi}\sum_{n=1}^{\infty}\left[\frac{-1}{n}\sin(n\omega x - n\phi_0 - 2\pi n\delta) + \frac{1}{n}\sin(n\omega x - n\phi_0)\right]} \tag{A.24}$$